



Center for Flow Physics and Control
in the
Hessert Laboratory for Aerospace Research

University of Notre Dame
Notre Dame, IN 46556



*Department of Aerospace
and Mechanical Engineering*



20070904056

**EXPERIMENTS IN SOUND AND STRUCTURAL
VIBRATIONS USING AN AIR-ANALOG MODEL
DUCTED PROPULSION SYSTEM**

Scott C. Morris

Final Report UND-SM07-329
August 2007

Prepared Under
Grant No. N00014-04-1-0522

by the

University of Notre Dame
Notre Dame, Indiana

for the

Department of the Navy
Office of Naval Research
Arlington, Virginia

**UND-SM07-329
August 2007**

**EXPERIMENTS IN SOUND AND STRUCTURAL
VIBRATIONS USING AN AIR-ANALOG MODEL
DUCTED PROPULSION SYSTEM**

FINAL TECHNICAL REPORT

Prepared by:

Scott C. Morris
Assistant Professor
Department of Aerospace and Mechanical Engineering
University of Notre Dame
Notre Dame, IN 46556
s.morris@nd.edu

**UND-SM07-329
August 2007**

REPORT DOCUMENTATION PAGEForm Approved
OMB No. 0704-0188

Public reporting burden for this collection of information is estimated to average 1 hour per response, including the time for reviewing instructions, searching existing data sources, gathering and maintaining the data needed, and completing and reviewing this collection of information. Send comments regarding this burden estimate or any other aspect of this collection of information, including suggestions for reducing this burden to Department of Defense, Washington Headquarters Services, Directorate for Information Operations and Reports (0704-0188), 1215 Jefferson Davis Highway, Suite 1204, Arlington, VA 22202-4302. Respondents should be aware that notwithstanding any other provision of law, no person shall be subject to any penalty for failing to comply with a collection of information if it does not display a currently valid OMB control number. **PLEASE DO NOT RETURN YOUR FORM TO THE ABOVE ADDRESS.**

1. REPORT DATE (DD-MM-YYYY)

27-August, 2007

2. REPORT TYPE

Final Technical Report

3. DATES COVERED (From - To)

6/1/04 - 5/31/07

4. TITLE AND SUBTITLE

YIP-Experiments in Sound and Structural Vibration Using Air-

Analog Model Ducted Propulsion Systems

5a. CONTRACT NUMBER**5b. GRANT NUMBER**

N00014-1-0522

5c. PROGRAM ELEMENT NUMBER**5d. PROJECT NUMBER****5e. TASK NUMBER****5f. WORK UNIT NUMBER****6. AUTHOR(S)**

Scott C. Morris

7. PERFORMING ORGANIZATION NAME(S) AND ADDRESS(ES)University of Notre Dame
Notre Dame, IN 46556**8. PERFORMING ORGANIZATION REPORT NUMBER**

UND-SM07-329

9. SPONSORING / MONITORING AGENCY NAME(S) AND ADDRESS(ES)Office of Naval Research
875 North Randolph Street
Arlington, VA 22203-1995**10. SPONSOR/MONITOR'S ACRONYM(S)****11. SPONSOR/MONITOR'S REPORT NUMBER(S)****12. DISTRIBUTION / AVAILABILITY STATEMENT**

Unlimited

DISTRIBUTION STATEMENT A
Approved for Public Release
Distribution Unlimited**13. SUPPLEMENTARY NOTES****14. ABSTRACT**

The prediction of the radiated acoustic signature of underwater structures has been and will continue to be of great importance for the Navy. New and innovative designs of maneuvering and propulsion systems present challenging problems for the prediction of radiated acoustics. The present research focused on the development of structural acoustic experiments that use air as the working fluid. The test specimens were designed using very light weight structures such that the fluid loading effects would be non-negligible, and in some cases dominant. A number of configurations have been investigated, including flat membranes, rib-stiffened cylindrical structures, and a ducted rotor with elastic shell. The ducted rotor facility is part of a continuing effort involving the effects of inlet distortion on the elastic shell vibrations. A substantial database of flow field, acoustic, and vibration measurements has resulted. The data show a significant sensitivity of the structural vibration to the spatial distribution of the acoustic sources.

15. SUBJECT TERMS**16. SECURITY CLASSIFICATION OF:** Unclassified**a. REPORT**

U

b. abstract

U

c. THIS PAGE

U

17. LIMITATION OF ABSTRACT**18. NUMBER OF PAGES**

99

19a. NAME OF RESPONSIBLE PERSON

Scott C. Morris

19b. TELEPHONE NUMBER (include area code)

574-631-3238

ABSTRACT

The prediction of the radiated acoustic signature of underwater structures has been and will continue to be of great importance for the Navy. New and innovative designs of maneuvering and propulsion systems present challenging problems for the prediction of radiated acoustics. The present research focused on the development of structural acoustic experiments that use air as the working fluid. The test specimens were designed using very light weight structures such that the fluid loading effects would be non-negligible, and in some cases dominant. A number of configurations have been investigated, including flat membranes, rib-stiffened cylindrical structures, and a ducted rotor with elastic shell. The ducted rotor facility is part of a continuing effort involving the effects of inlet distortion on the elastic shell vibrations. A substantial database of flow field, acoustic, and vibration measurements has resulted. The data show a significant sensitivity of the structural vibration to the spatial distribution of the acoustic sources. In some cases the acoustic-vibration coupling led to a significant change in the natural frequencies, and hence the coupling to the frequency dependent acoustic and convecting hydrodynamic pressure.

1.0 INTRODUCTION

The ability to predict the radiated acoustic signature of underwater structures has been and will continue to be of great importance for the Navy. New and innovative designs of maneuvering and propulsion systems present challenging problems for the prediction of radiated acoustics using analytical or numerical approaches alone. A significant obstacle in the development and validation of predictive methodologies is a general lack of high quality, comprehensive experimental data. These data are important for both validation of specific models and methodologies, as well as for investigating phenomena that are not yet well understood.

The objective of the present research was to develop the experimental methods needed to study the coupling between hydrodynamics, hydroacoustics, and structural acoustics in an *air-analog* system. The use of air as a working fluid is preferred to water in many circumstances due to the relative ease of working with models and instrumentation in a laboratory. An air environment allows for standard laboratory materials and instrumentation to be used without difficulty. Additionally, models in air can be placed in a near-perfect anechoic environment in order to easily obtain radiated sound power, directivity, etc.

The relevant parameters for fluid-flow problems with rigid boundary conditions include the Reynolds number and the Mach number. This allows most hydrodynamic and hydroacoustic problems to be considered in air with little difficulty. The use of air for the study of underwater structural vibrations and acoustics is generally not considered acceptable since dimensional similarity is generally not possible. Since the materials that can typically be used for air experiments are not too different from those used in underwater applications, there is a necessary mismatch between the dimensionless parameters of an underwater application and an air-analog experiment. However, the effects of membrane waves, flexural waves, fluid loading can be studied in air-analog systems under parameter ranges that are of direct relevance to underwater problems. For example, it will be shown that a thin plate or shell exhibits significant fluid loading effects in air at low frequencies. By considering higher frequencies or thicker materials, the effects of dispersive waves with little fluid loading can be examined. This flexibility in designing the air-analog experiments presents a unique advantage over water experiments.

A number of various geometries were considered in this study. The intent was to gain experience with the methods and instrumentation using relatively simple problems, and then consider config-

urations of increasing complexity. The majority of the efforts were focused on the development and measurement of a new facility that incorporates a rotor operating within an elastic duct. The geometry was considered to have a suitable balance between simplicity in its boundary conditions and complexity of the physical phenomena involved. Other geometries included combinations of plates and shells with both hydrodynamic and acoustic excitation.

It is noted that the intended focus of this research evolved over the course of the project. Discussion with engineers from the NSWC, ONR, and Electric Boat allowed the experimental program to take advantage of a number of capabilities that were of direct interest to the Navy. Specifically, the effects of internal mean flow distortion on the structural response of an elastic duct was considered in some detail.

The remainder of this report is structured as follows. Section 2 briefly describes the basic instrumentation that was used in this research. Section 3 provides a detailed description of the geometry and properties of the test setup and the elastic structures used. Sections 4 through 8 describe the primary results of the experimental program including a detailed set of conclusions in each section. Overall conclusions and a discussion of the project are given in Section 9.

2.0 EXPERIMENTAL TECHNIQUES

The experiments described in the following sections of this report will require a number of sophisticated measurement systems. A summary of the measurement capabilities and relevant references are given in the following sub-sections.

2.1 Anechoic Wind Tunnel

All experiments will be performed in the Anechoic Wind Tunnel (AWT) located within the Hessel Laboratory for Aerospace Research at the University of Notre Dame. A schematic of the tunnel is shown in Figure 1. The AWT consists of an anechoic chamber with a working space that is 20ft wide by 26ft long by 8ft high. The 22in fiberglass wedges have a coefficient of energy absorption at normal incidence of 0.99 or greater. The wedges provide a low frequency cutoff of about 100Hz.

A low disturbance subsonic free-jet test section wind tunnel is located within the anechoic chamber. The cross-sectional area of the test region is 4ft². A low noise centrifugal blower is connected to the flow-exit of the tunnel (not shown in Figure 1) through a muffler/diffuser system. This provides a maximum test section velocity of 110ft/sec. A complete description of the tunnel's individual components and important characteristics is presented in Mueller et al. (1992a,b).

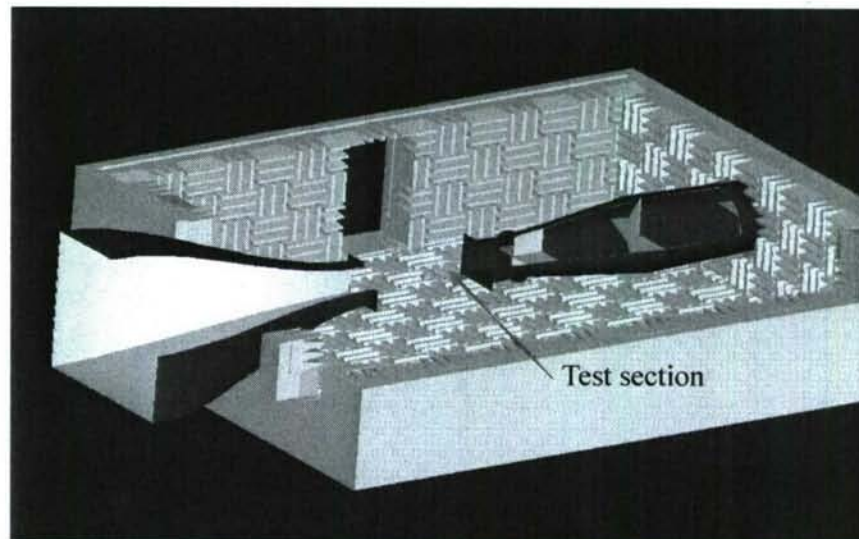


Figure 1 Schematic of the Anechoic Wind Tunnel and test section.

2.2 Phased Microphone Array

The AWT is equipped with a dual planar array measurement system for acoustic measurements. Measuring acoustics using an array of microphones offers two major advantages over measuring acoustics using a single microphone. First, the array increases the signal to noise ratio over that of a single microphone by a factor approximately equal to the number of microphones. The second benefit of an array is its capability to spatially localize acoustic sources. The two, 40 microphone arrays are fully calibrated, and capable of reducing the ambient noise levels of the facility by as much as 20dB.

Each of the AWT planar arrays consists of a strategic arrangement of 40 microphones mounted in a flat panel. Figure 2 shows a picture of one array panel situated outside of the AWT before microphone installation, and a completed acoustic array situated inside the AWT from the back-side of the array panel. By placing microphones to avoid replicating the spacing between any pair, an acoustic array resolves the acoustic contributions from a focal location while rejecting acoustic contributions from other locations (Underbrink, 2002). By using perforated plastic sheets as the array panels, the locations of the microphones in the AWT array panels may be altered to suit the needs of the acoustic measurement experiments at hand. Also, all microphones from the two arrays may be merged into one array panel for single plane measurements.

For the sake of example, Figure 3 shows a diagram of the acoustic array panels in the two-panel configuration with an array located on either side of the open jet test section to measure the trailing edge acoustics from a model foil. In the model foil experiments, the trailing edge is oriented vertically in the wind tunnel and the open jet is constrained by acoustically absorbing endplates that face the model side edges.

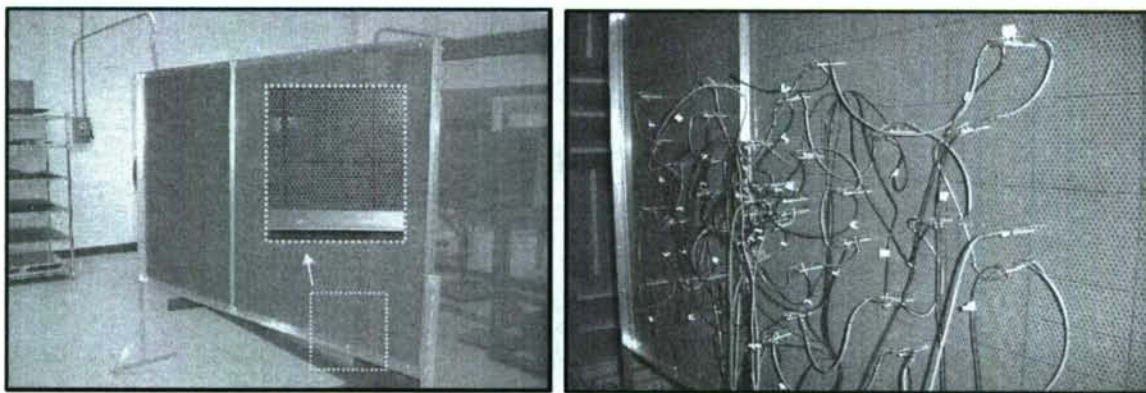


Figure 2 Picture of phased array panel (left), and completed inside the AWT (right)

In the acquisition stage of the acoustic array experiments, a digital representation of the analog signal from each microphone is acquired using 10 synchronized analog to digital converters controlled by a PC workstation. After time series data have been acquired from all the microphones, post-processing algorithms focus the array to a grid of locations in space. The most common array source localization technique is a post-processing operation called beamforming.

Beamforming produces an acoustic source level map over a specified grid of points in space. The classical beamforming process shifts each microphone signal in time by a delay equal to the assumed acoustic wave travel time from the beamforming grid point to the microphone location. The shifted microphone signals are summed either in the time or the frequency domain. The mean square value, or the power spectral density level, represents a value proportional to the mean-square acoustic pressure emanating from the beamforming grid point. Scanning a grid of points in space forms a beamforming map. If an acoustic source exists at the beamforming grid point, the summed acoustic source signal is amplified and a peak appears in the beamforming map. In addition, extraneous noise that is uncorrelated among microphones is reduced through phasing the

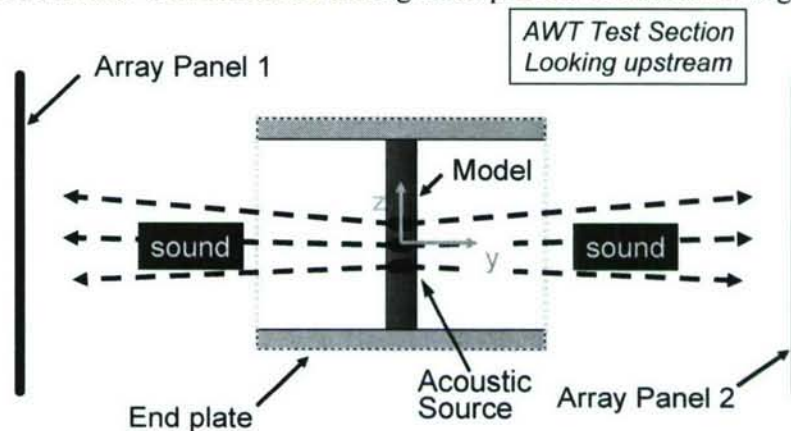


Figure 3 Schematic of dual array configuration inside the AWT

array via beamforming. The array is calibrated using a speaker to convert the beamforming map into a sound pressure level (SPL) map. Figure 4 shows an SPL map produced via beamforming using measurements in the presence of a calibration speaker for a frequency of 3kHz.

A full description of classical beamforming in the frequency domain follows the work of Dougherty (2002). Beamforming has two limitations, which are minimized through array pattern design optimization. The first is the capability of the array to resolve independent sources. The array resolution is quantified by the array main lobe (or beam), which depends on the array aperture, the

outer perimeter of the array, relative to the wavelength of the sound and the distance from the sound source to the array. Figure 4 points out the main lobe in the beamforming map of the calibration speaker plane. The larger the wavelength and the larger the distance from the sound source to the array, the wider the beamwidth. The larger the array aperture, the more narrow the beamwidth. The number of microphones and their placement governs the second limitation of the array: the strength of sidelobes. Sidelobes are unwanted artifacts of beamforming that appear as secondary peaks in the beamforming map as illustrated in Figure 4. They are essentially the product of spatial ambiguity due to 2π multiples in phase among more widely spaced microphone pairs in the presence of a source. The nearness of the sidelobes to the mainlobe and the magnitude of the sidelobes increase with decreasing wavelength and increasing closeness to the source.

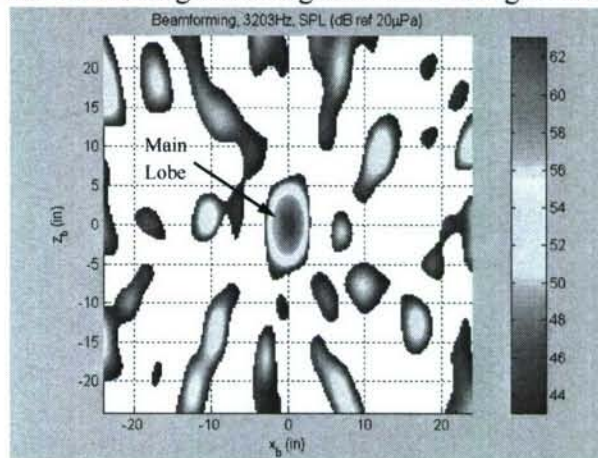


Figure 4 SPL map produced via beamforming using measurements from the array in AWT

2.3 Laser Doppler Vibrometry

A laser Doppler vibrometer is based on the principle of the detection of the Doppler shift of coherent laser light that is scattered from a small area of the test object. The object scatters or reflects light from the laser beam and the Doppler frequency shift is used to measure the component of velocity which lies along the axis of the laser beam. Since the laser light has a very high frequency (typically $>10^{14}$ Hz) a direct demodulation of the light is not possible. An optical interferometer is therefore used to mix the scattered light coherently with a reference beam. The photo detector measures the intensity of the mixed light whose beat frequency is equal to the difference frequency between the reference and the measurement beam. Vibration frequencies up to 400 kHz can be measured from a distance of up to 20 m.

Two LDV systems were used for the structural vibration measurements. The first is a Polytec single point LDV system. The second is a Polytec Scanning system that allows for fully programable geometry scans for a given experiment. The two systems were used in combination in order to obtain the full two-point correlation functions of vibrational velocity. This information is important when stochastic forcing such as when broadband rotor noise and/or the convecting hydrodynamic pressure is dominant.

3.0 EXPERIMENTAL APPARATUS

3.1 Tensioned Plate/Membrane Apparatus

A new experiment was created in which thin materials could be placed in the AWT with arbitrary tension. The purpose was to use acoustic and hydrodynamic forcing in order to gain experience working with the structural acoustics in very thin materials. This section will describe the geometry and the acoustic response experiments using a very thin aluminum membrane. Section 6 of this report will describe the response of the membrane to complex hydrodynamic forcing.

A schematic of the fixture geometry is shown in Figure 5. The assembly consists of an aluminum frame within a larger structure. The inner frame supports the test specimen. An insert piece is used to define the shape of the vibrationally active region of the membrane. The material is tensioned from four sides using a mechanical pivot with a spring and force transducer. Front and back images of the completed assembly in the AWT are shown in Figure 6. The active region was circular as observed on the image of the back of the fixture. The material used in the data presented in this section was aluminum with a thickness of 0.0127mm (0.0005 inches). The mass of the membrane per unit surface area was equivalent to 2.8cm of air.

The intent of the exercise was to measure the natural frequencies and mode shapes of the membrane using various materials under various tension values. For a circular membrane the motion normal to the plane is a solution to

$$\frac{1}{r} \frac{\partial}{\partial r} \left(r \frac{\partial \eta}{\partial r} \right) + \frac{1}{r^2} \frac{\partial^2 \eta}{\partial \phi^2} = \frac{1}{c^2} \frac{\partial^2 \eta}{\partial t^2} \quad (1)$$

where $c^2 = T/(\rho_s h)$ is the wave speed of the membrane as set by the Tension (T) and the mass per unit area ($\rho_s h$). The discrete solutions of equation 1 are classified by the mode order pair (m, n) where m is the number of diametrical nodal lines and n is the number of circular nodal lines including the outer boundary of the material. The first several mode shapes are shown in Figure 7. The vibration of the membrane was measured using the single SLDV. The measurement grid computed as shown in Figure 8. These points were programed into the SLDV for automatic scanning. The membrane was forced using broadband acoustic forcing and a small speaker placed in proximity to the structure. Two examples that identify the (1,1) and (0,2) modes are shown in Figure 9. The colors are representative of the amplitude of the motion at a particular phase.

The autospectral density from each of the measurement points were averaged in order to provide the net vibration of the membrane. These data, along with a number of identified mode order pairs are shown in Figure 10 using a tension of 182.5N/m. The natural frequencies can be easily observed by the local maxima in this spectrum. The full two point correlations were evaluated at each of these maximum (e.g., figure 9) in order to identify the mode order pair. Table 1 summarizes the measured and calculated frequencies of the first few modes. It can be observed that the measured natural frequencies are lower than the in-vacuo values due to the significant fluid loading effects. For example, the lowest mode (0,1) indicates a resonant frequency of 36Hz, compared to the in-vacuo value of 137Hz. The reduction in frequency by a factor of 3.8 indicates that the acceleration of the mass of the air surrounding the membrane is approximately 14.5 times the mass of the membrane itself (i.e., the square of the frequency ratio). The effective thickness of the accelerated air on each side of the membrane is also given in Table 1.

It is of interest to note that the fluid loading factor (Blake, 1986), defined as:

$$\beta_{FL} = \frac{(\rho c)_{fluid}}{(\rho_s h) \omega} \quad (2)$$

is approximately 50 at the lowest mode (36Hz). That is, despite the relatively large density ratio from the aluminum to air (2700/1.15), the structural vibrations are dominated by the fluid loading effects because the product of the acoustic wavenumber and the material thickness is also large. In this example (36Hz), $k_o h = 118,000$.

The ratio of the measured natural frequency of each mode to the in-vacuo natural frequency can be observed to increase for each higher order mode. This is expected since the fluid loading factor is less for each successive mode. Results from a larger tension value of 255.4N/m are shown in Figure 11 and Table 2. These data show similar results in terms of the changes in natural frequency. The frequency ratio ($f_{meas}/f_{in-vacuo}$) is plotted in Figure 12 for both sets of data. The frequencies have been further normalized by the ratio of the membrane wave speed to the sound speed (c_m/c_o).

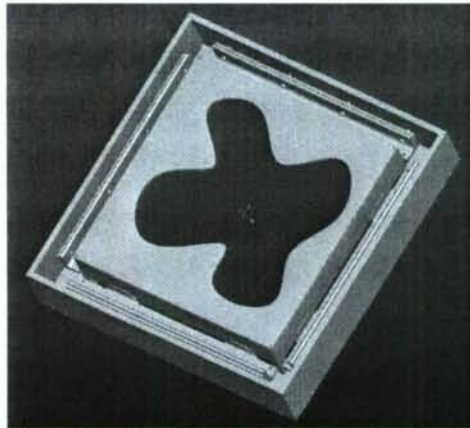


Figure 5 Schematic of mechanical fixture for plate/membrane stretching

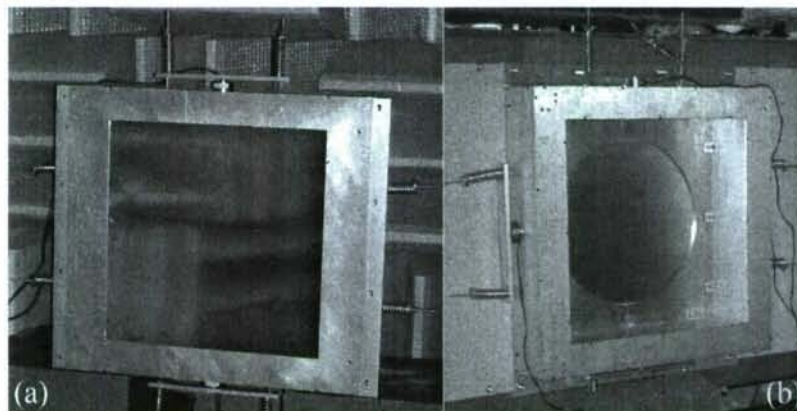


Figure 6 Photograph of front (left) and rear (right) of the fixture with circular insert

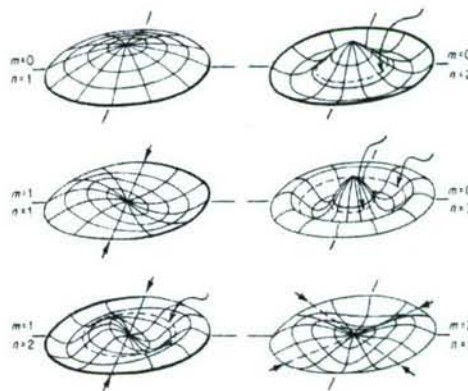


Figure 7 Mode shapes of a circular membrane (from Morse and Ingard)

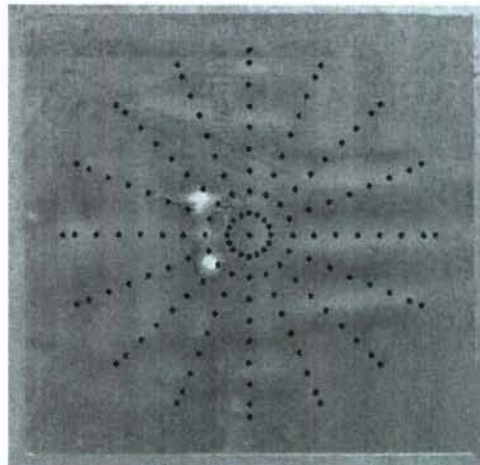


Figure 8 Scanning points on circular active region of aluminum membrane

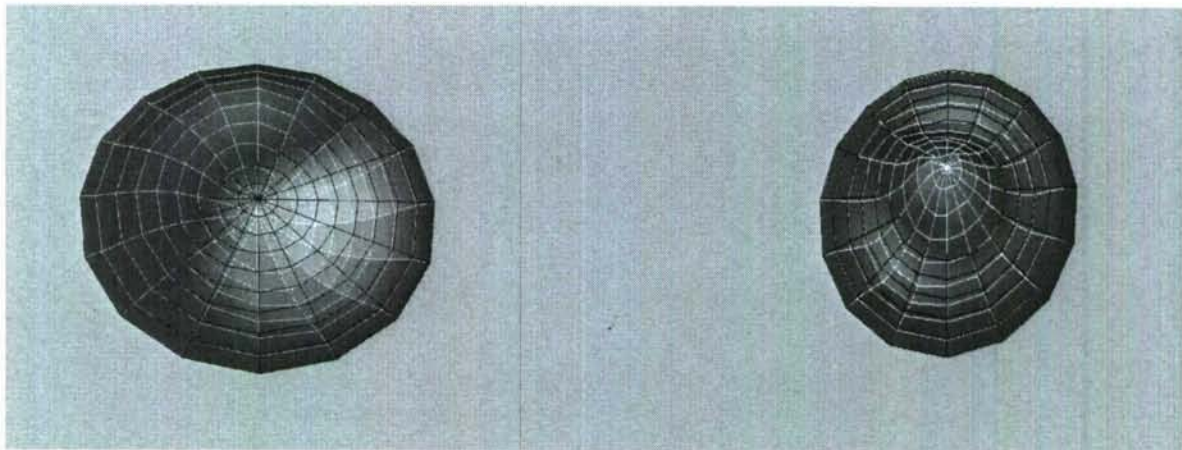


Figure 9 Example of measured eigenmode shape of circular membrane for the (1,1) mode at 78Hz (left) and the (0,2) mode at 185Hz (right).

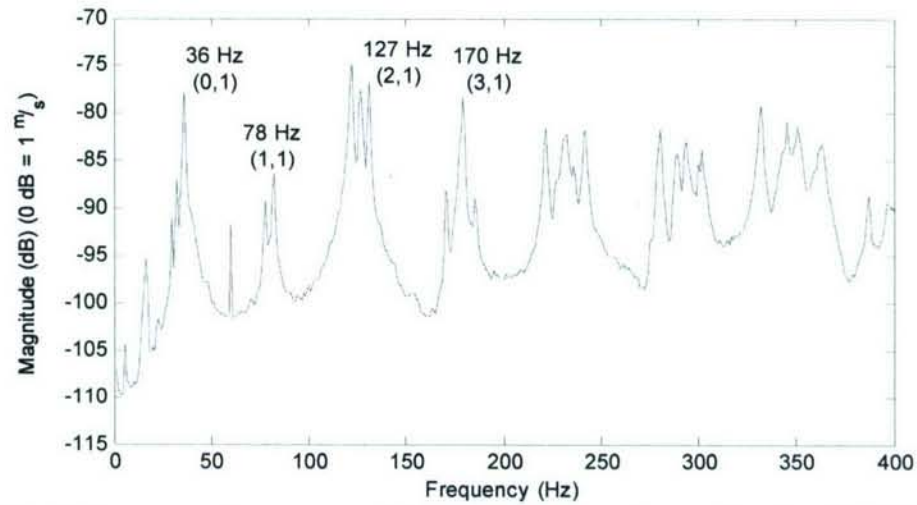


Figure 10 Spatially averaged auto spectral density of the membrane vibration ($T=182.5\text{N/m}$)

Frequency (Hz)	Mode (m,n)	In Vacuo Frequency (Hz)	Frequency Ratio	Amount of Air (cm)
36	(0,1)	137.38	0.26204	20.381
78	(1,1)	218.89	0.35633	11.022
127	(2,1)	293.28	0.43175	7.5275
170	(3,1)	364.48	0.46641	6.4335
185	(0,2)	315.35	0.58665	4.0665
241	(0,3)	494.36	0.48750	5.8892
284	(2,2)	480.85	0.59062	4.0147

Table 1: Frequencies and corresponding mode numbers for fluid loaded foil at 182.5N/m compared to the in vacuo frequencies.

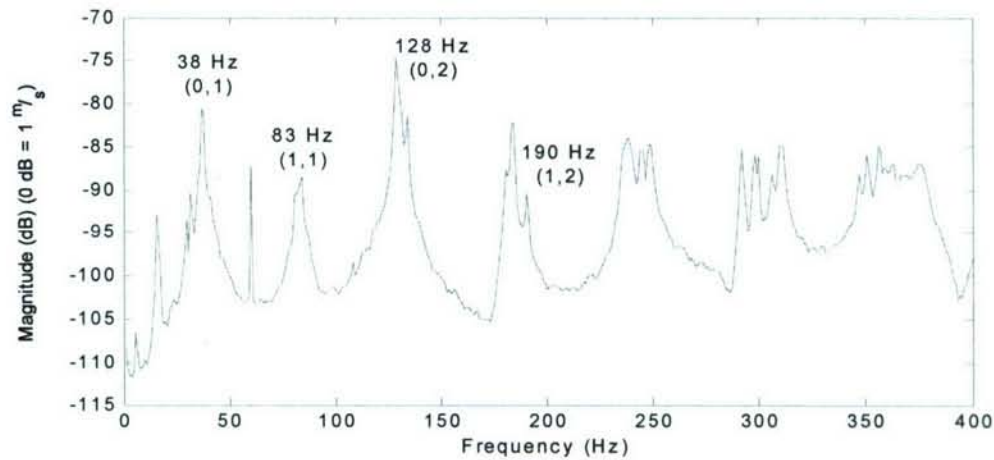


Figure 11 Spatially averaged auto spectral density of the membrane vibration ($T=255.4\text{N/m}$)

Frequency (Hz)	Mode (m,n)	In Vacuo Frequency (Hz)	Frequency Ratio	Amount of Air (cm)
38	(0,1)	162.55	0.23377	25.610
83	(1,1)	259.00	0.32046	13.628
128	(0,2)	373.12	0.34305	11.893
190	(1,2)	474.21	0.40067	8.7184
244	(0,3)	584.94	0.41714	8.0533
245	(2,2)	568.95	0.43062	7.5478
306	(1,3)	687.67	0.44426	7.0983
358	(0,4)	797.03	0.45607	6.7528

Table 2: Frequencies and corresponding mode numbers for fluid loaded foil at 255.4N/m compared to the in vacuo frequencies.

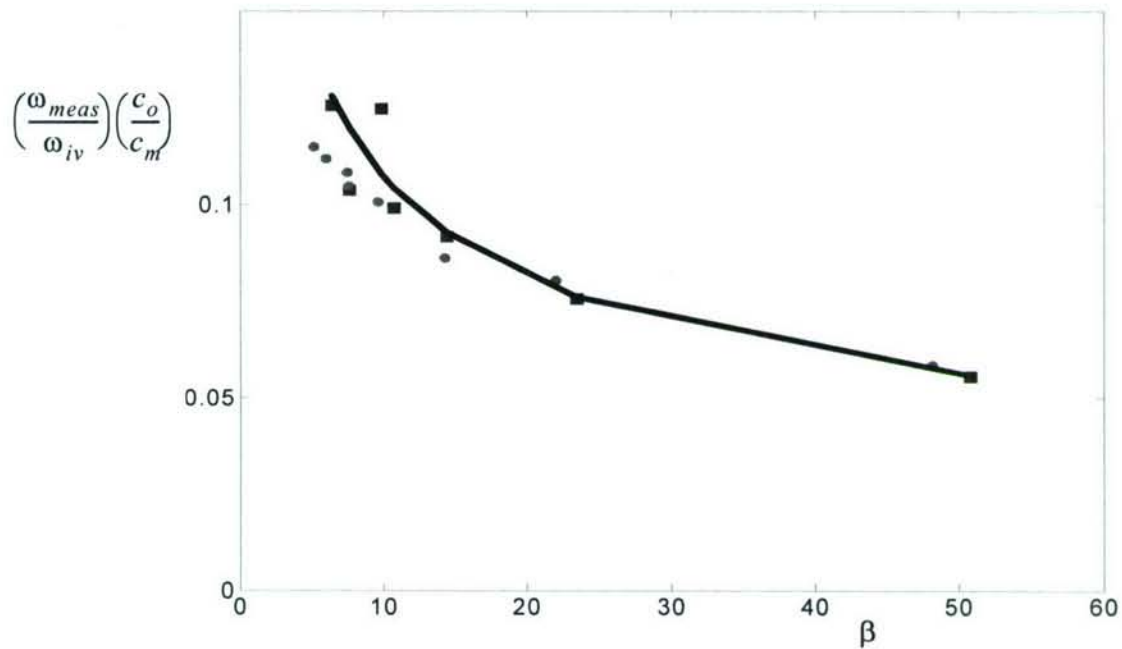


Figure 12 Ratio of the observed natural frequency to the in-vacuo frequency, normalized by the wave speed ratio (c_m/c_o) as a function of the fluid loading factor (β). The solid line represents the function $0.27(\beta^{-0.4})$ is shown only for visual reference.

3.2 Nickel Shell Apparatus

One of the significant results from this project is the development of a set of cylindrical test specimens that are very thin, yet do not have welds, seams, or other large scale imperfections that result from the manufacturing process. The purpose in developing these test shells was to provide the symmetry needed for simplified analysis of the structure.

The manufacture of the thin shells was as follows. First, an acrylic cylinder with 8.1 inch outer diameter was machined. The elastic shell was then created by electroplating pure nickel onto the acrylic. Note that a minute layer of gold was first sputtered onto the base cylinder in order to provide the electrical conductivity needed for the electroplating process. The time/current-density were monitored to provide a material that is essentially flawless and 0.0027 inches in thickness. Support ring (ribs) were mounted and glued to the nickel shell for structural support. Axial support struts were then placed between the ribs in order to prevent yielding or buckling of the thin shell during handling. The final step of the process required the submersion of the acrylic/nickel shell into an acidic solution in order to chemically remove the acrylic base material. Once all of the inner material was removed, the final product was removed from the solution and cleaned.

A total of four nickel duct sections were constructed. Two images of one of these sections is shown in Figure 13. The supporting apparatus shown provides the capability to pre-stress the material with axial tension without applying unwanted torsional pre-stress. The system uses linear bearings and two ground rods that support the rib sections. Four linear springs are compressed in order to provide a desired axial tension. The linear bearings attached to the spring section are held in place (axially) using two force transducer buttons that provide an accurate measurement of the applied tension.

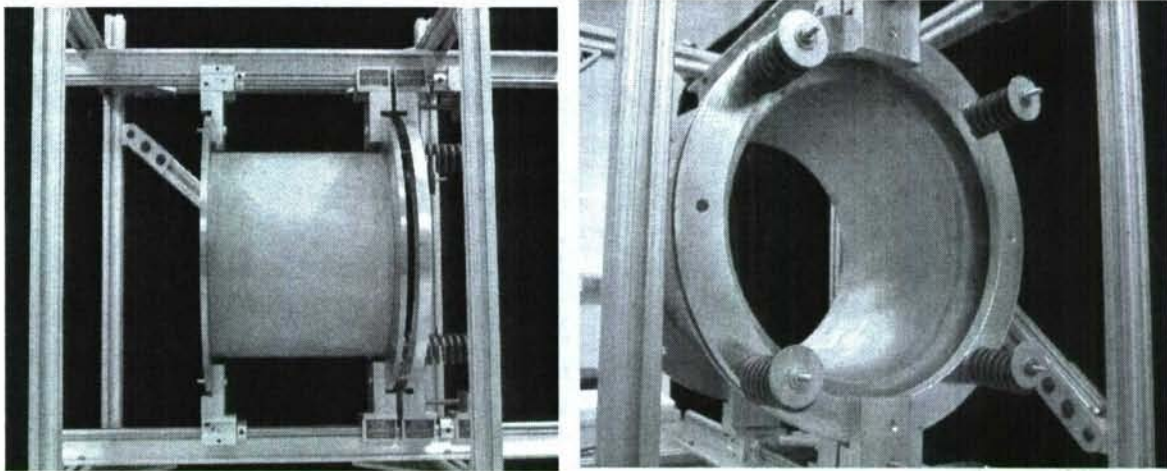


Figure 13 Images of a nickel duct section under tension

3.3 Ducted Rotor System

A new ducted rotor facility was developed for the experiments that will be described in later Sections. The intent of the facility was to create boundary conditions for the flow-structure-acoustic problem that captured the complexity of the physical mechanisms involved with these types of engineering systems, while maintaining the symmetry and simplicity that allows the problem to be studied analytically.

A schematic of the ducted rotor system with rigid walls is shown in Figure 14. The duct was constructed from PVC with a machined inner diameter of 206 mm and a wall thickness of 6.7 mm, and supported by a vibration isolation pad. A center cylinder extended upstream of the duct inlet and downstream of the outlet to create an annular flow passage. The inlet flow was conditioned using a single layer of a “cheesecloth” type thin fabric with negligible acoustic impedance stretched over a cylindrical wire frame. A compact servo motor was housed in the center cylinder to direct drive the rotor at the desired speed. The upstream cylinder and motor were supported by eight streamlined struts. The downstream center cylinder was cantilevered from a support structure beyond the duct outlet (not shown). The rotor was a ten-bladed propeller previously used by Sevik, with diameter $D = 0.203$ m, constant blade chord $C = 0.025$ m and maximum thickness of 2.4 mm, with straight blades incorporating twist only. The rotor operated with a tip gap equal to 5% of the blade chord. The length of the duct was variable, as was the position of the rotor from the duct inlet.

The turbulent boundary layer created on the sidewalls of the duct upstream of the rotor plays an important role in the modeling and prediction of the acoustic sources. The velocity field was characterized using a single component hot-wire anemometer connected to a radial traverse system. Time series of the velocity were measured at a range of radial and axial positions. The mean and RMS of velocity from these measurements is shown in Figure 15. The data indicate the expected acceleration effects in the very-near entrance region, followed by a typical boundary layer that grows smoothly in the downstream direction. These data will be used in later sections in defining the acoustic source strength with both rigid and elastic shells.

Example sound spectra are shown in Figures 16 and 17. A number of distinctive features were observed in the spectra. For example, multiple “organ pipe” type resonances can be observed at fixed frequencies in Figure 16. The spectra are plotted with frequency normalized by the blade passing frequency in Figure 17. These data show distinct features at integer multiples of the blade

rate. Significant broad band sound was also observed at high frequencies. The radiated sound was found to be dependent on the rotor flow coefficient. The duct flow rate was decreased by applying variable restriction in the form of thin fabric with negligible effect on the acoustic field to the duct exit, and increased by attaching the outlet of the duct to the anechoic wind tunnel blower.

The rotor casing and duct were segmented such that individual sections could be removed and replaced with one or more of the elastic shell sections. Model schematics of the ducted rotor with the nickel shell and tensioning apparatus are shown in Figure 18. The right-most picture shows the shell with a rigid walled exit contraction. This configuration allows the internal pressure of the duct to be controlled. Specifically, the flow rate generated by the rotor is accelerated through the contraction and exits as a jet at atmospheric pressure. The acceleration therefore provides an internal mean pressure that can be controlled by either changing the flow rate through the duct, or by changing the contraction ratio. This feature, along with the variable tension provided by the supporting mechanism, allows for some control of the shell's natural frequencies by changing the static pre-stress.

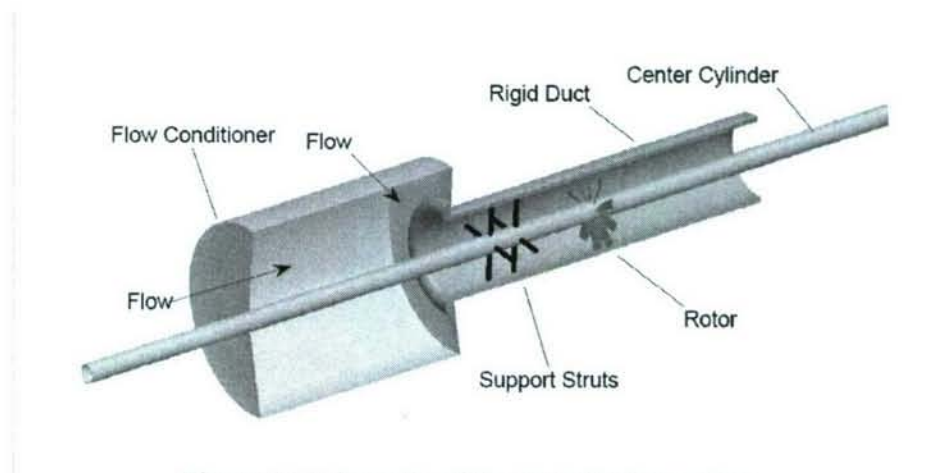


Figure 14 Schematic of the ducted rotor system

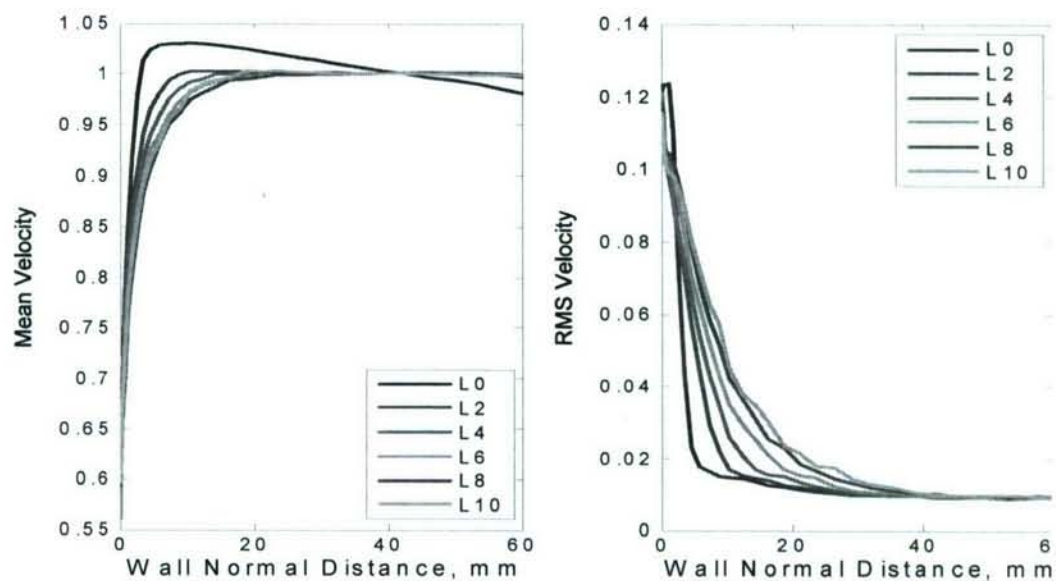


Figure 15 Characterization of the duct inflow boundary layer by the mean velocity profiles (left) and the RMS of velocity profiles (right). The location numbers noted in the legend represent the distance (in inches) from the inlet.

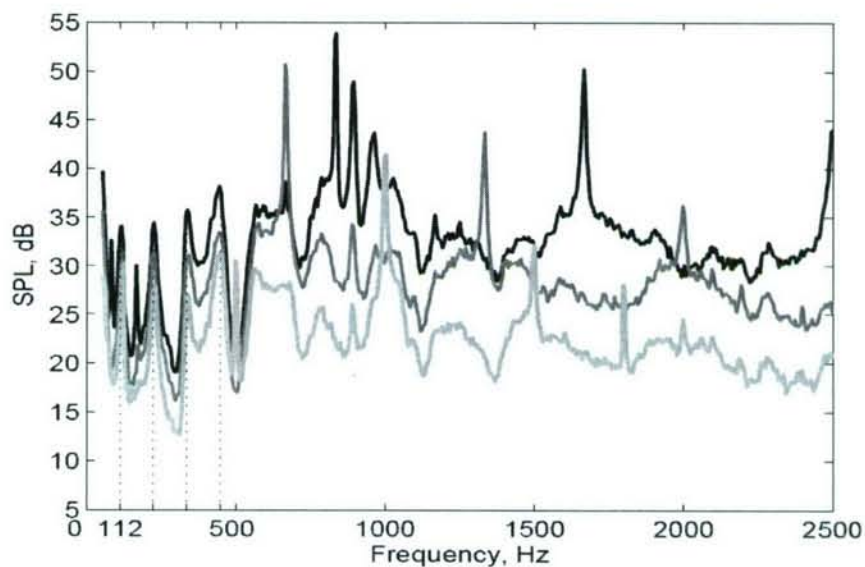


Figure 16 Measured sound spectra for the ducted rotor at three rotational speeds.

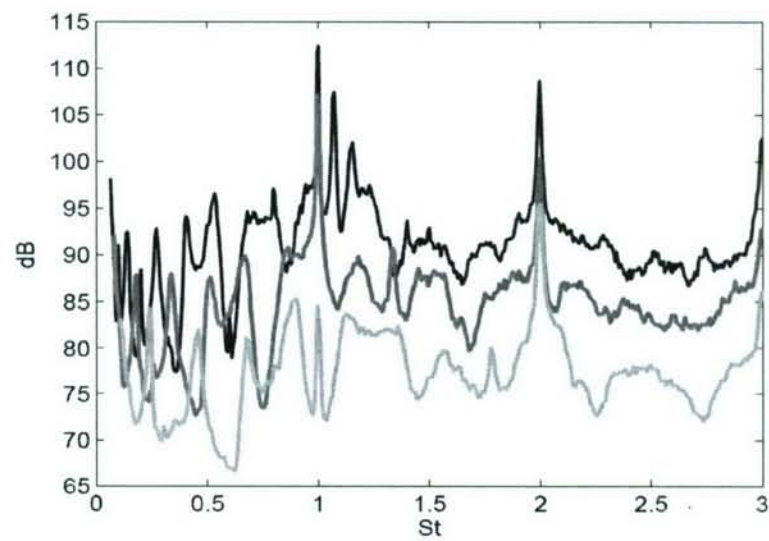


Figure 17 Measured sound spectra for the ducted rotor with the frequency normalized by the blade passing frequency.

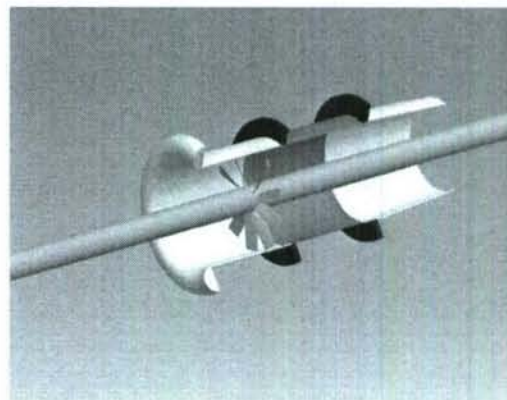
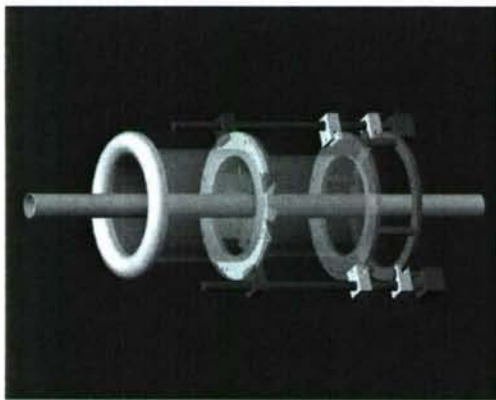


Figure 18 Model schematic of ducted rotor with nickel section and tensioning device (left), and rotor/shell with exit contraction (right).

4. RECIPROCITY MEASUREMENT OF ACOUSTIC TRANSFER FUNCTIONS

The prediction of structurally and aerodynamically generated sound requires detailed knowledge of both the distribution of sources as well as the transfer of acoustic energy from the source to a location of interest. The propagation of acoustic waves can be found from analytical methods or numerical solutions when the boundary conditions are sufficiently simple. However, complex geometries involved with engineering systems can result in significant difficulty for these approaches, particularly when surfaces are vibrationally active, when sound absorbing materials are used, or when features of the geometry are complicated. The present communication describes a reciprocal experiment using a miniature dual-microphone probe. The measurements allow the calculation of the frequency dependent Green's function and its spatial gradient, which represent the acoustic transfer functions for monopole and dipole sources, respectively.

A point monopole with a given frequency (ω) can be represented by its complex source strength, $S(x_s)$. This results in an acoustic pressure at location x_o that is given by the solution to the Helmholtz equation (Pierce, 1989):

$$(\nabla^2 + k^2)p(x_o) = -4\pi S(x_s)\delta(x_o - x_s), \quad (3)$$

where k is the acoustic wavenumber. This expression is valid if the fluid is at rest, and approximately true at low Mach number. The Green's function $G(x_o, x_s)$ is defined as the solution to equation (3) for a unit source strength ($S=1$). The acoustic pressure can then be determined by:

$$p(x_o) = G(x_o, x_s)S(x_s). \quad (4)$$

That is, the function G represents the "transfer function" between the acoustic source at location x_s and the acoustic pressure at location x_o .

Similarly, consider a single dipole with vector valued amplitude $\vec{D}(x_s)$. The inhomogeneous Helmholtz equation can be written as

$$(\nabla^2 + k^2)p(x_o) = -4\pi \vec{D} \cdot \nabla \delta(x - x_s). \quad (5)$$

The acoustic pressure field is given as

$$p(x_o) = \vec{D}(x_s) \cdot \nabla G(x_o, x_s). \quad (6)$$

It will be useful to consider a dipole with an assumed fixed vector direction, such that a new function can be defined as:

$$G_D(\mathbf{x}_o, \mathbf{x}_s) \equiv (\vec{D} \cdot \nabla G) / |\vec{D}| \quad (7)$$

The radiated sound can now be given by

$$p(\mathbf{x}_o) = G_D(\mathbf{x}_o, \mathbf{x}_s) |\vec{D}(\mathbf{x}_s)| \quad (8)$$

The function $G_D(\mathbf{x}_o, \mathbf{x}_s)$ therefore represents the acoustic transfer function for dipoles with a fixed direction. This representation is particularly useful in applications where aeroacoustic source distributions are the subject of interest. The specific example to be considered later in this paper is that of a short, three dimensional duct section. A low-speed rotor (such as a fan or compressor) operating in such a duct section will create a distribution of dipole-like sources that lead to far field sound. Estimates of $|\vec{D}|$ can be obtained in this example by calculating the unsteady lift on the blades due to approach turbulence (see, e.g., Goldstein, 1976). Equation 6 (or its integral when \vec{D} is represented as a force per unit volume) provides a simple method for predicting the far field sound pressure level when G_D is known.

The duct and rotor combination described can also be considered as an acoustic inverse problem. Specifically, acoustic measurements can be made using a single microphone located in the far field. In this example, an independent estimate of the acoustic transfer function, G_D , will allow the determination of the net dipole source strength.

A direct measurement of G would require the placement of a monopole type source at a desired location (\mathbf{x}_s), and a microphone located at the desired observation location (\mathbf{x}_o). In practice, however, it is not generally possible to create an omnidirectional point monopole, particularly when the geometry of interest is small or difficult to access. Furthermore, the source strength of such a device could be modified by strong near field pressures resulting from rigid and vibrating surfaces in the region of the source. The direct measurement of G_D would require a known amplitude ideal dipole to be placed at \mathbf{x}_s which is not feasible in practice.

A method for circumventing these issues is to use a reciprocal technique. The principal of acoustic reciprocity was first proposed by Helmholtz in 1860, and later given by Rayleigh in 1873. A

general proof of these concepts was later given by Lyamshev (1959) which utilized Green's formula to show that reciprocity was valid for linear, self-adjoint differential operators. Since that time, a number of authors have provided further refinements to both the theory and experimental application. For example, Steenhoek and Wolde (1970) and Belousov and Rimskii-Korsakov (1975) both provide detailed discussions on the application of reciprocity to mechanical-acoustical systems. Fahy (1995, 2003) provided a review of the development of reciprocity as well as detailed schematics of the reciprocal relations for a large number of vibroacoustic scenarios.

The use of reciprocity for aeroacoustic applications is significantly more rare. Presumably this is because of the multi-pole nature of rigid body aeroacoustic problems. In the papers by Fahy (1995, 2003) the reciprocity equations for both monopole and dipole point sources embedded in a fluid were given. It is these relations that will allow for the experimental determination of the functions G and G_D . To the author's knowledge, this communication presents the first application of Fahy's dipole form of acoustic reciprocity for experimental measurements.

Although the basic acoustic relationships described in this paper are well understood, the experimental methodology and associated uncertainty considerations are not. The techniques described herein show that relatively simple experiments can be conducted to determine both G and G_D simultaneously. The measurement uncertainty will be first considered analytically, and then demonstrated using results obtained in a free space (anechoic) environment. An example experiment will also be described which illustrates the use of the technique in measuring the monopole and dipole acoustic propagation from inside of a short, rigid duct section to a location outside the duct.

4.1 Application of monopole and dipole reciprocity

A schematic of monopole and dipole reciprocity adapted from Fahy (1995) is shown in Figure 19. The geometry is arbitrary, and shown here as a short cylindrical duct as it pertains to the example used later in this paper. For point monopoles, the spatial locations of the source and the microphone can simply be switched. The Green's function as defined in equation 4 can then be calculated as:

$$\frac{p(\mathbf{x}_o)}{S(\mathbf{x}_s)} = \frac{p(\mathbf{x}_s)}{S(\mathbf{x}_o)} \quad (9)$$

where the term on the left represents the desired Green's function, and the term on the right is the reciprocal representation that is measured by placing a microphone at \mathbf{x}_s and a calibrated omnidirectional acoustic source at \mathbf{x}_o .

The reciprocal relationship for dipoles is given as:

$$\frac{|\dot{h}(\mathbf{x}_o)|}{|\vec{D}(\mathbf{x}_s)|} = \frac{|\dot{h}(\mathbf{x}_s)|}{|\vec{D}(\mathbf{x}_o)|}. \quad (10)$$

That is, the ratio of the acoustic particle velocity magnitude, $|\dot{h}(\mathbf{x}_o)|$, to the dipole source magnitude, $|\vec{D}(\mathbf{x}_s)|$, is fixed when the locations \mathbf{x}_o and \mathbf{x}_s are switched. This is true only if the directions of the velocity and dipole vectors are maintained as shown in Figure 19.

Two important simplifications of equation 8 can be made if \mathbf{x}_o is located in the far field. First, the acoustic velocity can be represented by

$$u(\mathbf{x}_o) = p(\mathbf{x}_o)/\rho c. \quad (11)$$

Second, for wavenumber vectors parallel to the line segment connecting \mathbf{x}_o and \mathbf{x}_s , the sound field incident upon the geometry from a dipole located at \mathbf{x}_o is identical to that of a monopole whose strength is given by:

$$S(\mathbf{x}_o) = ik|\vec{D}(\mathbf{x}_o)|. \quad (12)$$

This step is important since an ideal dipole is not easily generated experimentally. That is, equation (12) allows the acoustic source to take the form of a monopole which can be purchased or constructed from a simple speaker.

The final step in formulating the reciprocity experiment for dipoles is the measurement of the particle velocity $u(\mathbf{x}_s)$. The present method used a two microphone probe similar to those typically used for sound intensity measurements. Specifically, the acoustic particle velocity was estimated using a discrete representation of the linearized Euler equation:

$$u(\mathbf{x}_s) = \frac{1}{i\omega\rho}\frac{\Delta p}{\Delta x}, \quad (13)$$

where the pressure gradient was measured with a closely spaced pair of miniature microphones. The vector orientation of the original dipole source at \mathbf{x}_s is preserved by positioning of the microphone pair.

The magnitude of G_D can then be calculated by combining equations 8 and 10 through 13:

$$G_D = \rho c \frac{|\hat{u}(\mathbf{x}_o)|}{|\hat{D}(\mathbf{x}_s)|} = \rho c \frac{|\hat{u}(\mathbf{x}_s)|}{|\hat{D}(\mathbf{x}_o)|} = \frac{1}{S(\mathbf{x}_o)} \frac{\Delta p(\mathbf{x}_s)}{\Delta x} \quad (14)$$

The implementation of dipole reciprocity therefore requires a monopole sound source with known magnitude placed at \mathbf{x}_o , and a dual-microphone probe located at \mathbf{x}_s .

4.2 Experimental technique

A probe was designed and constructed that allowed for the simultaneous measurement of both G and G_D . The probe and its support were designed to be small enough to be easily manipulated and traversed in a given experimental apparatus without creating significant changes in the local acoustic field. Additionally, the probe was designed to hold two microphones at a fixed separation (Δx) in order to recover an estimate of the pressure gradient $\Delta p(\mathbf{x}_s)/\Delta x$. The orientation of these two sensors needed to be articulated to match a specified dipole vector direction.

Figure 20 shows a picture of the assembled probe. The sensors were Knowles FG series electret condenser microphones commonly used in hearing aids. The diaphragm size was 0.7mm, with a nominal casing diameter of 2.56mm. The microphones were mounted on a U-shaped articulating arm. The microphone spacing was fixed at $\Delta x = 18.5\text{mm}$. The arm was mounted to a support sting constructed from 6.35mm diameter aluminum rod. The ability to rotate the sensor pair with two degrees of freedom allowed for alignment with a given direction.

Calibration of the two miniature microphones utilized a plane wave tube constructed from a 0.75m length of extruded PVC pipe with an inner diameter of 40.4mm. The cut-on frequency for non-planar waves was 4.87kHz. A calibrated ACO Pacific, Inc. 1/4" free-field microphone (model 7016PM with 4012 pre-amplifier) was used to measure the plane wave amplitude at the same axial location as the reciprocity probe. Broadband acoustic excitation was provided by a small speaker located at the end of the tube. Analog signals were converted to digital voltage time series and recorded for post-processing. The magnitude and phase of typical calibration functions for the two microphones, $H_1(\omega)$ and $H_2(\omega)$ are shown in Figure 21. The microphone pair was

observed to be relatively phase matched over the frequency range shown. The average phase mismatch was 0.05 radians.

The measurement of $G(\mathbf{x}_s, \mathbf{x}_o)$ was executed as follows. A B&K omnisource (Type 4295) speaker was positioned at the desired \mathbf{x}_o location. The miniature probe was located at \mathbf{x}_s . The same reference microphone used during calibration was placed in the free field which allowed for the determination of the source strength using the free space relation:

$$|\hat{S}(\omega)| = R \sqrt{A_{p_{ref}}(\omega) \Delta\omega} \quad (15)$$

where R is the radial distance from the reference microphone to the acoustic source, and $A_{p_{ref}}$ is the autospectral density of the reference pressure¹, p_{ref} . $G(\mathbf{x}_s, \mathbf{x}_o)$ was calculated by combining equations 4, 9 and 15:

$$G(\mathbf{x}_o, \mathbf{x}_s) = \frac{1}{R} \sqrt{\frac{A_p}{A_{p_{ref}}}}, \quad (16)$$

where the frequency band-width, $\Delta\omega$, used in the spectral processing cancels so long as they are the same for the evaluation of the two spectral densities.

Similarly, equations 14 and 15 can be combined to obtain a simple form for the dipole function:

$$G_D(\mathbf{x}_o, \mathbf{x}_s) = \frac{1}{\Delta x R} \sqrt{\frac{A_{\Delta p}}{A_{p_{ref}}}}. \quad (17)$$

where the autospectral density of the pressure difference, $A_{\Delta p}$ was obtained from

$$A_{\Delta p} = A_{p_1} + A_{p_2} - 2\text{Re}(A_{p_1 p_2}) \quad (18)$$

and $A_{p_1 p_2}$ is the cross spectral density of the microphone pressures.

The uncertainty in the measurement of $G(\mathbf{x}_s, \mathbf{x}_o)$ was determined by estimating potential errors in the reference microphone and the probe microphone calibrations. For the present measurements, the reference microphone was calibrated in a standard B&K pistonphone. The resulting error was estimated to be less than 0.2dB based on the calibration uncertainty. Additionally, if the experi-

1. The definition and calculation algorithms for the autospectra density functions are given by Bendat and Piersol (2000). Note that the symbol G_{pp} is commonly used for auto spectral density. However, G is reserved here for the acoustic Green's function, and the notation A_p will be used to represent spectral quantities.

ments are not conducted in a fully anechoic environment, the use of the free space Green's function in equation 15 will result in a bias error in the acoustic source magnitude. Issues related to the assumption of anechoic boundary conditions will be discussed in the following section.

Uncertainty in the measurement of G_D is related to the measurement of the particle velocity using the two-microphone technique. This is identical to the issues considered for common intensity measurements, and detailed uncertainty analysis can be found in (Seybert 1981, Fahy 1989, Wong 1991, Jacobsen & de Bree 2005). For the present investigation, the uncertainty was found to be controlled by two factors. At low frequency, any phase mismatch in the sensors that was not properly accounted for in calibration leads to large errors. At high frequency, the approximation

$\frac{\partial p}{\partial x} \approx \frac{dp}{dx}$ becomes invalid. This type of error is referred to as systematic error by Fahy (1989).

Other sources of error such as electronic noise and calibration amplitude factors were found to be substantially smaller than the phase mismatch and systematic errors.

The phase error introduced when measuring the acoustic particle velocity can be found by starting from Euler's equation for a harmonic pressure field:

$$u_{rms}^2 = \frac{p_{rms}^2}{\omega \rho \Delta x} (1 - \cos \phi) \quad (19)$$

where ϕ is the true phase difference in the pressure at two points spaced Δx apart. A normalized uncertainty can be found by dividing by the plane-wave reference values and taking the partial derivative with respect to ϕ :

$$e_\phi \equiv \frac{\partial}{\partial \phi} \left(\frac{u_{rms}}{p/\rho c} \right) \delta \phi = \frac{1}{2k\Delta x} \frac{\sin(k\Delta x)}{\sqrt{1 - \cos(k\Delta x)}} \delta \phi \quad (20)$$

where $\delta \phi$ is the phase mismatch, and the phase $\phi = k\Delta x$. This error is shown in Figure 22 using $\delta \phi = 0.05$ radians. This value was considered to be a conservative estimate of the phase uncertainty based on repeatability and scatter in the calibration measurements.

The normalized systematic error related to the finite difference approximation of $\partial p / \partial x$ is given by Fahy (1989) as

$$e_{sys} = \frac{\sin(k\Delta x/2)}{k\Delta x/2} - 1 \quad (21)$$

and is also shown in Figure 22.

The uncertainty defined by equations 20 and 21 clearly define a range of $k\Delta x$ for which the measurement technique will be viable. A maximum normalized error of 0.6 (2dB) limits the technique to the range $0.057 < k\Delta x < 4.3$. The microphone spacing used in the present measurements is $\Delta x = 18.5\text{mm}$, which corresponds to a frequency range of $170\text{Hz} < f < 12.6\text{kHz}$. However, as noted earlier, the cut-on frequency of the plane-wave tube used for calibration was 4.87kHz . The true usable frequency range of the probe for the measurement of G_D was then $170\text{Hz} < f < 4.87\text{kHz}$.

4.3 Free space measurements

Measurements of G and G_D were obtained in an anechoic environment in order to provide a direct assessment of the technique and its uncertainty. The data were collected in an anechoic chamber with dimensions 9.1m by 7.3m by 3.6m. Fiberglass wedges with 0.6m depth provided acoustic absorption at frequencies above 100Hz. A B&K omnisource (Type 4295) was placed in the room and its location designated as x_o . The location of the reciprocity probe, x_s , was 1.7m from the source. The probe axis was aligned radially from the source. That is, the vector direction defined by the two microphones was parallel to \hat{k} . The omnisource speaker was driven by a white noise signal generated using a Stanford Research Systems function generator (model DS360) and amplified through a B&K power amplifier (Type 2716). The reference microphone was located 1.3m from the source. The sound pressure level at the x_s location was approximately 68dB. Time series data were recorded from the two probe microphones simultaneously with the reference microphone and saved for post processing.

As noted earlier, reflections that result from incomplete absorption of the sound by the fiberglass wedges can lead to two types of bias error in the measured transfer functions. First, reflected sound that is incident on the x_s location will result in a positive bias in both G and G_D when compared to the free space conditions. Similarly, reflected sound that is incident on the p_{ref} location will result in a negative bias in G and G_D . Initial measurements indicated that these room reflections would result in 2 to 5 dB of error. To cancel the effect of these reflections, the measurements described above were repeated at five different locations within the anechoic room, and the resulting functions were averaged.

The analytic solutions for G and G_D in free space are given by

$$G(\mathbf{x}_o, \mathbf{x}_s) = \frac{e^{ik|\mathbf{x}_o - \mathbf{x}_s|}}{4\pi|\mathbf{x}_o - \mathbf{x}_s|} \quad (22)$$

and

$$G_D(\mathbf{x}_o, \mathbf{x}_s) = \frac{k \cos(\theta) e^{ik|\mathbf{x}_o - \mathbf{x}_s|}}{4\pi|\mathbf{x}_o - \mathbf{x}_s|} \quad (23)$$

respectively (Pierce, 1989). Note that θ is the angle between the wavenumber vector and the line segment defined by the two probe microphones. As described before, $\theta = 0$ degrees was used for the measurement. The free space functions given in equations 22 and 23 are shown in Figure 23 along with the experimentally determined values. The values of G and G_D are shown on a dB scale defined by $10\log_{10}(G)$ referenced to 1m^{-1} and $10\log_{10}(G_D)$ referenced to 1m^{-2} , respectively. The difference between the experimental and analytical values was found to be within $\pm 3\text{dB}$. The bias in the monopole measurement over the valid frequency range was 0.4dB with a maximum error of -3dB measured at 4.32kHz . The average bias in the dipole measurement was 0.5dB over the valid frequency range. The bias was 0.7dB over the frequency range $100\text{--}400\text{Hz}$. The maximum error was 3dB measured at 120Hz .

4.4 Application to finite duct acoustics

The motivation for the development of the present experimental technique was the study of aeroacoustic sources in low speed rotors operating in a short duct section. The study of the radiated sound from such devices is complicated by the presence of end reflections, organ pipe resonance, cut-on of higher order modes, and the acoustic interaction of the duct ends from outside the duct. It is therefore of interest to present initial results from these studies to highlight the utility of the developed measurement technique.

A schematic representation of the duct is shown in Figure 24. The duct walls were constructed from extruded PVC with a machined inner radius $a = 0.103\text{m}$ and a wall thickness of 6.35mm . The length of the duct was $6a$. A partial flange with 25.4mm outer diameter was placed at both ends of the duct as shown. The location of \mathbf{x}_s was centered both axially and radially in the duct, and the vector orientation was aligned with the duct axis. The location of \mathbf{x}_o was 1.31m from the duct center along the duct centerline.

The measured functions G and G_D are shown as a function of frequency in Figure 25. The frequency was normalized by the organ-pipe resonance frequency:

$$f_o = \frac{c}{2L_{eff}} \quad (24)$$

where $L_{eff} = L + 2 \cdot 0.611a$ is the effective length of the duct using the end correction factor of Levine and Schwinger (1948). Also, shown on the upper abscissa are the corresponding values of the nondimensional wavenumber, ka . Several notable features can be seen in the resulting transfer functions. First, both G and G_D are approximately the same overall magnitude as the free-space functions given by equations 22 and 23 (also shown in Figure 25). Also, local maxima are noted in $G(\omega)$ at odd multiples of f_o whereas $G_D(\omega)$ was found to exhibit these maxima at even multiples of f_o . This result is intuitive based on the symmetry of the geometry and the source location. At higher frequencies, a number of resonances and anti-resonances are noted. The numbered pairs noted on the figure correspond to the cut-on frequency of higher order duct modes.

4.5 Conclusions of Reciprocity Measurements

The acoustic transfer functions for single point monopole and dipole sources can be represented by the acoustic Green's function and its gradient, respectively. The experimental determination of these functions using a reciprocal technique has been demonstrated. This required the construction of a miniature dual-microphone probe that could be positioned at a desired source location. A basic uncertainty analysis as well as measurements conducted in a nominally anechoic environment have shown that the technique provides an accurate representation of the acoustic transfer functions, with a maximum error of about 3dB.

The motivation for developing the present technique was to provide a simple method for the determination of G and G_D in complex geometries for which analytical and numerical solutions are either difficult to obtain or not available. A demonstration of the technique using a short, rigid duct section was provided. Experiments are presently underway for investigating the dependence of G_D on the source location for complex rigid and elastic duct sections.

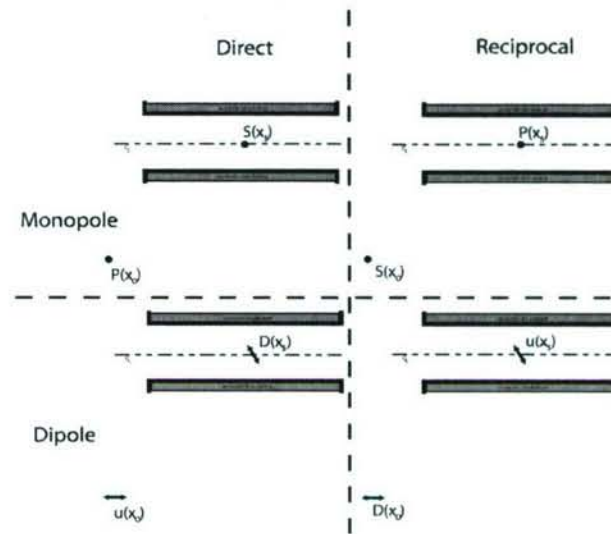


Figure 19 : Illustration of acoustic reciprocity applied in fluids. The example shows monopole (top) and dipole (bottom) point sources located in a cylindrical duct, with an observation point outside the duct.

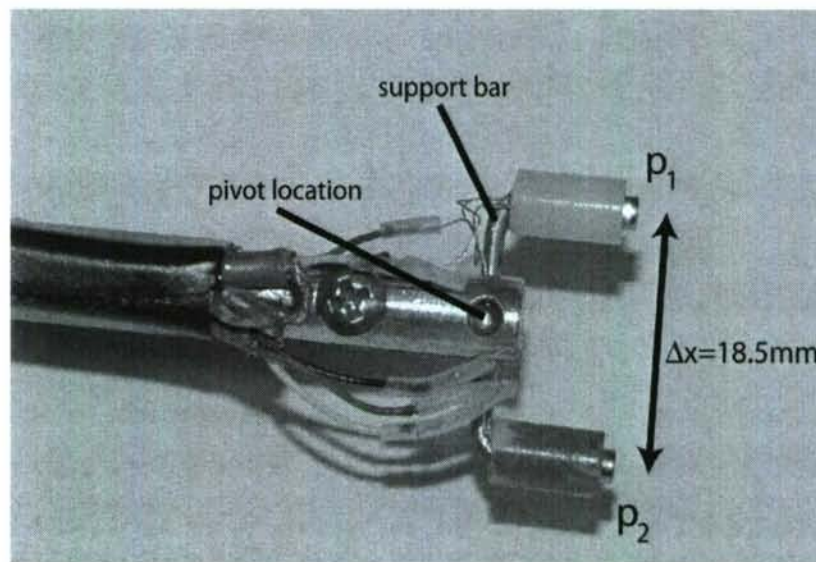


Figure 20 : Probe used in the measurement of the acoustic transfer function.

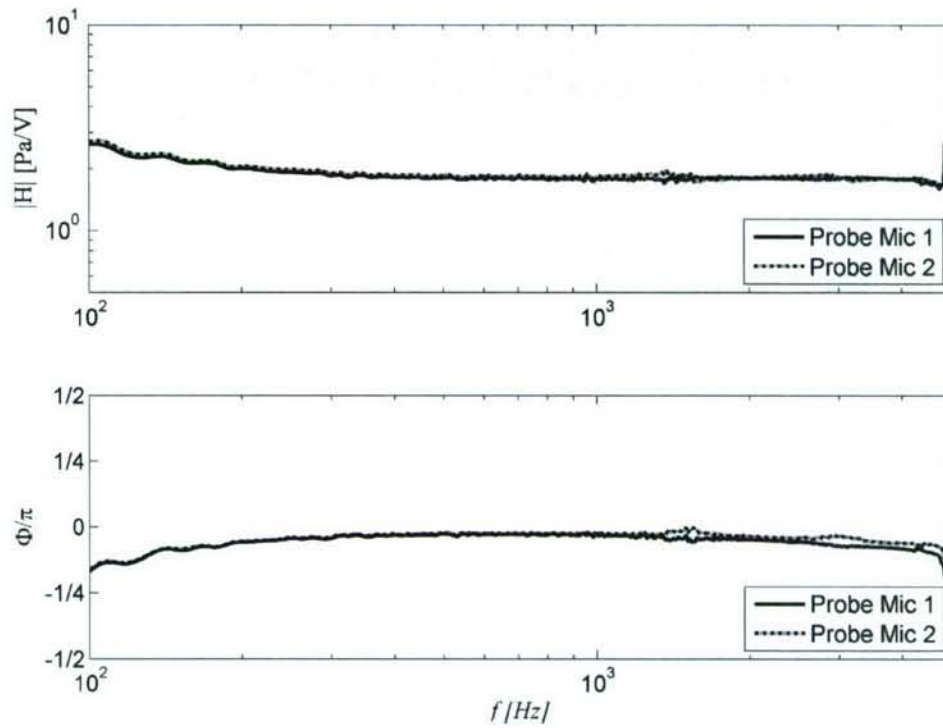


Figure 21 : Magnitude (upper) and phase (lower) of the calibration transfer functions for both probe microphones.

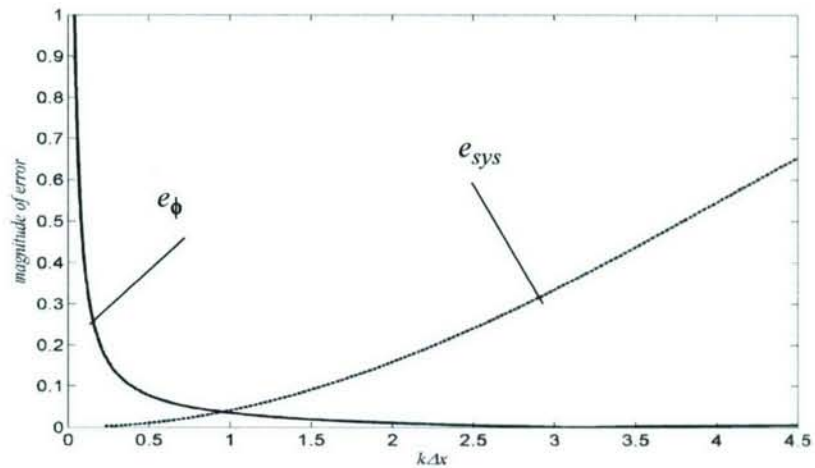


Figure 22 : Phase mismatch (solid) and systematic (dashed) normalized error in the measurement of acoustic particle velocity as a function of nondimensional wavenumber.

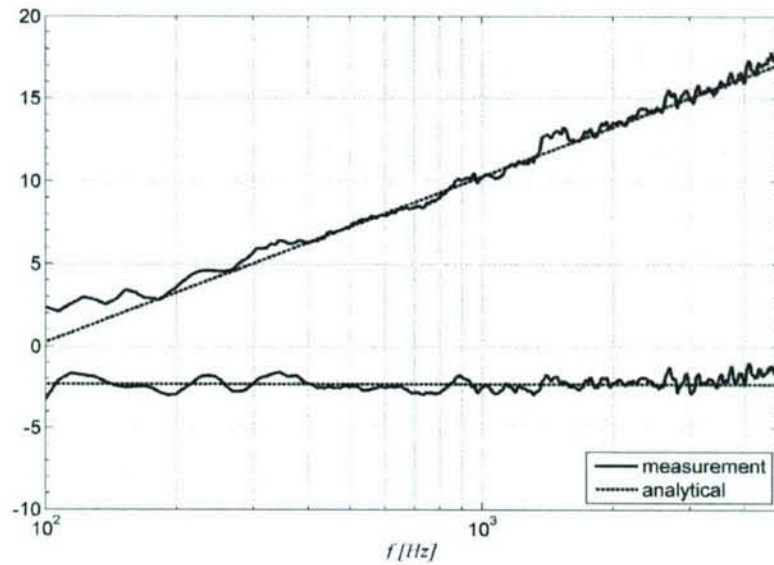


Figure 23 : Measurement of the monopole (lower) and dipole (upper) free space acoustic transfer function. Results presented as $10\log_{10}(G)$ (*re 1m⁻¹*) and $10\log_{10}(G_D)$ (*re 1m⁻²*), respectively.

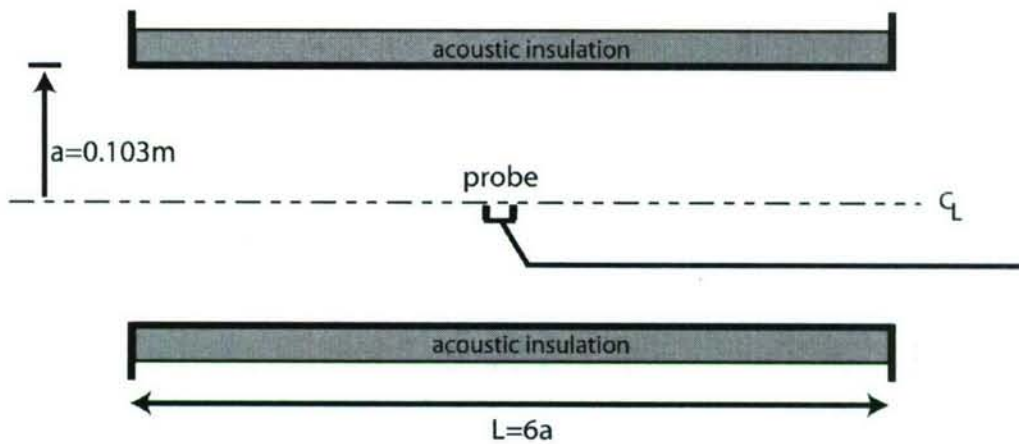


Figure 24 : Schematic illustrating the cylindrical rigid walled duct.

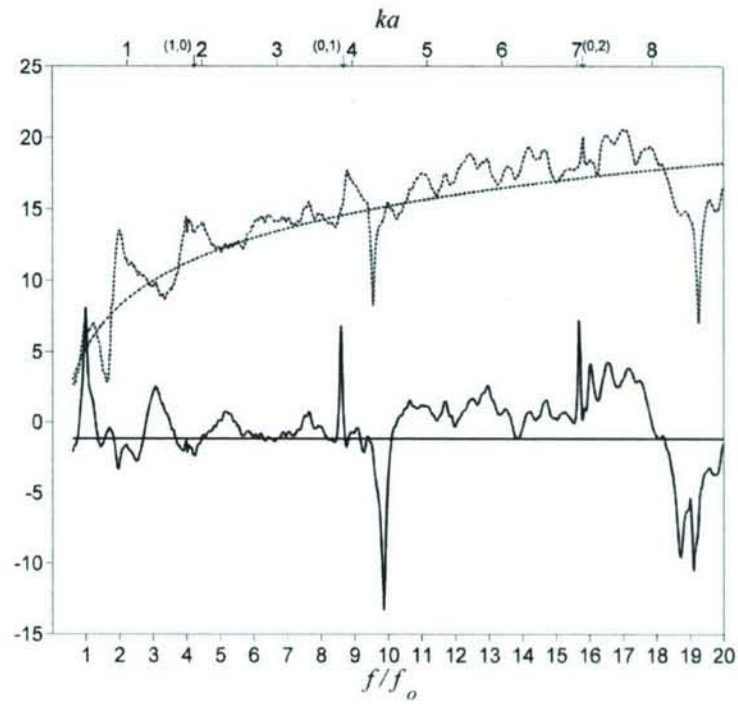


Figure 25 : Acoustic transfer function (in dB) between a monopole (solid) and dipole (dotted) located at the center of the duct and an observation point outside the duct on centerline. Smooth curves represent free-space solutions.

5.0 DETERMINATION OF DIPOLE SOURCE FROM SOUND DATA

This section describes a method for analyzing the sound radiated by a low-speed axial flow ducted fan. Specifically, an algorithm was developed that allows the determination of aeroacoustic source strength from microphone measurements. The radiated sound depends on both the sound generated by the rotor and the geometry of the surfaces surrounding the source region. These surfaces act to modify the spectral content of the sound as perceived by an observer outside of the duct. The fan was considered as a compact region of axial dipole sources, so that the radiated sound could be described as the product of a frequency-dependent unsteady force and an effective transfer function.

The microphone measurements presented in this section were acquired from the radiated sound generated by a ten-bladed fan operating inside a finite length rigid duct. Two fundamental frequencies were found to be inherent in the system, one based on the parameters of the sound source, and the other based on the geometry of the duct. As previous studies have found, these two frequency scales allow for the separation of the radiated sound into source and transfer function spectra. A unique method for determining these separate functions is presented, with the primary assumption that the aeroacoustic sources follow a power law relationship with rotor tip relative speed. The resulting algorithm was shown to effectively quantify the acoustic transfer function. A set of mathematically defined input functions was used to evaluate the efficacy of the separation method. Additionally, the ducted rotor system was operated over a range of flow rates to produce different sound sources, and the transfer function calculated by the algorithm was found to be independent of this source mechanism.

5.1 Background

Axial flow ducted rotors are important in numerous engineering applications, ranging from ventilation equipment to jet engines. The aerodynamic sound radiated from these devices is generated by a number of different mechanisms. At low speeds these mechanisms can be generally described by the response of the rotor to turbulent flows. For example, the interaction between the blades and turbulence in the approach flow is often referred to as “inflow noise.” Sound generated by the scattering of unsteady pressure that is created by the blades is often referred to as “self noise.” Many of these sound sources have received extensive analytical attention, much of which can be found in books by Blake (1986) and Goldstein (1975), and review papers by Morfey

(1973), Wright (1976) and Huff (1997). Some examples of more recent work include rotor interactions with the duct boundary layer (Moissev et al (1978)), tip vortex noise (Dunne and Howe (1997)), vortex sheet noise (Lee et al. (1993)) and ingested flow irregularities (Atassi et al. (1993)) and Kobayashi (1978).

The propagation of acoustic waves from rotating sources can be represented by an appropriate Green's function. Sound propagation from rotors operating in a free-space environment can be found by using a free-space Green's function with modifications for rotational effects (see, e.g., Blake, (1986)). Rotors operating in an effectively infinite duct invoke significantly more complex phenomena due to the effects of the source distribution on the excitation of various duct characteristic modes (see Doak (1973), Pierce (1981), and others). Noise that is radiated from rotors operating in a relatively short duct section exhibits additional complexity. For example, reflected waves from the duct ends will result in "organ-pipe" modes whose amplitude will depend on the location of the sources. The directivity and amplitude of sound radiated from each of the duct ends depends on the specific geometry of the duct inlet and exit sections. The Green's function for a finite length duct can not be determined analytically, and so must be measured or computed numerically. For example, Boundary Element Methods (BEM) are effective, but require significant computational resources, particularly for very complex geometries.

The relationship between the generated sound and the far field sound propagation can be simplified significantly by considering the sound source to be a net equivalent dipole force, $F(St, M_{tip})$. The tip relative Mach number M_{tip} is defined as the relative fluid velocity at the tip, U_{tip} , divided by the speed of sound in the working fluid, c_o . The independent frequency variable is described as a Strouhal number, in the manner of Weidemann, and defined as

$$St = \frac{f D_r \pi}{V_{tip} B} = \frac{f 2\pi}{\Omega B} = \frac{f}{\text{BPF}}, \quad (25)$$

where D_r is the rotor diameter, V_{tip} is the velocity of the rotor tip, f is the dimensional frequency and B is the number of rotor blades. For this definition the fundamental frequency of the sound source is taken to be the rotor blade passing frequency (BPF). The effects of the Green's function can be considered as a net transfer function, $T(He)$, where the Helmholtz number is defined as

$$He = \frac{fD}{c_0} = M_{tip} \times St \times \frac{B}{\pi}, \quad (26)$$

where D is the duct diameter.

The sound spectrum at a point in the far field is then given by the product, $P=F*T$. A complete derivation of this relationship and its assumptions is given in the following section. The focus of the present investigation is the use of experimental measurements of the radiated sound spectra, $P(f, M_{tip})$, from a variable speed ducted rotor to quantify the two functions $F(St, M_{tip})$ and $T(He)$. These measurements utilized a low speed fan operated inside of a short annular duct section inside an anechoic room. The radiated sound spectra were acquired using a single far field microphone at 11 rotational speeds.

A number of previous investigations have explored methods for separating source and transfer effects from measurements of the radiated sound, including Weidemann, Neise (1975), Bent and McLaughlin(1993), Mongeau, Thompson and McLaughlin (1995) and Zhang, Mongeau and Frankel (2002). A thorough discussion of these and other related papers will be given in the following section, along with the relevant background material. A new code was written for each of these methods and applied to the present data set. All of these methods were found to identify the majority of the spectral features in both F and T . However, in each case the results were found to exhibit spurious trends in both T and F . Specifically, these methods were found to result in functions for T that were strongly dependent on the spectral content of the sound source. It will be shown in this paper that these errors are likely due to a non-uniqueness issue that has not previously been described and accounted for. Specifically, it will be shown that large scale trends in either F or T can not be determined by simply varying the fan speed.

The main result of this section is the presentation of a new formulation and algorithm for determining F and T from the available measurements. The background and assumptions are provided in the following section. The efficacy of the algorithm was tested using a new experimental data base as well as mathematically defined input functions. The experiments included measurements with dramatically varied acoustic source spectra that resulted from throttling the fan into rotating stall. The functions T returned from these tests varied by less than 0.29 dB across most of the frequency range of interest.

5.2 Analytical background

5.2.1 Derivation of net equivalent product model

A system that can be characterized as a compact distribution of aeroacoustic sources surrounded by a specified geometry gives rise to the conceptual framework of a net equivalent point source and an effective acoustic transfer function. This concept can be formalized by starting with the Helmholtz equation,

$$\nabla^2 p + k^2 p = \nabla \cdot \mathbf{F} \quad (27)$$

where p is the Fourier transform of the acoustic pressure and k is the acoustic wave number. The form of the acoustic source on the right hand side is assumed to be dipole in nature where \mathbf{F} is an equivalent body force distribution. Eq. (27) is valid for low Mach number systems without monopole or quadrupole type sources.

The Helmholtz equation can be solved using a Green's function approach, where Green's function $g(\mathbf{r}, \mathbf{r}_o)$ is explicitly defined by

$$\nabla^2 g(\mathbf{r}, \mathbf{r}_o) + k^2 g(\mathbf{r}, \mathbf{r}_o) = -\delta(\mathbf{r} - \mathbf{r}_o), \quad (28)$$

and the boundary conditions appropriate to the system. For Eq. (28), \mathbf{r}_o is the source location, \mathbf{r} is the observer location, and δ is the Kronecker delta function. The solution to Eq. (28) can be written as a convolution of the Green's function over a volume V_o with the distributed sources $\nabla \cdot \mathbf{F}$, giving

$$p(\mathbf{r}) = \iiint_V [-\nabla_o \cdot \mathbf{F}] g(\mathbf{r}, \mathbf{r}_o) dV_o, \quad (29)$$

where the subscript on the operator ∇ denotes operation over the source region. A detailed derivation of Eq. (29) is available in Morse and Ingard (1968), among others. Integration by parts allows the far field solution to be rewritten as

$$p(\mathbf{r}) = \iiint_V \mathbf{F} \cdot \nabla_o g(\mathbf{r}, \mathbf{r}_o) dV_o. \quad (30)$$

If the source region is sufficiently compact the Green's function is separable into near and far field components. By using a coordinate system centered about the source region, this assumption of

compactness is denoted as $kr_o < 1$. For the present purposes, it will be useful to describe the Green's function as a product of three functions,

$$g(\mathbf{r}, \mathbf{r}_0) = \chi(\mathbf{r}) g_{fs}(\mathbf{r}, \mathbf{r}_0) g_{near}(\mathbf{r}_0), \quad (31)$$

where g_{near} is a dimensionless function of the source location that quantifies near-field effects such as Doppler shifts due to moving sources, geometrical non-compactness, and other effects due to both propagating and non-propagating components. The dimensions of the Green's function are retained in the free-space Green's function, $g_{fs} = \frac{1}{4\pi|\mathbf{r}-\mathbf{r}_0|} e^{ik|\mathbf{r}-\mathbf{r}_0|}$. The function χ accounts for amplifications and attenuations at particular frequencies due to the boundary conditions imposed by the rigid duct. A similar amplification function was introduced by Morse and Ingard (p. 320). As an example, if a harmonic monopole source were placed near an infinite rigid wall, the magnitude amplification function would be $|\chi| = 2$, indicating a doubling of the magnitude of the free-space Green's function across all frequencies.

Combining Eq. (30) with Eq. (31) gives

$$p(\mathbf{r}) = \chi(\mathbf{r}) \iiint_V \mathbf{F} \cdot \nabla_0 [g_{fs}(\mathbf{r}, \mathbf{r}_0) g_{near}(\mathbf{r}_0)] dV_0. \quad (32)$$

For the ducted rotor system considered in this paper, a radiation efficiency term can be partially derived by considering the acoustic sources to be axially oriented dipoles. This is appropriate so long as the stagger of the blades is such that the unsteady forcing on the rotor blades acts primarily in the axial direction. An equivalent source distribution can be defined as

$$\mathbf{F}(\mathbf{r}_0) = F_x(\mathbf{r}_0), \quad (33)$$

where the unsteady forces act only in the x -direction, that is along the axis of the duct, denoted with the subscript x . The gradient operator in Eq. (32) can be carried out giving

$$p(\mathbf{r}) = \chi(\mathbf{r}) \iiint_V F_x \cdot [\nabla_0 g_{fs}(\mathbf{r}, \mathbf{r}_0) g_{near} + g_{fs}(\mathbf{r}, \mathbf{r}_0) \nabla_0 g_{near}(\mathbf{r}_0)] dV_0. \quad (34)$$

The gradient of the free space Green's function in the far field is given as

$$\nabla_0 g_{fs}(\mathbf{r}, \mathbf{r}_0) = -[ik \cos \theta] g_{fs}(\mathbf{r}, \mathbf{r}_0), \quad (35)$$

where θ is the angle between the axis of the dipole forces and the vector between the source and the receiver, $\mathbf{r}-\mathbf{r}_0$. Substituting this in Eq. (34) gives

$$p(\mathbf{r}) = -\chi(\mathbf{r}) (ik) g_{fs}(\mathbf{r}) \cos \theta \iiint_V F_x \cdot \left[g_{near}(\mathbf{r}_0) + \frac{\nabla_0 g_{near}(\mathbf{r}_0)}{ik \cos \theta} \right] dV_0. \quad (36)$$

If $\mathbf{r}-\mathbf{r}_0$ can be approximated as $|\mathbf{r}|$, then g_{fs} can be removed from the integral above, which is appropriate now that the gradient operator has been evaluated and the dependence of g_{fs} on \mathbf{r}_0 is small. This gives

$$p(\mathbf{r}) = -\chi(\mathbf{r}) (ik) g_{fs}(\mathbf{r}) \cos \theta \iiint_V F_x \cdot \left[g_{near}(\mathbf{r}_0) + \frac{\nabla_0 g_{near}(\mathbf{r}_0)}{ik \cos \theta} \right] dV_0. \quad (37)$$

The auto spectrum of the acoustic pressure can be obtained by taking the expected value of Eq. (37) multiplied by its complex conjugate to obtain

$$\begin{aligned} \mathcal{P} = \overline{p^2}(\mathbf{r}) &= |\chi(\mathbf{r})|^2 k^2 |g_{fs}(\mathbf{r})|^2 \cos^2 \theta \iiint_{V_2} \cdot \iiint_{V_1} \overline{F_{i1} F_{i2}^*} \\ &\cdot \left[g_{near}(\mathbf{r}_{01}) + \frac{\nabla_{01} g_{near}(\mathbf{r}_{01})}{ik \cos \theta} \right] \left[g_{near}(\mathbf{r}_{02}) + \frac{\nabla_{02} g_{near}(\mathbf{r}_{02})}{ik \cos \theta} \right]^* dV_{01} dV_{02}. \end{aligned} \quad (38)$$

Similar forms of this expression have been derived previously by Blake (1986) and Zhang et al. (2002), among others. The derivation presented here is unique, however, due to the inclusion of the k^2 efficiency term and the function χ . The net equivalent product model can now be given by representing the spatial integral of the two point correlation of the distributed sources as a single source function F , yielding

$$\mathcal{P} = \mathcal{F} \cdot \mathcal{T}. \quad (39)$$

The use of the notation T for the acoustic transfer function is unique to the present communication, and is used to denote the combined variables

$$\mathcal{T} = |\chi(\mathbf{r})|^2 k^2 |g_{fs}(\mathbf{r})|^2 \cos^2 \theta \quad (40)$$

or

$$\log \mathcal{T} = \log k^2 + \log |g_{fs}|^2 + \log |\chi|^2 + \log \cos^2 \theta.$$

(41)

which is valid for a compact distribution of axial dipoles.

5.3 Separation of source and transfer functions

The utility of the linear source-filter model given by Eq. (39) is apparent both for analysis of experimental data and for the prediction of acoustic signatures from complex systems. A partial separation of F from T given a set of acoustic measurements P is possible because the acoustic sources are explicitly dependent on a frequency related to the fluid velocity, whereas the transfer function is related only to the geometry of the surrounding surfaces and the sound speed in the working fluid. Equation (39) can be given as

$$\log \mathcal{P}(f) = \log \mathcal{F}(St) + \log \mathcal{T}(He), \quad (42)$$

where it is now clear that Eq. (42) has been reduced to two terms and that F is dependent on St but not on He , while T is dependent on He but not on St .

Before considering specific methodologies for separating the source and transfer functions, it will be useful to develop some insight into the limitations of the analysis. Consider a velocity dependent source function, $F(St)$, which is broadband in nature, and a transfer function with a single, narrow band tone at a fixed frequency. An “organ-pipe” type of resonance, for example, could result in such a feature. As the fan speed increases, the radiated sound pressure would likely increase with rotational speed according to a power law. However, each of these measured spectra would exhibit the spectral feature due to the pipe resonance at the fixed frequency. Separating this feature of the acoustic transfer function from the source function is relatively straight forward in this case. In the converse of this example, consider a featureless transfer function, such as the free space Green's function, and a source spectra with a narrow band feature, such as a blade rate tone. In this case, varying the fan speed will result in radiated sound spectra in which the frequency of the narrow band feature is proportional to the rotor speed. Separating the features of these functions is again straight forward.

It is clear from Eq. (42), however, that absolute magnitudes of F and T can not be uniquely determined using only measurements of P . What is less obvious, is that broad trends can not be determined by making finite variations in St or He . For a simple example, assume a measured sound

spectra which is constant with frequency. Such a spectra could be generated by a source spectra that increases with frequency combined with a transfer function that decreases with frequency, or vice-versa. Thus, an important aspect of any algorithm designed to separate F from T must delineate which features of the acoustic transfer function can be determined unambiguously, and which features and trends can not be determined.

Previous attempts at separating the acoustic transfer function from the acoustic sources are described by Weidemann and Neise (1975) for centrifugal rotors. A study by Neise and Barsikow (1982) used a series of dimensionally similar centrifugal fans to study acoustic similarity laws and reported that the acoustic transfer function spectra were strongly dependent on the rotor flow coefficient ϕ , defined as the mean flow velocity in the duct normalized by rotor tip velocity. In terms of the Eq. (42), the term F should be dependent on the flow coefficient, but the acoustic transfer function T should not be. In the present derivation, changes in the radiation efficiency with flow coefficient are contained in the near-field term g_{near} , which is contained in F . The finding of Neise and Barsikow may have been a result of the underdetermined aspect of the formulation and their separation method. The results presented in the current work suggest that the acoustic transfer function T is not a function of rotor flow coefficient.

Mongeau et al. (1995) developed a method for characterizing the transfer function for a ducted centrifugal compressor. A similar technique was later applied to a confined jet flow by Zhang et al. (2002). Their method requires the assumption that on a plot of non-dimensional sound pressure spectra in terms of St , lines of constant He are parallel, with an offset determined by the derivative of the transfer function with respect to He . This assumption is valid so long as the acoustic source function $F(St)$ has only linear variations with St . For example, if one line of He overlaps a blade rate tone, and another He does not, the two lines would not be parallel. These algorithms were found to be effective at determining the small scale features of the spectral functions. However, application of the method presented by Zhang et al. (2002) to the current measurements led to large scale trends in the acoustic transfer function that were strongly dependent on the functional form of the acoustic sources.

The present technique was developed such that the small scale features of T could be determined unambiguously, and the large scale trends could be intentionally fixed by utilizing additional

information known about the acoustic system. The method assumes a function F_o exists, such that the source spectra at all rotor speeds is given by

$$\mathcal{F}(St, M_{tip}) = \mathcal{F}_0(St) M_{tip}^{n(St)}, \quad (43)$$

or

$$\log \mathcal{F}(St, M_{tip}) = \log \mathcal{F}_0(St) + n(St) \log M_{tip}. \quad (44)$$

In words, increasing tip speed will result in a linear increase in the logarithm of generated sound pressure at a fixed value of St . The purpose for leaving n as a function of St in Eq. (44) was two fold. First, n can be found as a function of St by a least squares fit to F and M_{tip} using Eq. (44). Thus leaving n as a function of St seemed to provide the least restrictive assumptions. Second, the tip speed scaling $P \sim V^n$ is given significant attention in the literature, and many different values for tonal and broadband sound have been documented; see, for example, Neise (1975). The methods developed by Mongeau et al. (1995) and Zhang et al. (2002) require a fixed value of n but provide results that are explicitly independent of the value of n chosen. A study by Quinlan and Krane (1996) reported on the spectral form of the tip speed exponent n , noting that the velocity exponent should be a function of St , but they approximated it as $n(f)$ by using a small change in rotor tip speeds ($\Omega_{max}/\Omega_{min} = 1.16$) such that the “smearing” of spectral features such as blade rate tones over St was minimized. No such approximation will be required of the current work. A detailed study of the resulting function $n(St)$ is beyond the scope of this paper, however. The main point of this paper is to describe a method for using Eqs. (41), (42) and (44) to find the function χ . The method works by assuming that P is not proportional to V^n only because $\log \chi$ is nonzero. That is, radiated sound at the fixed value of St should follow a V^n power law. Deviations from this are assumed to be a result of amplifications and attenuations at specific frequencies He , quantified as the function $\chi(He)$.

5.3.1 Ducted rotor experiment

A review of the rigid-walled ducted rotor and the specifics of the acoustic measurements is provided in this subsection. The experimental model was constructed in the anechoic chamber. A center cylinder extended upstream of the duct inlet and downstream of the outlet to create an

annular flow passage. The inlet flow was conditioned using a single layer of a “cheesecloth” type thin fabric with negligible acoustic impedance stretched over a cylindrical wire frame.

Radiated sound was measured using B&K 6.35 mm capacitance based microphones. The microphones were positioned approximately two meters from the duct inlet at an angle of 9.5 degrees from the duct axis. Measurements were acquired at 11 equally spaced speeds from 2500 to 5000 RPM. Example sound spectra are shown in Figs. 26 and 27. A number of distinctive features were observed in the spectra. For example, multiple “organ pipe” type resonances can be observed at fixed frequencies in Fig. 26. The spectra are plotted as functions of St in Fig. 27 and show distinct features at integer multiples of St , such as blade rate tones. Significant broad band sound was also observed at high frequencies.

The radiated sound was found to be dependent on the rotor flow coefficient ϕ . The duct flow rate was decreased by applying variable restriction in the form of thin fabric with negligible effect on the acoustic field to the duct exit, and increased by attaching the outlet of the duct to the anechoic wind tunnel blower.

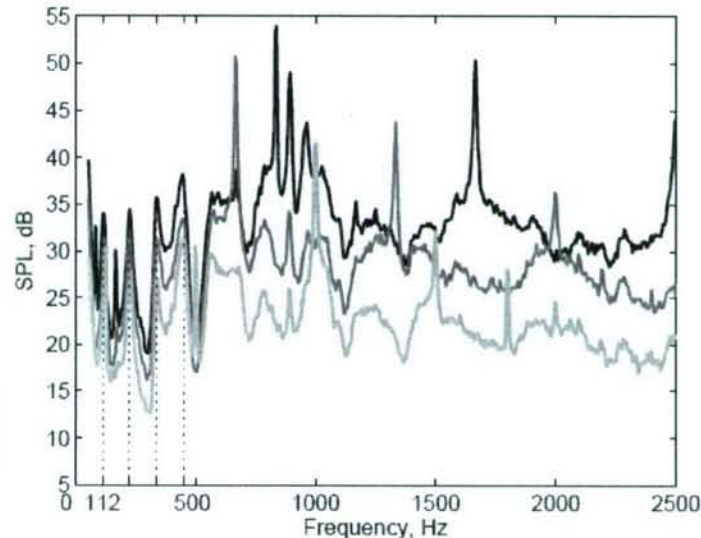


Figure 26 Measured sound spectra for ducted rotor at three rotational speeds.

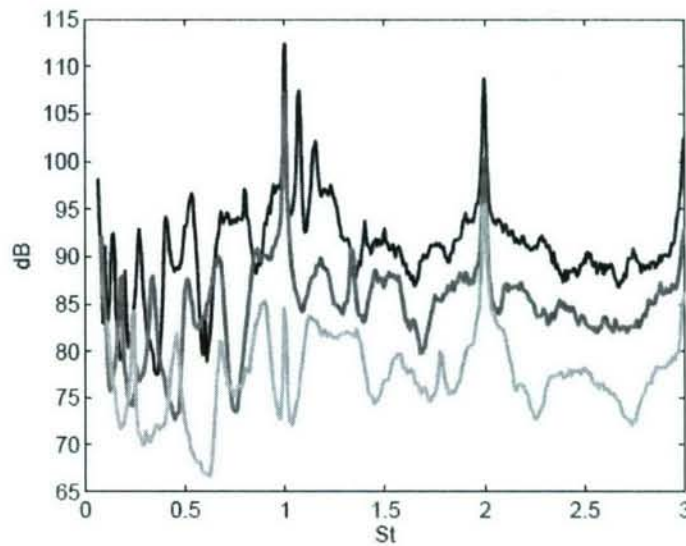


Figure 27 Measured sound spectra for ducted rotor at three rotational speeds, frequency normalized as St

5.4 Spectral decomposition algorithm

This section describes the details of the algorithm to extract an acoustic transfer function spectrum from a series of microphone measurements acquired at a range of rotor tip speeds. The linear model given in Eq. (42) can be expanded by substituting Eq. (44) for $\log F$ and Eq. (41) for $\log T$ to obtain

$$\begin{aligned} \log \mathcal{P}(f, M_{tip}) = & \log \mathcal{F}_0(St) + n(St) \log M_{tip} \\ & + \log k^2 + \log |g_{fs}|^2 + \log |\chi(He)|^2 + \log \cos^2 \theta. \end{aligned} \quad (45)$$

In this expression $\mathcal{F}_0(St)$, $n(St)$ and $\chi(He)$ are unknown. The algorithm seeks to find the function $\chi(He)$ that, in a least squares sense, best fits this expression given measurements of P at several values of M_{tip} . Once the function $\chi(He)$ has been found, the value of the true acoustic transfer function can then be reconstructed using Eq. (41). The relationship between the source function, the transfer function, and the radiated sound is given in Eq. (42).

5.4.1 Implementation as a computer algorithm

The method was implemented as an algorithm using Matlab on a desktop computer. Processing time ranged from less than a minute to several minutes, depending primarily on the number of points in the frequency spectra. A flowchart representation of the algorithm is included in Fig. 28 for reference. The algorithm is iterative, and the index j is used in this section to denote terms that are calculated with each iteration.

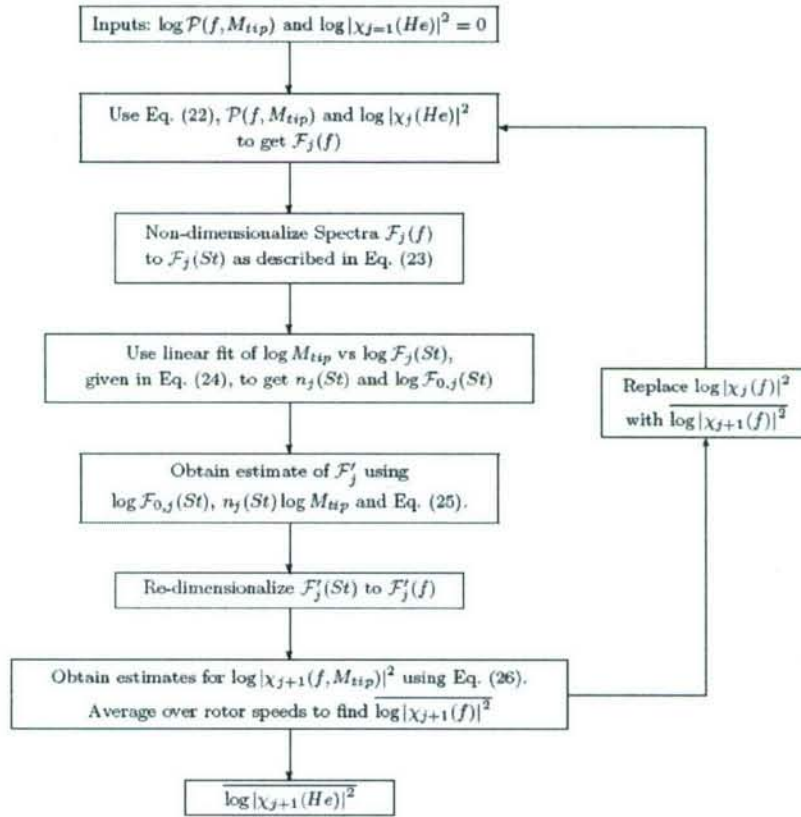


Figure 28 Flowchart representation of decomposition method. The number of the iteration is denoted by the index j .

Step 1: The source spectra for each rotor speed are estimated as

$$\begin{aligned} \log \mathcal{F}_j(f, M_{tip}) = & \log \mathcal{P}(f, M_{tip}) - \log k^2 \\ & - \log |g_{fs}|^2 - \log |\chi_j(He)|^2 - \log \cos^2 \theta. \end{aligned} \quad (46)$$

For the first iteration ($j = 1$) the function $\log |\chi_{j=1}(He)|^2$ is set equal to zero, and the rest of the terms on the right-hand side of Eq. (46) are known. The impact of this initial value for χ will be

discussed below. The spectra are made non-dimensional using the source length πD_r and velocity $V_{tip}B$ as,

$$\mathcal{F}_j(St, M_{tip}) \equiv (V_{tip}B/\pi D_r) \mathcal{F}_j(f, M_{tip}). \quad (47)$$

This type of spectral scaling is described by, e.g. Blake(1986) (p. 38). Linear interpolation was used to obtain the spectral magnitudes at discrete values of St from $\mathcal{F}_j(f, M_{tip})$. It was also important to restrict the calculations to the extent of the available data. Specifically, the highest frequency usable was determined by the highest St of the highest speed. As an example, the maximum measured sound frequency of 20 kHz corresponded to $St=48$ at 2500 RPM, and $St=24$ at 5000 RPM, so the highest St that could be used was 24. The limit of the estimates for $\mathcal{F}_j(St=24)$ likewise correspond to frequencies of 10 kHz to 20 kHz, so the lower value of 10 kHz must be used in re-dimensionalizing the functions back to frequency in Step 4 below. The lower limit of the usable range was determined by the usable frequency range of the anechoic facility. A minimum useful frequency of 100 Hz for the present measurements corresponded to $St=0.24$ for 2500 RPM and $St=0.12$ for 5000 RPM. The limiting usable value of $St=0.24$ was used, which corresponded to 100 Hz at 2500 RPM and 200 Hz at 5000 RPM. The frequency range of usable data is reduced at both ends by the scaling.

Step 2: A least-squares fit to the estimated sound source spectra is used to obtain $n_j(St)$ and $F_{o,j}(St)$, using the expression provided in Eq. 44, and denoted here with iteration index j as

$$\log \mathcal{F}_j(f, M_{tip}) = \log \mathcal{F}_{0,j}(St) + n_j(St) \log M_{tip} \quad (48)$$

According to this expression, at each value of St , a plot of $\log \mathcal{F}_j(St, M_{tip})$ vs $\log M_{tip}$ should be a straight line with slope $n_j(St)$. Deviations from the linear scaling are assumed to be a result of $\chi \neq \chi_j$. An example from the ducted rotor experiment is shown in Fig. 29 at $St=1.02$. In the current experiment, $P(St=1.02, M_{tip})$ spans a frequency range from 425 to 850 Hz when measurements were obtained at 11 equally spaced speeds between 2500 and 5000 RPM. The values of $n_j(St)$ were determined using an ordinary least-squares fit, as well as a robust linear fit method, as described by Huber (1981). The robust fit was implemented using the “robustfit()” command in

Matlab, which uses an iterative weighted adaptation of the least-squares method that reduces the influence of outliers on the linear fit. In a small number of cases, less than 1% for the present data set, the robust fit fails to converge, and an ordinary least-squares fit is used for these values of St .

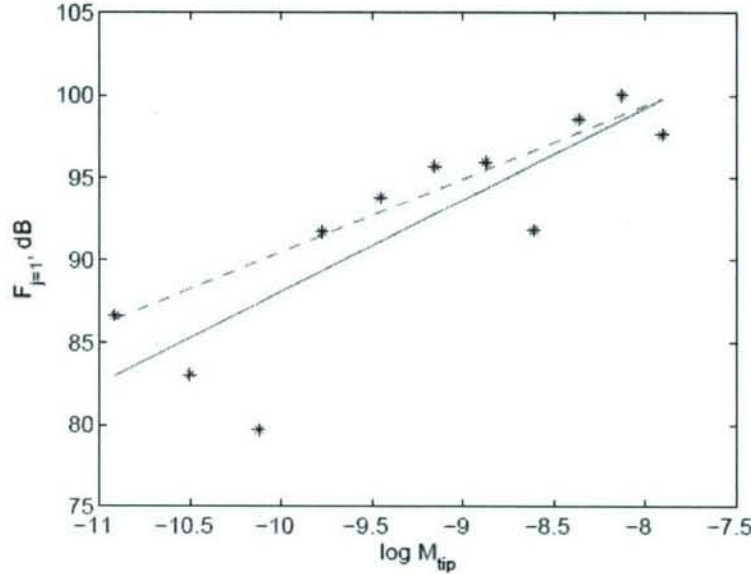


Figure 29 Experimental data showing linear fit to $\log F_{j=1}(St)$. “*”: estimated sound source $\log F_j(St=1.02)$; solid line: robust fit; dashed line: least-squares fit.

Step 3: An improved estimate for $|\log \mathcal{F}(St, M_{tip})|$, denoted $|\log \mathcal{F}'_j(St, M_{tip})|$ was obtained using Eq. (48), along with $n_j(St)$ and $\log F_{0,j}(St)$ from Step 2. This step can be expressed as,

$$|\log \mathcal{F}'_j(St, M_{tip})| = \log \mathcal{F}_{0,j}(St) + n_j(St) \log M_{tip}. \quad (49)$$

This new estimate of the source spectra is essentially a smoothed version based on the linear fit, and most of the transfer function effects should have been removed.

Step 4: An estimate for χ can now be found for each rotor speed using,

$$\begin{aligned} |\log |\chi_{j+1}(f, M_{tip})|^2| &= \log \mathcal{P}(f, M_{tip}) - \log \mathcal{F}'_j(f, M_{tip}) \\ &\quad - \log k^2 - \log |g_{fs}|^2 - \log \cos^2 \theta, \end{aligned} \quad (50)$$

as found in Eq. (45). The dimensionless source spectra $F'_j(St, M_{tip})$ were used to obtain $F'_j(f, M_{tip})$, and interpolation was again required to obtain data at the same points in f as the original measured sound spectra for use in Eq. (50). The transfer function effects can now be quantified as

$\overline{\log |\chi_{j+1}(He)|^2}$, where the overbar denotes average over rotor speeds M_{tip} .

Step 5: The function $\overline{\log |\chi_{j+1}(He)|^2}$ calculated in the previous step can be used in place of $\overline{\log |\chi_j(He)|^2}$ to iterate from Step 1.

Iterating between one and three times was found to provide a balance between a converged solution and a useful frequency range in the result. The example data from the ducted rotor in Fig. 29 are shown in Fig. 30 after one iteration. This indicates the transfer function features have been largely captured in $\chi(He)$, and the linear scaling is seen to be significantly improved.

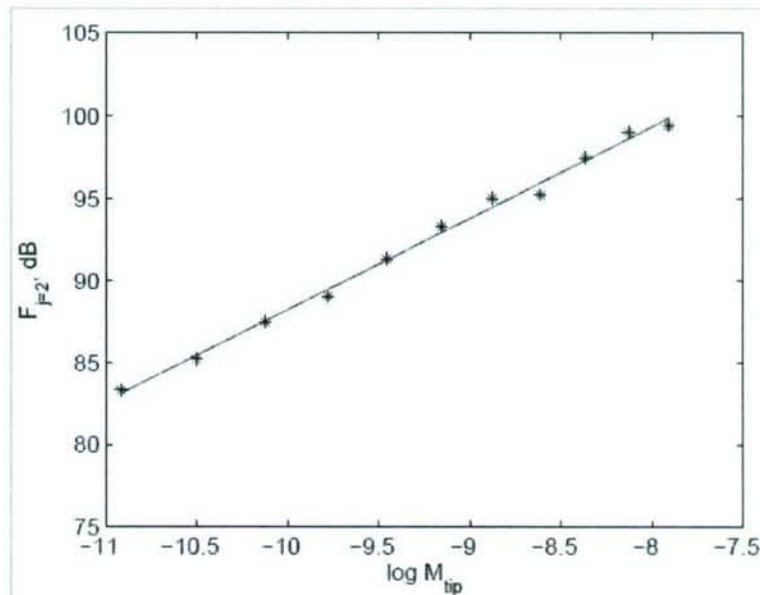


Figure 30 Experimental data showing sound source linear scaling after one iteration of the algorithm. Transfer function effects have been largely removed.

5.4.2 Error analysis of the algorithm

A set of defined input functions was constructed in order to evaluate the effectiveness of the algorithm. The set consisted of a function for $\chi(He)$, a function for $F_o(St)$ and a scaling $n(St)$. Spectral functions $P(f, M_{tip})$ were created using Eq. (45) and used as input into the algorithm. The resulting function for $\chi(He)$ could then be compared to the input, and an error computed by comparing the calculated transfer function ($\chi_C(He)$) to the actual transfer function ($\chi_A(He)$) as

$$Error = \sqrt{\frac{\int [\log |\chi_C(He)|^2 - \log |\chi_A(He)|^2]^2 dHe}{\int [\log |\chi_A(He)|^2]^2 dHe}}. \quad (51)$$

The transfer function $|\log |\chi_A(He)|^2|$ used for the defined input function set was a gaussian curve with a parameterized frequency width Δ_f and center frequency f_c given as,

$$\log |\chi_A(He)|^2 = e^{-10(f-f_c)^2/\Delta_f^2}. \quad (52)$$

This function is shown in Fig. 31. The feature shape can be considered a worst case, since the values were only positive and only induced outliers on one side of the correct linear slope in the $\log F(St, M_{tip})$ vs $\log M_{tip}$. A simple curve for the source spectra was used:

$$\log F_0 = 30 \cos(St/25) + 5 \cos(2\pi St - \pi) e^{-St}$$

Other functional forms of the acoustic source were used, and the results indicate that the function $\chi(He)$ did not depend on F_o . A scaling of $n = \text{const}$ was used for these results, although identical results were obtained when $n(St)$ was used. The experimental rotor tip speeds were used for M_{tip} .

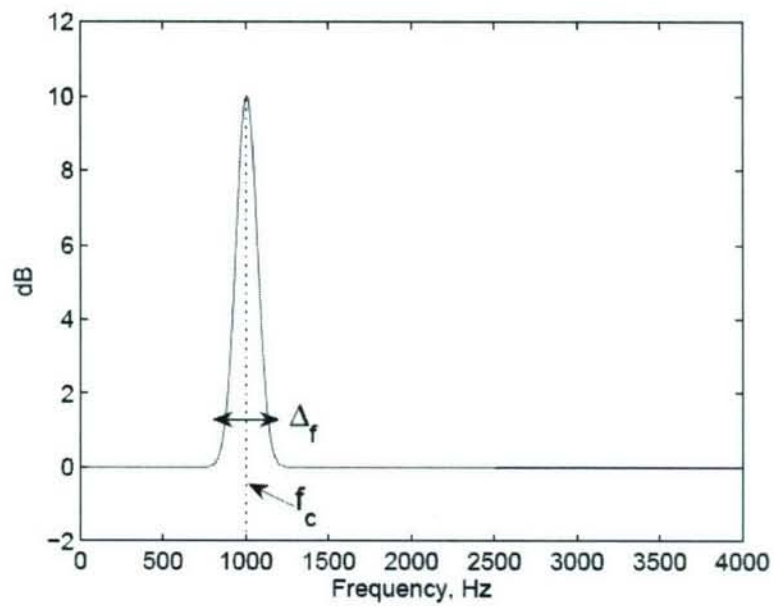


Figure 31 Example simulated transfer function

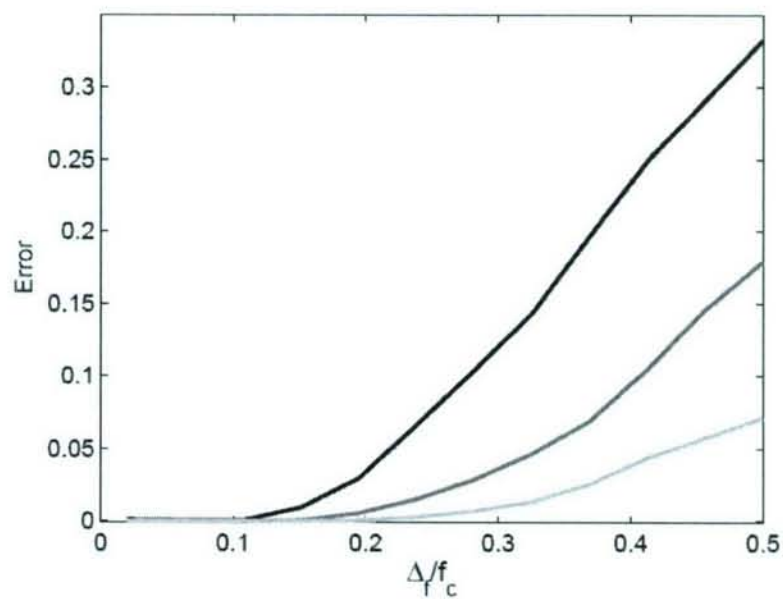


Figure 32 Error for different values of feature size ratio and speed ratio after three iterations. Dark line: SR=2, Med-gray: SR=3, Light gray: SR=5.

A series of transfer functions were tested over a range of f_c and Δ_f and the error was computed. It was found that the error could be described by the functional relationship

$$Error = function\left(\frac{\Delta_f}{f_c}, SR\right), \quad (53)$$

where SR is the ratio of the maximum rotor speed to the minimum rotor speed. Specifically, the error curves at each SR collapsed when plotted against the *feature size ratio*, Δ_f/f_c . This is explainable because the range of f spanned at fixed St is a linear function of St . In this experiment, at $St = 1$ the 11 speeds span 416 to 833 Hz while at $St = 10$ the range is between 4160 and 8330 Hz. Lower St values result in frequency ranges that are smaller, such that if the transfer function changes only slightly across the frequency range it can not be well resolved. The apparent size of a feature therefore depends on its center frequency “location,” f_c , as well as its frequency “width,” Δ_f . Note that this result is consistent with the previously mentioned limits on separating Eq. (42). Specifically, absolute magnitudes and linear trends in the transfer function can not be described by finite values of Δ_f/f_c and thus can not be determined.

The successful identification of transfer function features is also dependent on the speed ratio used during measurement. A small speed ratio results in points that are close together in f at constant St and only transfer function features that cause changes in that range of frequency can be identified. A larger speed ratio allows larger features to be identified. Minimum and maximum rotor speeds are limited by the experimental apparatus. Conversely, the limitation on using larger speed ratios is important when considering the scaling the spectra between St and He , as previously discussed. This restricts the number of iterations that can be performed, although adequate results can typically be obtained with only one or two iterations.

The error functions defined by Eq. (53) are shown in Fig. 32. As shown, for the set of defined input function tests using $SR = 2$ and a feature of size 0.1 an error of 0.004 was calculated after one iteration and 0.0008 after two iterations. A larger feature with size of 0.2 resulted in an error value of 0.05 after one iteration and 0.03 after three iterations. Small features are well resolved under all speed ratios while larger features are poorly resolved. A higher speed ratio leads to lower error, especially for larger feature size ratios.

5.5 Results using experimental data

An effective test of the algorithm utilized data acquired from the ducted rotor experiment using the same duct geometry with a variety of rotor sound sources. Manipulating the rotor flow rate provided a method for varying the sound produced by the rotor without introducing additional sound sources into the system. Ingested turbulence, for example, could also have been varied, but turbulence generators may be a significant source of sound. The rotor flow coefficient ϕ was varied between rotor stall and zero pressure rise. The spectra for $\Omega = 5000$ RPM are shown in Fig. 33 at four flow coefficients. Substantial changes in the sound produced by the system can be observed, indicating that the source spectra was a strong function of ϕ .

The function $|\chi(He)|$ was calculated as specified in the previous sections using microphone measurements acquired at the four flow coefficients. These results are shown in Fig. 34 using two iterations of the algorithm. The frequency axis was normalized by the first organ pipe frequency based on duct length L calculated as

$$f_0 = \frac{c}{2(L + 0.6133D)}, \quad (54)$$

using the end correction as calculated by Levine and Schwinger (1948). The harmonics of predicted organ pipe modes are seen to correlate with peaks in the resultant transfer function. It is also clear that the function $|\chi(He)|$ determined by the algorithm is essentially independent of the acoustic source. The standard deviation between the four curves at each frequency was calculated, and a mean value of 0.29 dB was found.

Significant deviations are noted at only two frequencies, $ff_o=1$ and $ff_o=8$. At the lower frequency, the deviant $|\chi(He)|$ values result from the lowest flow coefficient, $\phi = 0.17$. The rotor is stalled at this condition and the reduced magnitude was likely a result of changes in the coupling between the dipole source distribution and the duct plane waves. The deviant $|\chi(He)|$ values at $ff_o=8$ occurred at the highest flow coefficient, $f = 0.42$. At this condition the blades are completely unloaded and again, a change in the coupling between the blade dipoles and higher order duct modes could explain the variation in $|\chi(He)|$.

The final step in the analysis was to reconstruct the transfer function $T(He)$ from the determined $|\chi(He)|$ function using Eq. (41). The sound source function F could be found using T and the measured sound spectra P , as found in Eq. (42). An example of these three functions is shown in Fig.

35. As an independent validation of Eq. (41) and its assumptions, a reciprocal technique was used to obtain the dipole transfer function. Specifically, a miniature intensity probe was constructed, calibrated and placed in the duct at the axial position of the rotor with the blades removed. The dipole transfer function (∇_{0g}) was then determined using the method of Fahy (1995).

The transfer function determined using reciprocity is shown in Fig. 35 as a dotted line. The absolute magnitude and trend of the two curves support the present interpretation of Eq. (41) for $St < 2$, corresponding to around 1700 Hz. Note that the features determined from reciprocity are greater in magnitude by up to 15 dB compared to the rotor transfer function T at integer multiples of f_0 . This result is likely due to the absence of the blades during the reciprocity experiment. That is, the rotor would cause an effective impedance change in the duct which would reduce the organ pipe resonances. In addition, the true spatial distribution of the sources (axially and radially) that occurs in the rotor would lead to reduced resonant response.

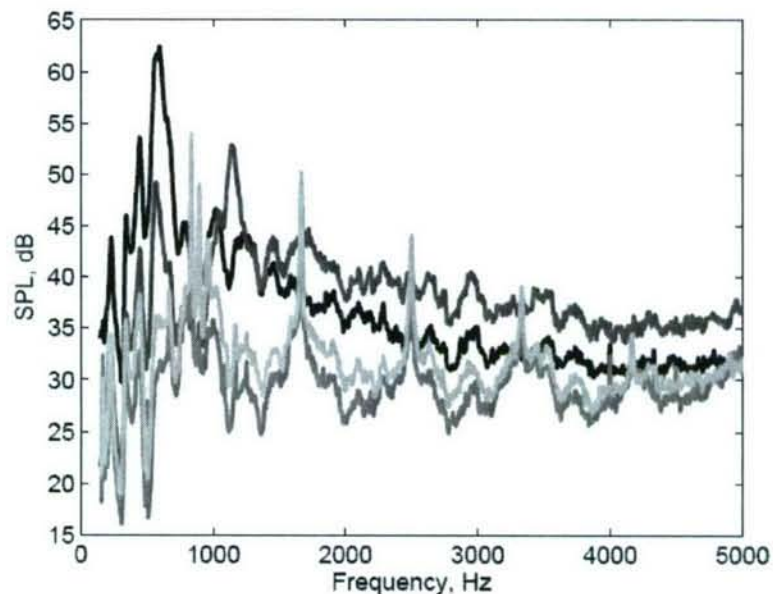


Figure 33 Measured sound under different flow coefficients at 5000 RPM.

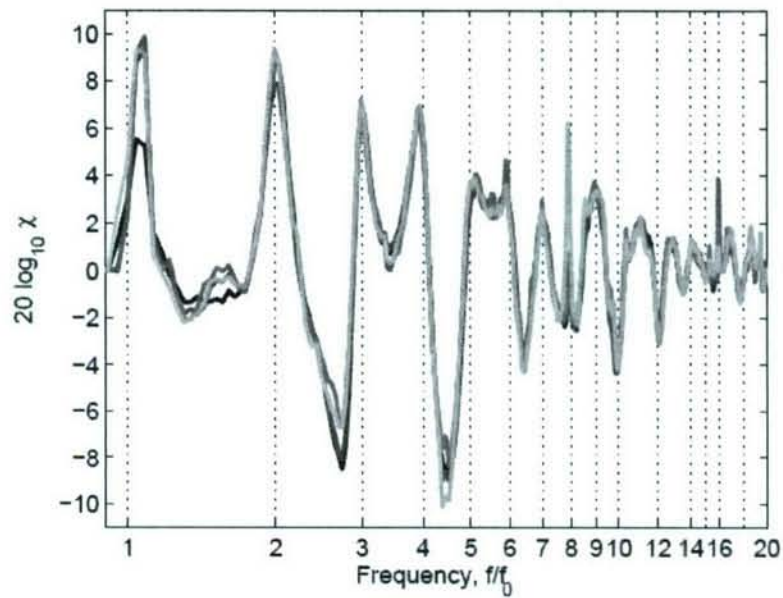


Figure 34 Calculated transfer functions at varied flow coefficients. Frequency is normalized by the first organ pipe mode frequency.

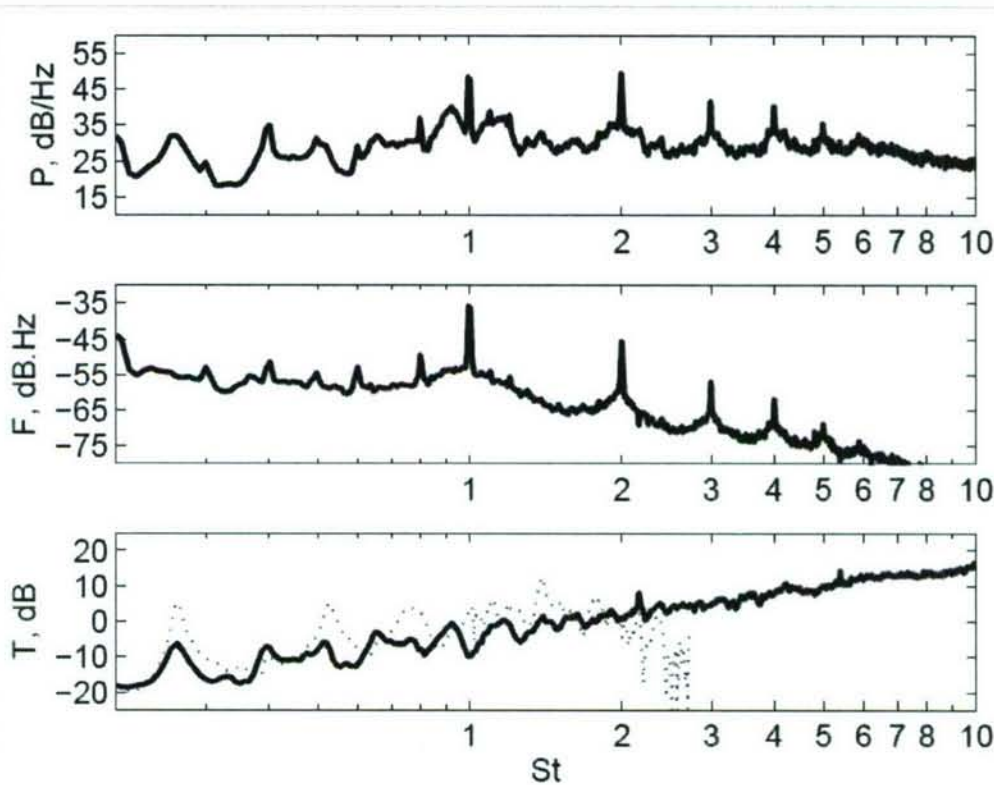


Figure 35 Example sound spectra and decomposition results from algorithm showing sound pressure, P , unsteady force, F , and transfer function, T .

5.6 Conclusions

A technique for processing aeroacoustic measurements was developed and evaluated. Using this algorithm the acoustic transfer function T could be determined. This will allow for the study of the sound source spectra F separate from acoustic transfer function effects. The method utilized the two frequency scales that are inherent in many applications to determine the functional form of a net equivalent source and a net acoustic transfer function from radiated sound spectra at various fan speeds. This was implemented as a computer algorithm, and evaluated with mathematically defined input functions, as well as experimental results from a low speed ducted rotor. The following conclusions have been drawn from this study:

- Any separation of net sources and net transfer function requires some form of assumption about either the source or the transfer function spectra. In the present algorithm, the acoustic source was assumed to increase with rotor speed to an unknown power. It was found that this assumption allowed for a unique determination of $\chi(He)$, which contained the narrow band spectral features of the acoustic transfer function T .
- The ability of the algorithm to determine spectral features of the net transfer function was quantified. Specifically, features whose width to center frequency ratio $\Delta f/f_c < 0.1$ were found to be correctly resolved with an error of less than 1% for a speed ratio of 2. This result was found to be independent of the spectral character of the acoustic source.
- The algorithm was applied to a ducted rotor model operating under a range of flow coefficients. Transfer functions were calculated for each of these source conditions and were found to closely agree, with a standard deviation of 0.29 dB. The method effectively determines transfer function features from measured sound in a system where a net dipole source term is an appropriate approximation.
- The spectral character of the ducted rotor transfer function was found to have peaks of magnitude up to 10 dB at integer multiples of the first duct organ pipe mode, in addition to other features.
- The magnitude and large scale trend of the transfer function can be determined when a distribution of axially oriented dipoles is an appropriate approximation for the sound source. The magnitude and large scale trends were verified using an independent reciprocity measurement of the transfer function.

6.0 Sound and Vibration Produced by an Airfoil Tip in a Turbulent Boundary Layer Flow with an Elastic Wall

6.1 Introduction

Predicting the acoustic radiation from a finite elastic wall section subjected to complex turbulent forcing is a complicated problem. This is particularly true when rigid surfaces are subjected to turbulent flow in proximity to the vibrating structure. This type of interaction occurs often in applications and results in a coupling of rigid body aerodynamics, aero-acoustics, and structural acoustics.

A flowchart describing the two boundary value problems considered in the present work is shown in Fig. 36. The first row, labeled 'A', describes the canonical problem of a membrane subjected to a stationary turbulent flow on one side. A formal solution for the structural motion can be found by convolving the unsteady wall pressure amplitudes (expressed in a wavenumber-frequency domain) with the structural Green's function¹. Given the structural motion, the radiated acoustic pressure can be found through a second convolution of the wall motion with the acoustic Green's function [1]. Although problem 'A' can be solved formally, a number of issues make practical predictions difficult. For

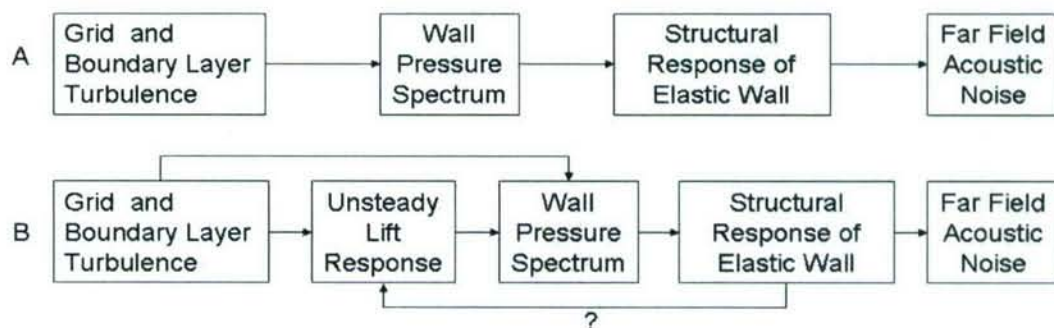


Figure 36: Flow chart showing describing each of the physical mechanisms involved in the present boundary value problem.

example, the unsteady wall pressure may result from external acoustic excitation or turbulence which is not stationary in either space or time, or both. Secondly, the structural Green's function may not be known analytically, and may be difficult to resolve numerically. This is particularly true when the wave motion of the structure includes mixed flexural and membrane waves, and when fluid loading effects are present [2-5]. Lastly, mean static pressure variations can lead to localized membrane stresses in the structure that modify its response.

The second row shown in Fig. 36 illustrates a more complex problem in which an airfoil tip is placed in proximity to the elastic wall. In this configuration the leading edge of the airfoil interacts with, and modifies, the approach turbulence, and results in a net unsteady force on the airfoil surface. This unsteady lift can result in radiated dipole type sound which can add to the unsteady pressure experienced by the elastic wall. In addition, the movement of the membrane can lead to changes in the pressure field experienced by the airfoil, leading to a fully coupled problem.

The present investigation considered the conditions with and without an airfoil in proximity to a round Aluminum membrane. The membrane was inserted into one side of a test section of an anechoic wind tunnel. A detailed description of the experimental program and data processing is provided in the following section. Results from each stage of the causal flowchart shown in Fig. 36 are provided for cases 'A' and 'B' in sections 6.3 through 6.6. Conclusions will then be presented and discussed in the context of the ongoing research.

6.2 Experimental Setup

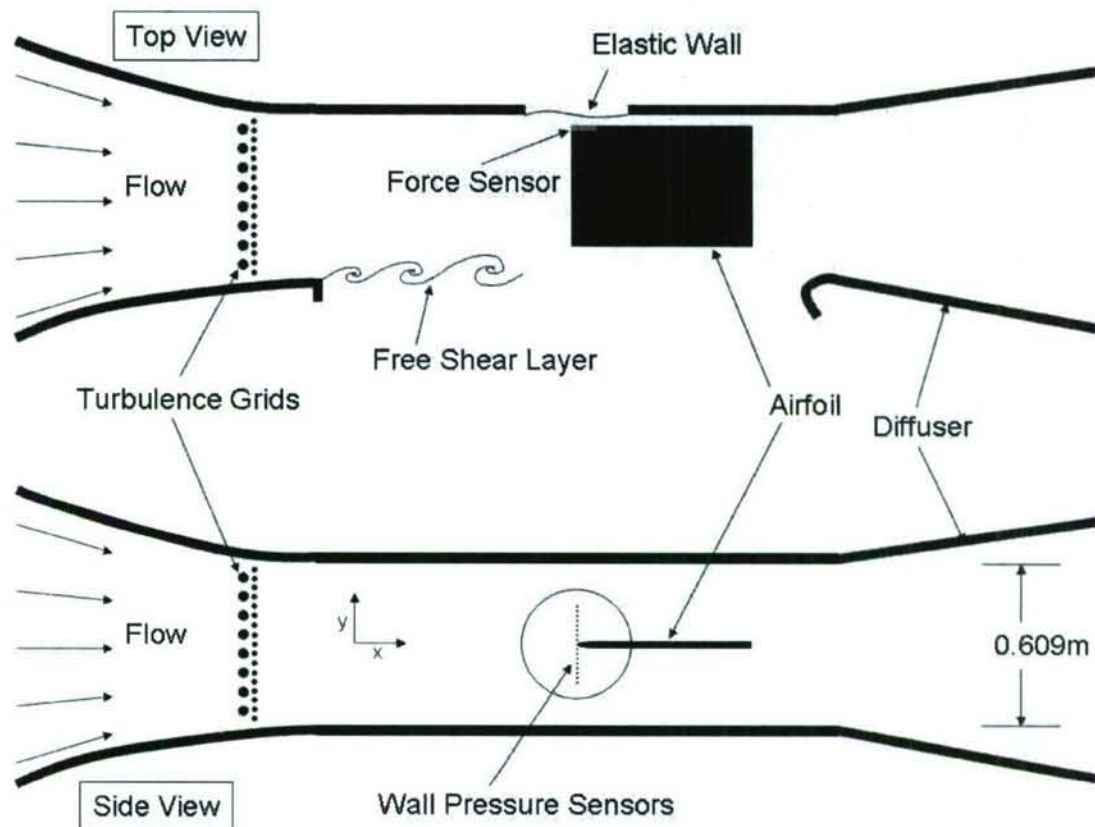


Figure 37: Schematic of experimental setup.

A schematic representation of the experiment is shown in Fig. 37. The open jet test section was enclosed on three sides allowing the airfoil to be cantilevered, with a tip gap of 6.35 mm, into the test section. Acoustic pressure generated on both sides of the membrane could radiate into the anechoic chamber. The flat plate airfoil had a span of 406 mm, chord of 610 mm and thickness of 6.35 mm. The large chord and span provided a force response with only leading edge effects as described in the next section. The leading edge was milled to a 5 to 1 ratio ellipse. Data were acquired for four flow speeds ranging from 17.5 to 25 m/s in increments of 2.5 m/s.

The elastic wall was a circular membrane of 0.127 mm thick Aluminum foil with a diameter of 0.4064 m. A uniform, isotropic tension of 219 N/m was applied to membrane. The tension was measured using four force transducers. The membrane was clamped on the entire circumference.

Two turbulence generating grids were combined in order to produce the unsteady approach flow field. The first grid was made from 12.7 mm diameter cylinders with 76.2 mm spacing while the second was made from 3.2 mm diameter cylinders with 25.4 mm spacing. The purpose of two grids was to augment the natural elastic wall boundary layer and generate a large range of scales of turbulent fluid motions. Hot wire anemometry was used to determine the velocity spectrum of the approach flow.

The unsteady lift response of the airfoil to the turbulent approach flow was measured directly using novel "strip" surface pressure transducers embedded in the tip of the airfoil as shown in Fig. 37. A sensor was placed on either side of the airfoil tip near the leading edge. The shape of the sensors provide a response that is directly proportional to the net unsteady lift experienced by the leading edge region of the foil. Data were acquired at a sampling frequency of 40 kHz for 209 s. A detailed description of the measurement technique may be found in Slaboch and Morris.[6]

The wall pressure spectrum of the turbulent flow field was measured using an array of 16 microphones with a diameter of 0.7 mm embedded in a rigid wall as shown in Fig. 37. The microphones were flush mounted to the surface and spaced 1.9 cm apart in the transverse direction with 8 on each side of the airfoil.

The elastic wall vibrational response was measured using a scanning laser Doppler vibrometry system (SLDV) and a separate, single point LDV. The SLDV was used to

survey 145 points on the membrane, while the single point LDV was focused only at the center point of the membrane. A full scan of the membrane was acquired for each of four flow speeds both with and without the airfoil present. Data were acquired at 40.96 kHz for 12.8 s per scan point.

The far field acoustic noise generated by the system was recorded using a 6.35 mm ACO microphone. The microphone was placed 2 m from the membrane.

6.3 Unsteady Lift Response

The airfoil configuration described in Section 6.2 was chosen specifically to isolate the leading edge response. That is, the trailing edge was sufficiently far downstream as to not affect the membrane motion. The leading edge response to unsteady fluid motions is described by Amiet [7]. The unsteady lift can be represented in non-dimensional form by:

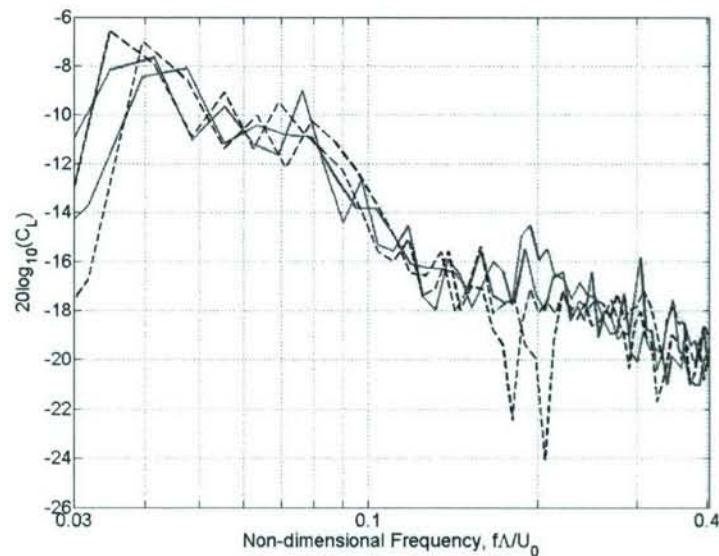


Figure 38: Unsteady lift response of the airfoil subject to turbulent flow. The blue, solid lines represent the case with an elastic wall while the black, dashed lines are the rigid wall case.

$$C_{L'} = \frac{G_{L'}}{\rho_0 U_0 \tilde{v} L} \quad (53)$$

where ρ_0 is the free stream density, U_0 is the free stream velocity, L is the length of the sensor, \tilde{v} is the square root of the autospectral density magnitude of the "upwash" component of the turbulent velocity, and $G_{L'}$ is the square root of the autospectral density of the unsteady lift. The frequency scale was non-dimensionalized by U_0 and the integral length scale of the turbulence, Λ , defined as [8]

$$\Lambda = \int_0^{\infty} R_{xx}(\tau) d\tau \quad (54)$$

where $R_{xx}(\tau)$ is the autocorrelation function. At the measurement location near the tip, $\Lambda = 7.1$ mm. The integral length scale at the center of the test section was found to be 1.2 cm. The lift coefficient for the unsteady lift response is shown in Fig. 38 for both the highest and lowest flow speeds, both with a rigid and an elastic wall. The data show that the elastic wall did not have an effect on the unsteady lift response of the airfoil. The only exception was at a non-dimensional frequency of approximately 0.2, where the unsteady lift with a rigid wall showed a negative peak in the spectral density. However, the local minimum was at a constant dimensional frequency and therefore did not change with speed which suggests that this result was not a physical response but merely an artifact of the signal processing, likely due to a calibration error. Aside from that one notable frequency, the data in Fig. 38 agree remarkably well. Thus the unsteady lift can be considered to be independent of both Reynolds number and the wall condition used.

6.4 Wall Pressure Spectrum

The wall pressure spectrum was measured using 16 surface mounted microphones

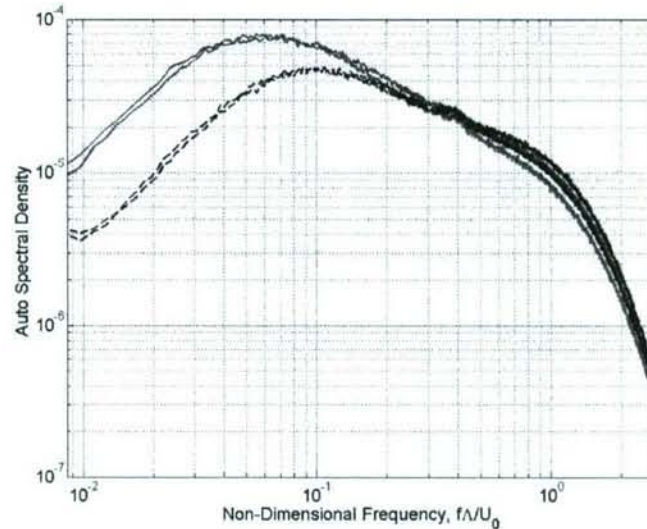


Figure 39: Autospectral density of the two microphones located nearest to the centerline of the tunnel. The blue, solid curves represent the case with the airfoil present while the black, dashed lines are the case with no airfoil present.

in a vertical array, embedded in a rigid wall. The microphones were placed 1.9 cm apart

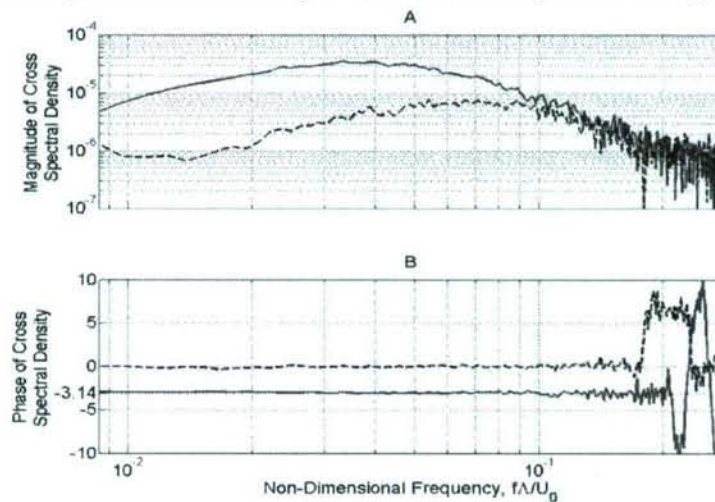


Figure 40: A.) Magnitude and B.) phase of the cross spectral density between the two microphones located closest to the centerline of the test section. The solid, blue lines represent the case in which the airfoil is present while black, dashed lines are without the airfoil.

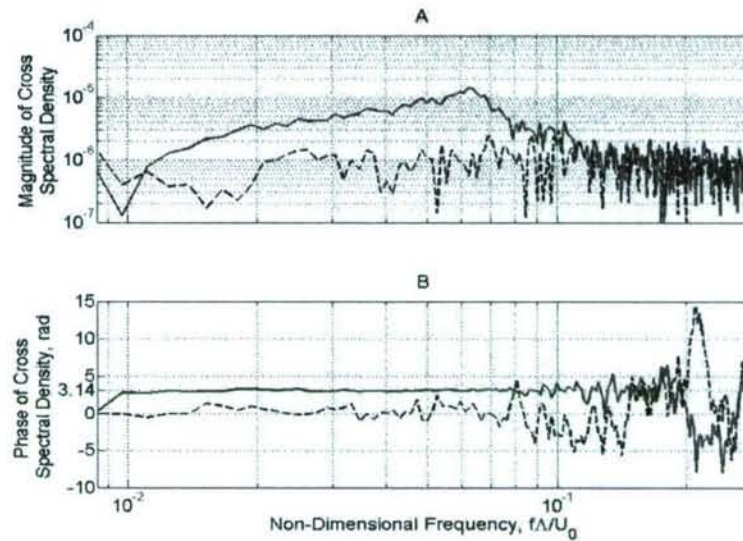


Figure 41: A.) Magnitude and B.) phase of the cross spectral density between the two microphones located furthest from the centerline of the test section. The solid, blue lines represent the case in which the airfoil is present while black, dashed lines are without the airfoil.

with 8 microphones on each side of the centerline of the test section as shown in Fig. 37. Figure 40 shows the autospectral density of the wall pressure, normalized by the dynamic pressure ($\rho_0 U_0^2/2$). Four spectra are shown in Fig. 40 which represent the two microphones closest to the centerline. Measurements with and without the airfoil present are shown. The results indicate that the presence of the airfoil had a small, if not negligible effect on the wall pressure spectra for frequencies $f\Lambda/U_0 > 0.2$. At lower frequencies the airfoil caused a substantial increase in the unsteady pressure. It is interesting to note that both configurations indicate an f^2 relationship at low frequencies.

Further insight into the effect of the airfoil on the wall pressure can be obtained from the cross spectral density of two microphone signals. Figure 39 shows the magnitude and phase of the cross spectral density between the same microphones used to compute

the auto spectra in Fig. 40, that is, 0.95 cm on either side of the airfoil leading edge. The magnitude of the cross spectrum was increased by as much as a factor of 10 at lower frequencies, with negligible increase at higher frequencies. The phase relationship, shown in Fig. 39b indicates that for low frequencies the two signals were in phase when the airfoil was not present, and π out of phase when the airfoil was present. The phase matching without the airfoil is intuitive given that the microphones were placed 2.67Λ apart. That is, it would be expected that the turbulent motions that contribute to the spectra at $f\Lambda/U_0 \ll 1$ have a length scale that is significantly greater than the microphone spacing, and thus the two locations are subjected to essentially the same low frequency unsteadiness. The switch in phase to $-\pi$ when the airfoil is present further suggests that the pressure field is dominated by the turbulence~leading edge interaction. Specifically, both the near field hydrodynamic pressure and the radiated sound pressure will be dipole-like due to the net reaction force exerted by the airfoil onto the fluid.

Figure 41 shows the cross spectral density magnitude and phase for the two microphones located at ± 14.3 cm. These were the furthest away from the centerline of the test section. These show the same general behaviors as those seen in Fig. 39, however, there are two distinct differences. First, the magnitude of the correlation between these two locations is a factor of 5 lower than that for the two microphones closest to the centerline. This is to be expected because the spacing of these two microphones is much greater than the integral turbulent length scale. Second, since the hydrodynamic field at these locations was not likely altered, the increase in the wall cross spectral density with the airfoil present can be attributed to acoustic radiation from the tip of the airfoil. The phase difference of π indicates that the acoustic radiation from the airfoil is dipole like sound.

6.5 Elastic Wall Vibration Response

The elastic wall used was made from 0.127 mm thick Aluminum that was tensioned isotropically at 219N/m. The motion of the elastic wall can be approximated as a solution to the equation for waves in a membrane [1],

$$(\nabla_2^2 + k^2 \alpha^2) \eta = -P(r, \phi, \omega) \quad (55)$$

where η is the displacement of the membrane, P is the fluctuating net pressure difference, $k = \omega/c$, c is the speed of sound, and $\alpha = c/\sqrt{T/\sigma}$, where σ is the density per unit area, and T is the tension per unit length. The effects of flexural wave motion, aerodynamic and acoustic damping, and fluid loading have been ignored. For the case of a round membrane with a clamped boarder, the solution can be given in terms of the eigenfunctions for the free vibration of the membrane:

$$\frac{\cos}{\sin} (m\phi) J_m(2\pi v_n r/c_p) = 0 \quad (56)$$

where J_m is the Bessel function of order m , r is the radius of the membrane, c_p is the wave speed of the membrane and v_n is the frequency of the wave. The zeros of the Bessel function can be found to provide the natural frequencies of oscillation allowed in the membrane. For the experimental conditions given here, the natural frequencies are shown in Table 1. The structural response of the membrane at two locations, both with and without the airfoil, is shown as an auto spectral density of the membrane velocity in Figs. 42A and

42B. The physical locations chosen for these figures were somewhat arbitrary, but the data are indicative of observations at other locations as well.

Table 1: Natural frequencies of vibration for a clamped, circular membrane,

n/m	0	1	2	3	4	5
0	0.014	0.022	0.029	0.036	0.043	0.049
1	0.031	0.039	0.047	0.055	0.062	0.069
2	0.049	0.057	0.065	0.073	0.081	0.088
3	0.066	0.075	0.083	0.091	0.099	0.107
4	0.084	0.093	0.101	0.109	0.117	0.125

The addition of the airfoil was observed to create a substantial increase in the vibration amplitudes shown in Fig. 42A. The frequency range and amplitude of the increase were generally consistent with the increased auto and cross spectral measurements of the wall pressure shown in Figs. 39 and 41. Specifically, the rough increase in the wall pressure by a factor of 10 in the range $0.01 < f\Lambda/U_0 < 0.15$ can be observed in Fig. 42A as well. However, it is clear that the increased phase organization of the wall pressure

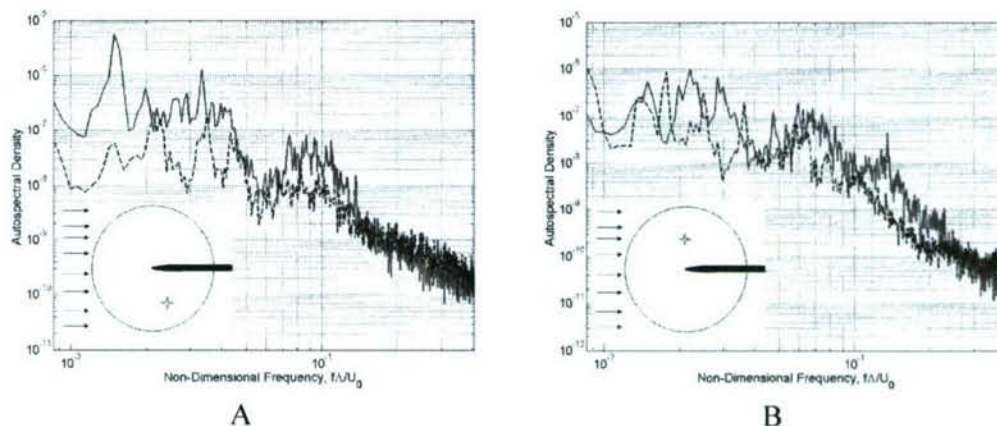


Figure 42: Autospectral density of the vibrational response of the membrane at A.) a radius of 14.7 cm and an angle of -105 deg and B.) a radius of 12.19 cm and an angle of 90 deg. The solid, blue curve is with the airfoil present while the black, dashed curve is in the absence of the airfoil. + indicates position on membrane.

due to the airfoil was causing some of the modes to be excited at significantly higher levels. For example, the fundamental membrane mode ($m=n=0$) was increased by a factor of nearly 100. At higher frequencies ($f\Lambda/U_0 > 0.1$) the vibration response was nearly identical for the two test cases.

The data shown in Fig. 8 were acquired under the same conditions as those in Fig. 42A, but show a number of notable differences. First, the broad increase in amplitudes at lower frequencies observed in Figure 42A is not present in Fig. 42B. In addition, modes that were not excited with the homogeneous turbulent forcing, for example $[0,1]$ and $[0,2]$, were found to be excited by the presence of the airfoil. At higher frequency the vibration amplitude was found to be increased by a factor of 5-10 in the range $0.07 < f\Lambda/U_0 < 0.25$. Given that the magnitude of the wall pressure fluctuations were found to be unaffected by the airfoil at these frequencies, it is reasonable to expect that the relative phase of the wall pressure led to this increase.

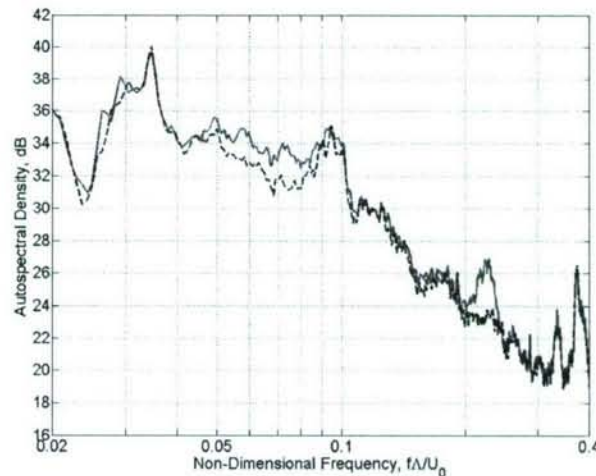


Figure 43: Autospectral density of a single far field microphone plotted on a Decibel scale with a bin width of 6.9×10^{-4} vs non-dimensional frequency. The solid, blue line is the case with the airfoil while the black, dashed line is without the airfoil present.

6.6 Acoustic Noise Response

The acoustic response of the elastic wall to complex turbulent forcing can be represented as the convolution of the membrane motion with the structural Green's function.[1] The near field is dominated by evanescent waves which cancel in the far field. The modes that do not cancel are scattered off of the boundaries of the membrane or other surface discontinuities. These non-cancelling modes will radiate to the far field as acoustic waves.

Data were taken with a single far field (2 m) microphone both with and without the airfoil present. Figure 43 shows the far field acoustic spectra for both cases. Over a range of $0.04 < f\Lambda/U_0 < 0.1$, the airfoil increased the far field acoustic noise by approximately 2 dB. An increase of this nature is to be expected given the response of both the wall pressure spectra and elastic wall vibration response to the presence of the airfoil. However, the range of frequencies over which there is a substantial increase is smaller than that observed for the wall pressure and elastic wall vibration spectra. There was also a large increase of approximately 3 dB at a frequency of 0.22, which is very close the natural shedding frequency of the turbulence grids.

6.7 Conclusions

The sound and vibration of an elastic wall produced by an airfoil tip, in a turbulent flow, near the wall was investigated. An experiment was conducted using two sets of boundary conditions, the first being a canonical setup in which the membrane is excited by turbulent flow alone and the second adding a flat plate airfoil to the flow with a narrow tip gap to the elastic wall. The unsteady lift response of the airfoil was measured using unsteady force transducers. It was determined that the elastic wall had a negligible effect

on the unsteady lift response when compared to that with a rigid wall in place. The presence of the airfoil had a significant effect on the wall pressure spectrum over a range of $0.01 < f\Lambda/U_0 < 0.15$. The effect was also observed in the vibrational response of the elastic wall. The increased structural vibration of the membrane corresponded to a 1-2 dB increase in the far field radiated acoustics. This was a significant increase in the far field sound generated by an elastic wall alone.

7.0 RECIPROCITY RESULTS FOR RIGID AND ELASTIC DUCTS

The study of sound radiated from aeroacoustic and structural acoustic systems requires an understanding of both the acoustic sources as well as the transfer of acoustic energy from the source location to a point of interest (e.g., the far field). The experimental use of reciprocity principles to measure the acoustic Green's function was described in Section 4. This section presents results from the reciprocal measurement of the acoustic Green's function and its gradient for two geometries of interest. The first was a rigid PVC cylindrical duct with 8.1 inch inner diameter and 24 inch length. The second was constructed from three sections of the thin nickel shell described in Section 3. The end conditions for both the rigid and elastic ducts were partially flanged as shown in Figure 44. The internal coordinate system shown describes the (r, θ, z) location of the virtual acoustic source in the duct. The far field, or "receiver" location is shown in Figure 45.

The purpose of the measurements was to investigate the dependence of the far field sound on the source and far field locations, and to compare these results for the rigid and elastic ducts. A related objective was to determine if the sensitivity of the far field sound to the source location is different for the elastic duct as compared to the rigid boundary conditions with nominally the same geometry. This issue is important for the definition of blocked, or net equivalent acoustic sources. Specifically, if a distribution of sources (such as a ducted rotor) is modeled as a single point source in a rigid-walled system, significant errors may be encountered when the actual sources are placed in an system where the elastic walls may change the spatial sensitivity of the local Green's function.

Measurements were conducted as described in Section 4 to obtain the Green's function, G , as well as its gradient, G_D . These functions represent the acoustic transfer functions for monopole and dipole sources, respectively. For ease of presentation, the results presented in the following subsections will be given as the difference between the measured value and the magnitude that would be obtained in a free space environment. Specifically,

$$G'(x_o, x_s) \equiv 10 \log[G(x_o, x_s)] - 10 \log[G_{FS}(|r|)] \quad (57)$$

where $G_{FS}(|r|)$ is the free space Green's function evaluated at the radial location $|r| = |x_o - x_s|$.

Similarly, the gradient function difference is defined as

$$G'_D(x_o, x_s) \equiv 10 \log([G_D(x_o, x_s)]) - 10 \log[G_{D-FS}(|r|)] \quad (58)$$

where G_D is defined in equation 7, and the free space value, G_{D-FS} is defined in equation 23.

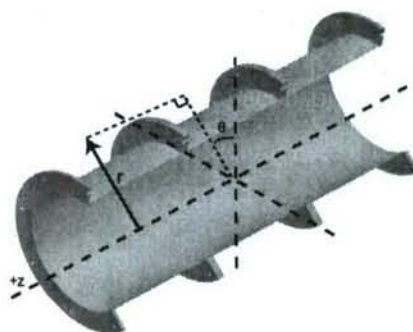


Figure 44 Schematic of geometry and source location coordinate system

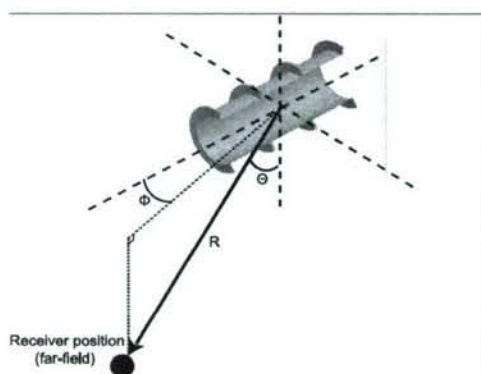


Figure 45 Far-field "receiver" coordinate system

7.1 Far field angular dependence of Green's function

This section presents results that describe the angular dependence of the G and G_D . The source location, x_s , was placed at the origin of the coordinate system shown in Figure 44. The far field location was measured 2m from the duct center, with the angular coordinate, ϕ , treated as the independent variable of interest.

Contours of G' and G'_D are shown in Figures 46 through 49 for both the rigid and elastic ducts. In these "polar" plots the radial direction represents the frequency, and the angular position represents the far field angle, ϕ . For example, the values shown near the horizontal axis of the polar plot represents the values "on axis" with the duct. The vertical direction represents a far field location that is perpendicular to the duct axis. The frequency values are shown in both axes scaled by the fundamental organ pipe frequency (eqn 24) on the horizontal axis, and normalized by the duct radius (a) on the vertical axis. Also, the frequencies of higher order mode cut-on are noted by the

ordered pairs in the figure where the first integer represents the radial mode order, and the second represents the circumferential mode order. For the G'_D measurements, the dipole axis was aligned with the duct axis.

The contours of G' shown in Figure 46 illustrates a number of distinctive features in the radiated sound field. First, the first organ pipe mode is observed to resonate which leads to a 10dB increase in far-field sound at all angles with respect to the duct. The second pipe mode is not excited since the axial center is an anti-node for this frequency. The third pipe mode is again excited, although two distinctive peaks can be observed in the azimuthal direction. The first is on axis, and the second is approximately 60 degrees from axis. The radiation at higher frequency is observed to be primarily on axis, with some increased levels between 20 and 60 degrees. The cut-on resonances are notable, and show several local maxima in the azimuthal direction.

The angular dependence of G'_D for the rigid duct is shown in Figure 47. These data show similar trends compared to the Green's function described above. A notable difference is the excitation of the even, rather than the odd ordered pipe modes. This is expected since the anti-nodes of the gradient function will be located at the nodes of the original function. It is also noted that the cut-on frequencies are not amplified (compared to the free space values).

Contour plots of G' and G'_D for the elastic duct are shown in Figures 48 and 49 respectively. It is first noted that the general character of the sound radiation with the elastic duct is similar to the rigid case. Specifically, local maxima in the rigid duct functions generally correspond to local maxima for the elastic duct. However, it is observed that generally increased radiation levels are present with the elastic duct sections. This is particularly evident at higher frequencies where the higher-order duct acoustic modes are interacting with the vibrating duct.

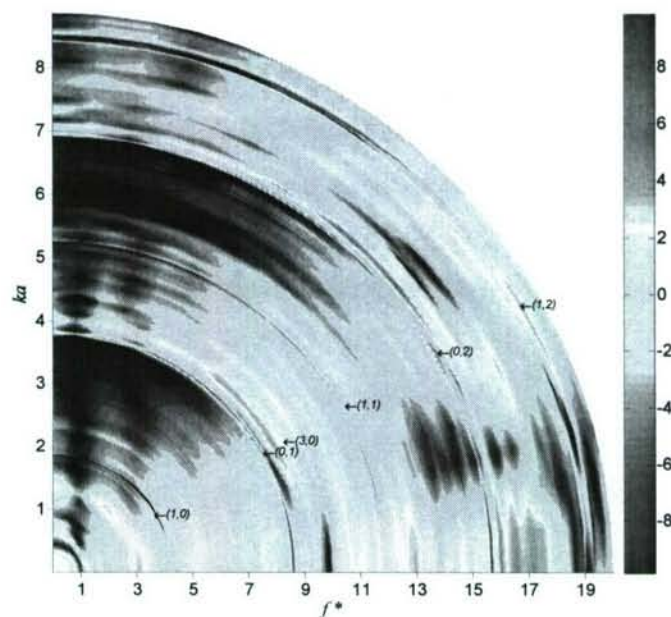


Figure 46 Contours of G' showing the angular and frequency dependence for the rigid duct.

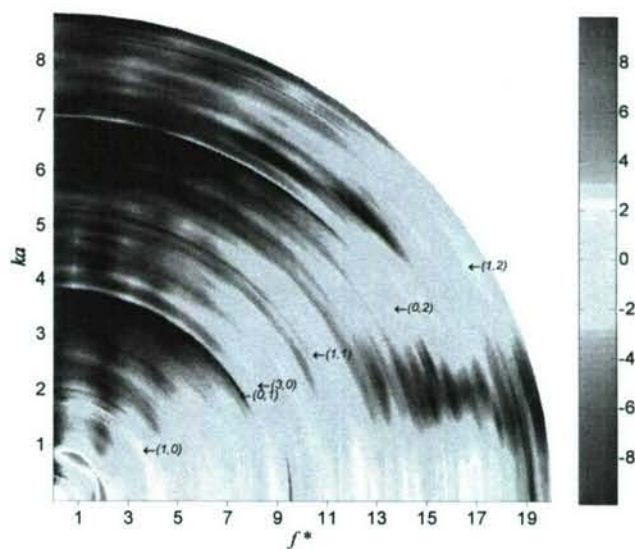


Figure 47 Contours of G'_D showing the angular and frequency dependence for the rigid duct.

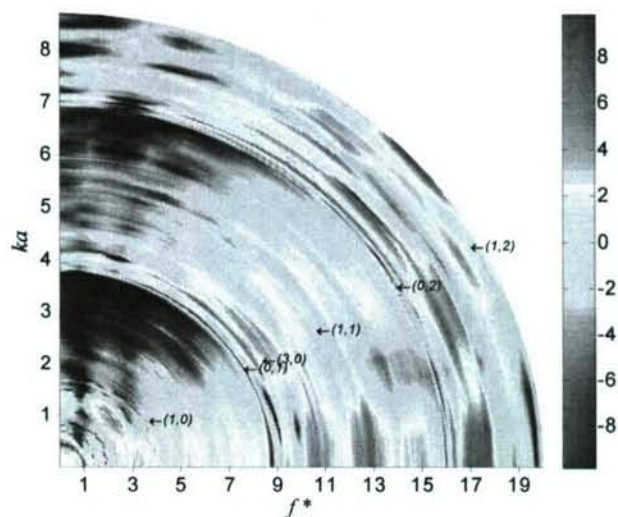


Figure 48 Contours of G' showing the angular and frequency dependence for the elastic duct.

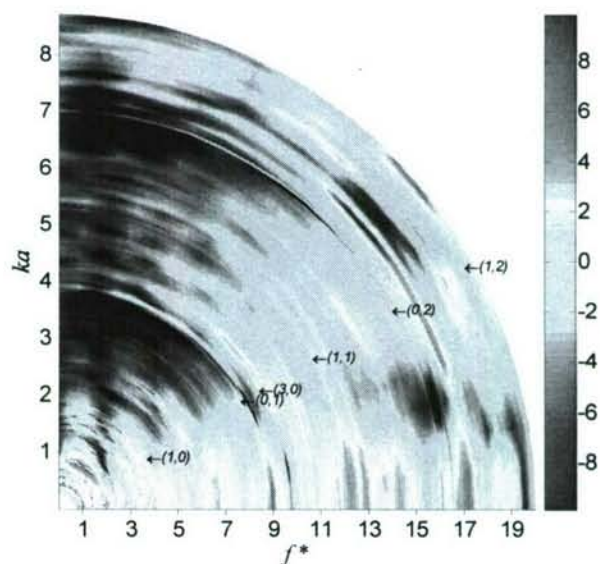


Figure 49 Contours of G'_D showing the angular and frequency dependence for the rigid duct.

7.2 Effect of Axial Location of Source on Radiated Sound

The effects of the axial location of the sound source are presented in Figures 50 through 53. The contour plots are shown with the frequency on the abscissa, again normalized by both the first organ pipe frequency as well as the duct radius on the lower and upper axes, respectively. The ordinate of the plots shows the axial location normalized by the duct length ($-0.5 < x/L < 0.5$).

The magnitude of G' for the rigid case shown in Figure 50 indicates a number of distinctive and interesting features to the radiated sound field. First, the nodal pattern of the first organ pipe mode can be observed by the strong amplification at the duct center compared to the duct ends at $f^*=1$. Similarly, at $f^*=2$ the amplifications are observed at axial locations of -0.25 and 0.25 corresponding to the nodes of the standing wave. Note that the dependence on z/L is not symmetric about the duct center since the far field location is placed on axis on the $z > 0$ side of the duct. The magnitude of G'_D shown in Figure 51 for the rigid duct shows similar results, although the organ pipe modes are excited at the anti-nodes of the standing wave as expected.

The radiated sound exhibits dramatic changes in character near both the $(0,1)$ and $(0,2)$ cut on frequencies. It is clear that the magnitudes of G' and G'_D at high frequency is both considerably larger than the free space Green's function, and is also highly dependent on the location of the source. For example, at $f^*=13$, G' varies by nearly 20dB from $z/L=0.5$ to 0.3 .

The results for the elastic duct generally exhibit increased magnitudes at all frequencies and axial locations. It is also noted that there are fewer locations at which the Green's function and its gradient have a lower magnitude than the free space values. Note that the structural free vibration frequencies of the shell are all about 200Hz, which corresponds to $f^*=0.7$. Issues related to the structural vibration will be described in the next section.

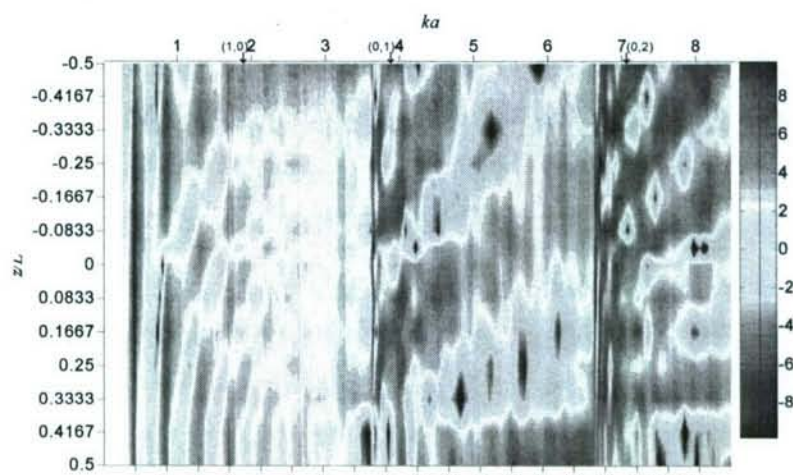


Figure 50 Axial dependence of G' for rigid duct

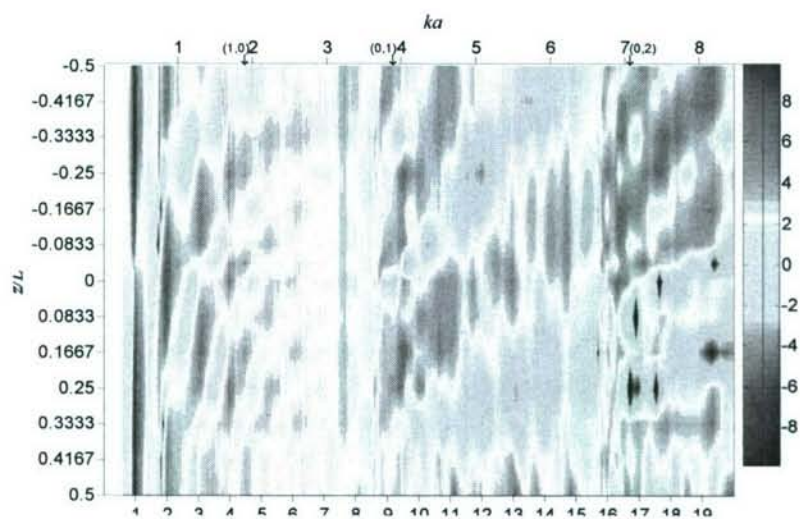


Figure 51 Axial dependence of G_D' for rigid duct

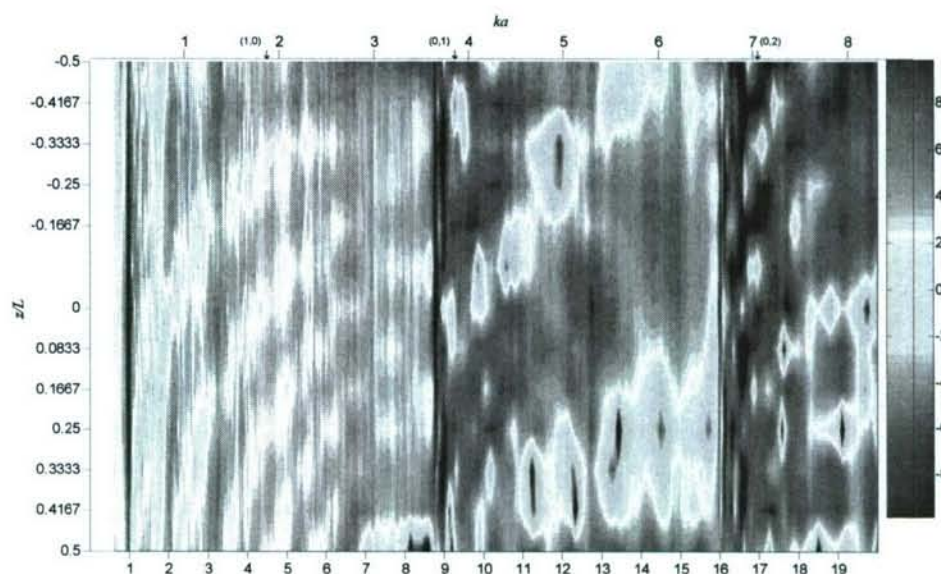


Figure 52 Axial dependence of G' for elastic duct

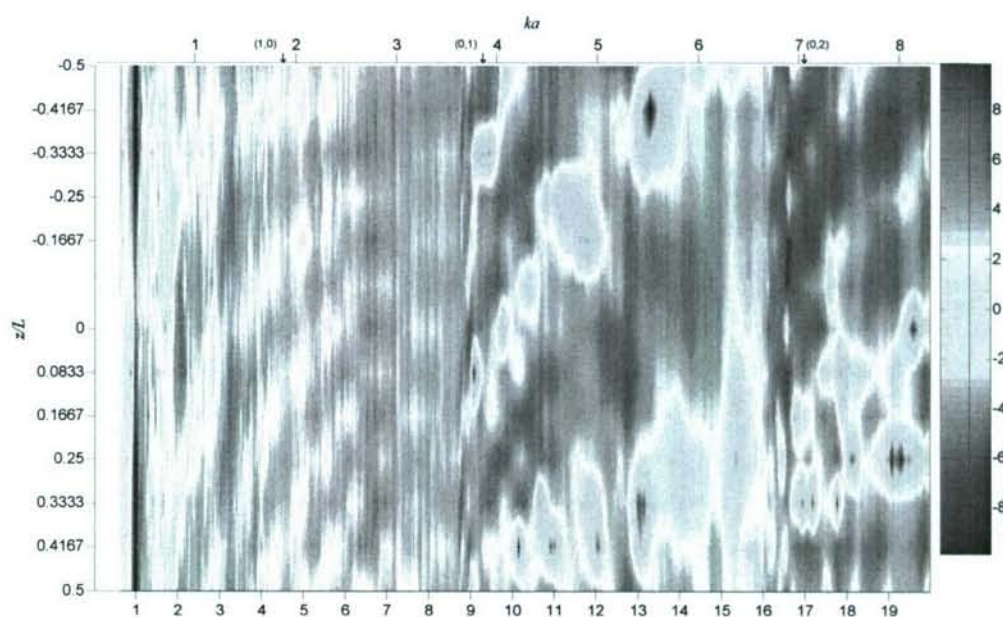


Figure 53 Axial dependence of G_D' for elastic duct

7.3 Effect of Radial Location of Source - On and Off Axis

The radial position of an axial source is an important parameter in predicting the radiated sound from a ducted rotor system. Specifically, a ducted rotor will consist of a radial distribution of sources that may lead to varied levels of plane wave and higher order mode excitation within the duct. If the distributed acoustic sources are modeled as a single, net source, then accurate predictions of radiated sound can only be made if an appropriate weighted average of the acoustic Green's function is made.

The results showing G' and G'_D for the rigid duct with far field location on axis with the duct are shown in Figures 54 and 55, respectively. The axial location of the source was $z/L=0$. The same is plotted for the elastic duct in Figures 56 and 57. These four plots are repeated with the far field location at an angle of 45 degrees from the duct axis in Figures 58 through 61. In all figures the horizontal axes represent the frequency normalized by either the first organ pipe frequency or as ka as before. The ordinate represents the radial position normalized by the duct radius.

The rigid duct exhibits nearly uniform magnitude of both G' and G'_D in the radial direction at lower frequencies where the plane wave mode is dominant. As expected from the axial location of the source, G' is dominated by the odd ordered organ pipe modes at all radial locations, whereas G'_D is dominated by the even ordered modes. At higher frequencies the higher order modes lead to more substantial radial dependence of both G' and G'_D . For example, the (0,1), (1,1), and (0,2) modes appear to be more strongly excited at the duct center (near $r/a=0$). The modes (3,0) and (3,1) are considerably stronger near the duct wall ($r/a=1$).

A number of interesting features are observed when comparing the results for the elastic shell. First, the lower frequencies are observed to exhibit radial dependence that was not observed for the rigid duct. The on axis data (Figures 56 and 57) indicate an increased sensitivity to the radial position at higher frequency, with particularly large magnitudes observed near the duct centerline. At 45 degrees off axis, (Figures 60 and 61), the elastic shell exhibits the largest values at the outer radial locations at high frequency.

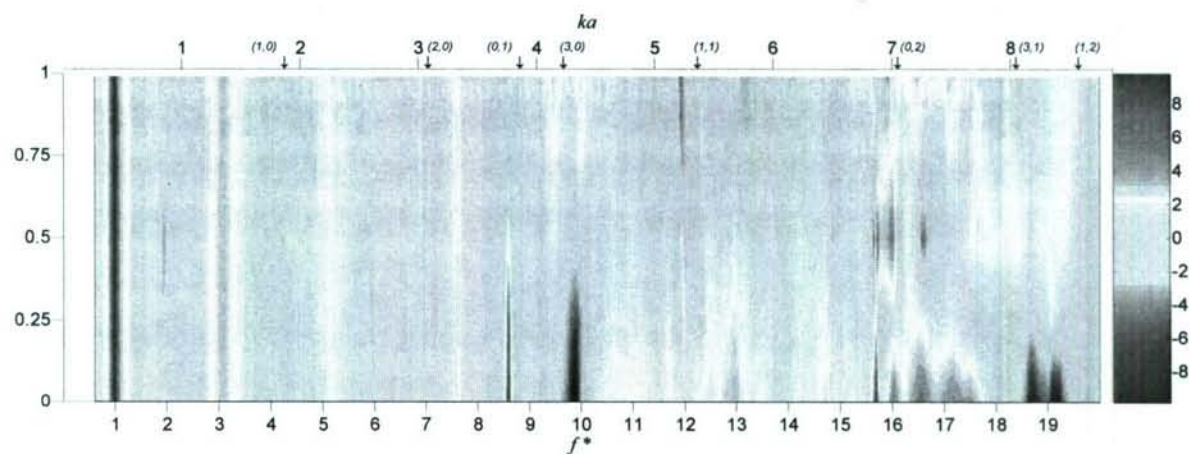


Figure 54 Radial dependence of G' (on axis) for rigid duct

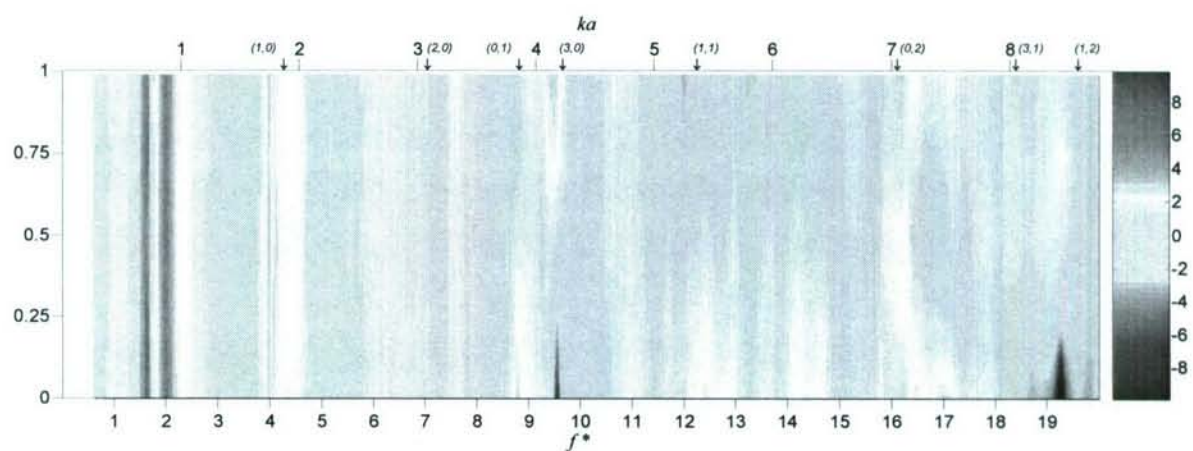


Figure 55 Radial dependence of G_D' (on axis) for rigid duct

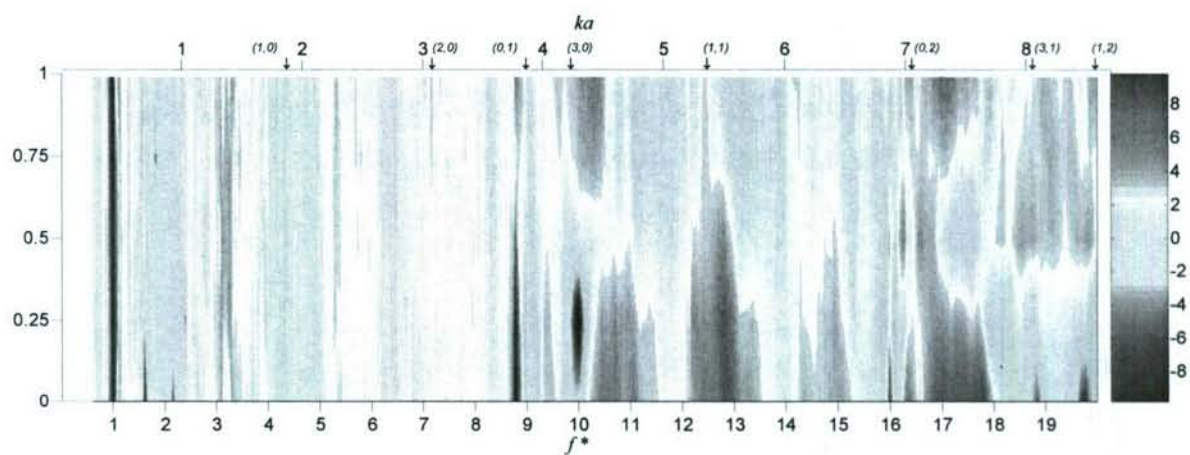


Figure 56 Radial dependence of G' (on axis) for elastic duct

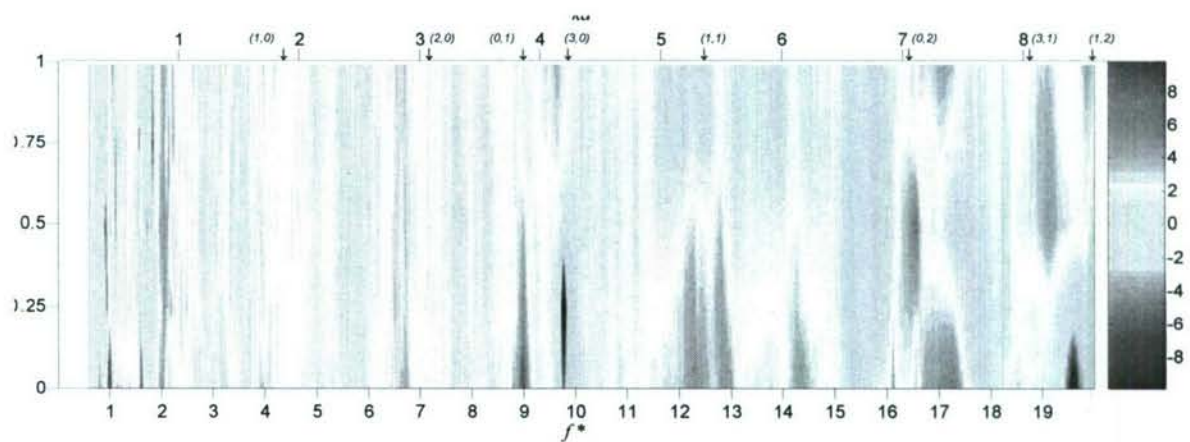
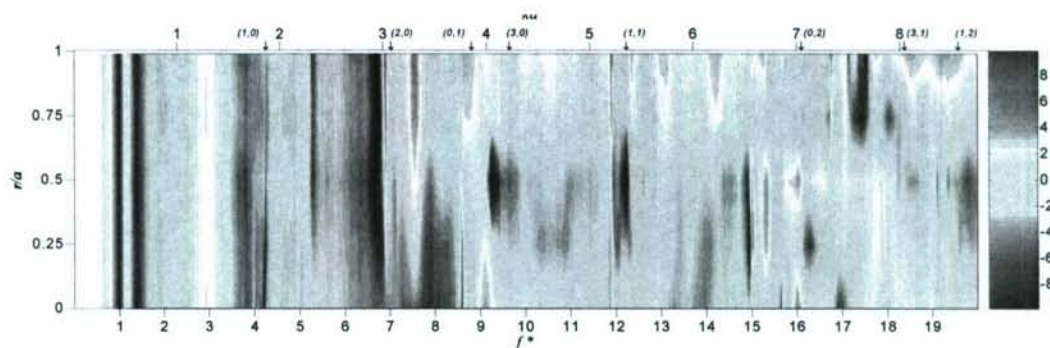
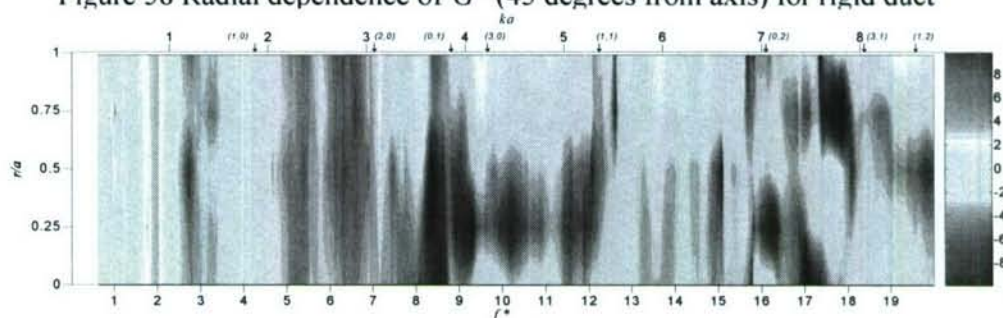
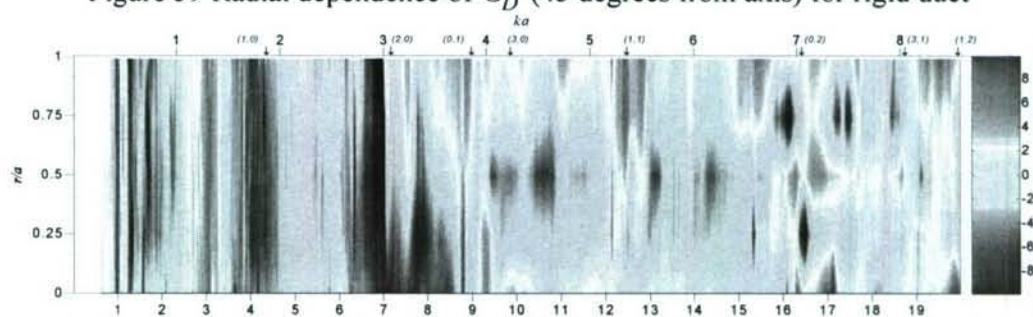
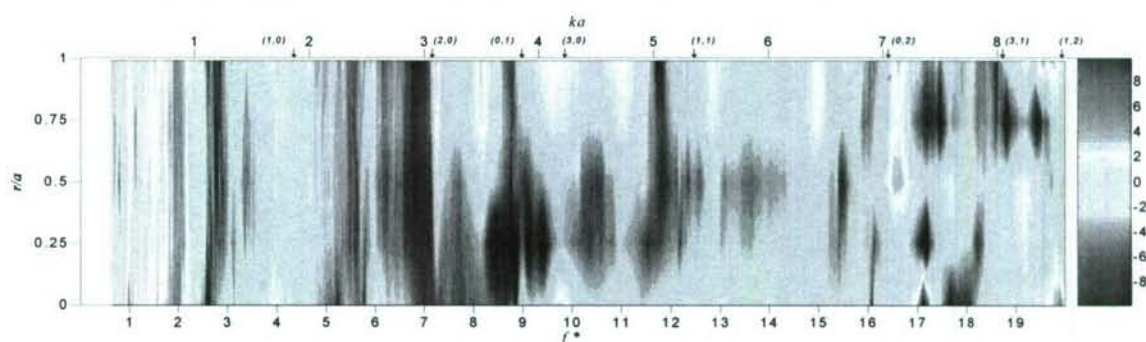


Figure 57 Radial dependence of G'_D (on axis) for elastic duct

Figure 58 Radial dependence of G' (45 degrees from axis) for rigid ductFigure 59 Radial dependence of G_D' (45 degrees from axis) for rigid ductFigure 60 Radial dependence of G'' (45 degrees from axis) for elastic ductFigure 61 Radial dependence of G_h' (45 degrees from axis) for elastic duct

8.0 PROPELLER - ELASTIC DUCT INTERACTIONS

8.1 Introduction

The original objectives of this research involved the development of the experimental tools necessary to investigate the interaction between the acoustic sources of a ducted rotor, the convecting hydrodynamic pressure field, and the shell vibrations. Consultation with engineers from NSWC, ONR, and Electric Boat provide significant feedback and technical guidance for this part of the research. One of the primary objectives that was added during the last phase of the project involved the investigation of inlet distortion effects on the vibro-acoustic response of a ducted rotor. This results presented in this section are intended to be a status update for this work, which is continuing under ONR Grant #N00014-07-1-0570.

The general boundary conditions and experimental setup for the propeller-duct interaction experiments were described in Section 2. The duct length was 31 inches, with a corresponding first organ pipe mode $f^*=189\text{Hz}$. The significant change of relevance to the present work is the use of varied inlet section design such that variable inlet total pressure as well as the overall level and spectral content of the turbulent fluid motions were obtained. These inlet conditions were provided in both an axisymmetric as well as a non-symmetric configuration as described in the following subsections. These experiments provide a method to directly access the impact of inlet distortion on the vibration response of the shell.

8.2 Rotor Inflow Boundary Conditions

The properties of the mean flow as well as the turbulence were documented in detail for several inlet duct section geometries. The measurements were acquired using standard hot-wire anemometry techniques. Specifically, a single hot-wire probe was calibrated and traversed radially in the duct at the rotor inlet plane. Airflow was provided by an auxiliary blower for these experiments. The mean velocity and RMS of the fluctuating velocity acquired for the baseline, smooth inlet geometry is shown in Figure 62. Data are shown for several streamwise locations with respect to the duct inlet. The data labeled L0 were acquired at the inlet of the duct, and exhibit a typical inviscid “overshoot” due to the strong streamline curvature that exists at the inlet. The location “L2” (2 inches from the inlet) shows a more standard velocity profile. The boundary layer thickness is observed to increase monotonically with increased distance downstream as expected. The corresponding RMS values are consistent with typical boundary layer measurements.

The autospectral densities from several locations in the boundary layer are shown in Figure 63. These data are important because they form the input excitation for the aeroacoustic source terms. It should be observed that the spectral levels continue to increase at low frequency. That is, there is no “leveling off” of the spectra at low frequency that would normally be expected in free shear turbulence. The reason for this is well understood in the boundary layer turbulence community, and is related to the long streamwise structures that exist in both the very near wall region as well as the outer regions of the boundary layer. This is an important aspect for modeling the hydroacoustic and structural acoustic problem. Specifically, the majority of the unsteady fluid motions that lead to structural vibrations can be considered to be strongly anisotropic in nature. The higher frequency (small scales) that are more closely model by isotropic turbulence theory are considerably smaller in magnitude and thus do not contribute significantly to the acoustic signature of the ducted rotor system.

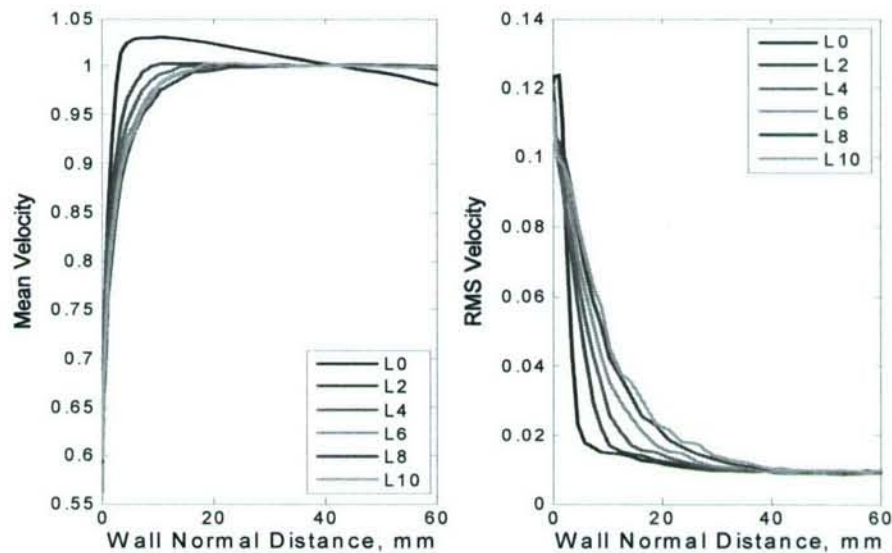


Figure 62 Mean velocity and RMS of fluctuating velocity acquired at various streamwise locations (in inches from the inlet) for the smooth wall inlet geometry.

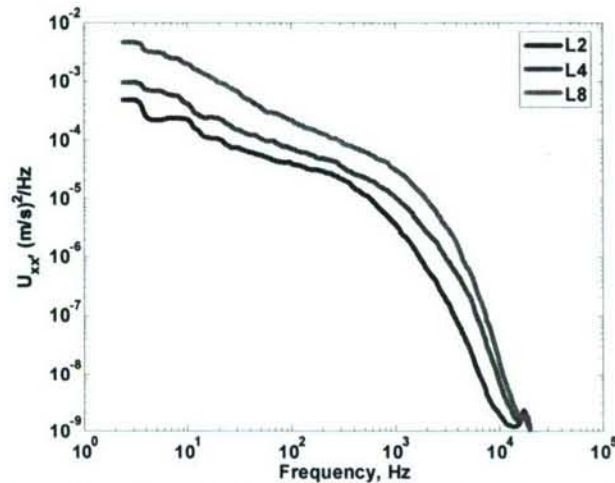


Figure 63 Sample velocity spectral results from smooth inlet boundary layer at a wall normal location of 20mm.

A second rotor inlet geometry was designed, machined, and tested in the ducted rotor facility. A solid model image of the geometry is shown in Figure 64. The interior wall of this section is configured as the standard “NASA hump”. The profile of the NASA hump was designed specifically to have a fixed separation point on a convex surface. The advantage of this geometry for the present application is that it provides a well defined, large scale turbulent approach flow to the rotor without generating additional noise. That is, since the hump profile does not contain sharp corners it will not radiate sound efficiently, and thus will not add additional sources to be considered in the hydro/structural problem.

The velocity results from the symmetric NASA hump are shown in Figures 65 and 66. The mean and RMS of velocity describe a typical “wake-like” behavior that is followed by a redeveloping boundary layer at the downstream locations. The spectral results indicate a prominent shedding frequency that decays in the streamwise direction. The furthest location measured (L8) indicates that the turbulence has “relaxed” to a state that can be roughly approximated as isotropic turbulence. That is, three distinct regions can be identified in the spectral plot: a flat region at low frequency, a $-5/3$ slope region characteristic of the inertial subrange, followed by an exponential roll-off at the highest frequencies.



Figure 64 Image of the inlet section with interior axisymmetric “NASA hump”

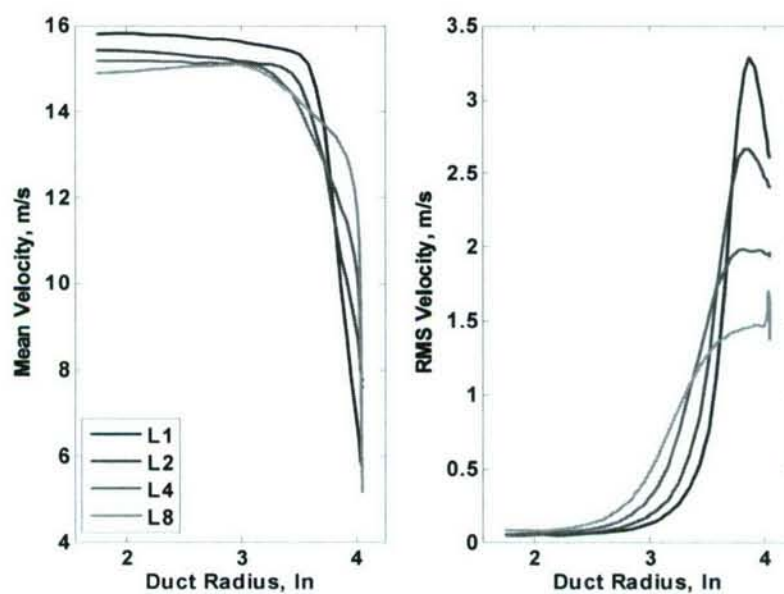


Figure 65 Mean and RMS of velocity in the wake of the NASA hump

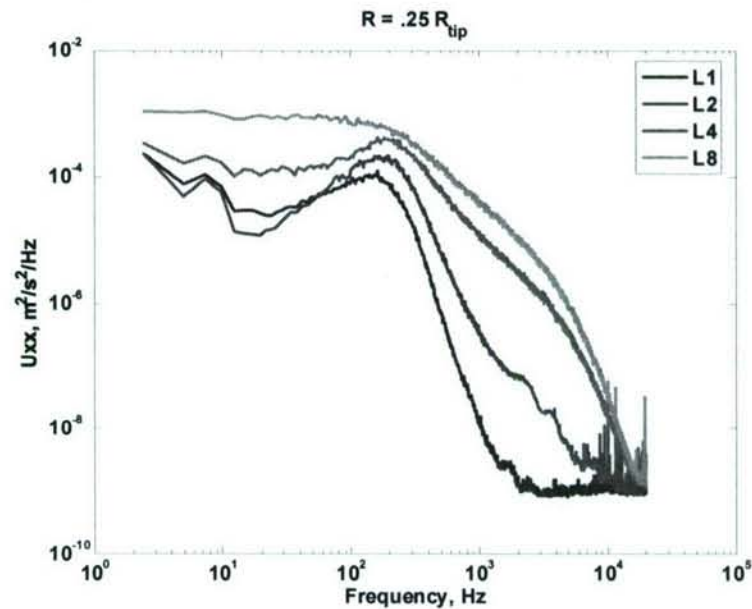


Figure 66 Sample velocity spectra obtained in the wake of the NASA hump.

The third and final geometry constructed for this study is shown in Figure 67. The model is configured to generate a circumferential distortion to the rotor. Specifically, the height of the NASA hump described in the previous geometry was varied around the circumference from zero at one location (say, 0 degrees) to a maximum of 0.375 inches (same as above) at 180 degrees. This resulted in a circumferential varied inlet velocity and inlet turbulent level as shown in Figure 68. The corresponding spectral results are shown in Figure 69.

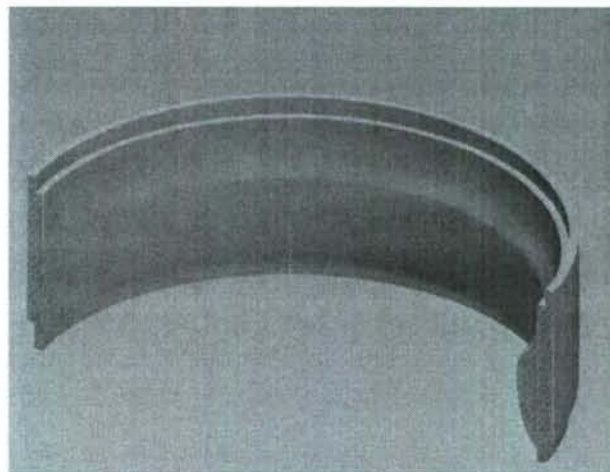


Figure 67 Model of the non-symmetric inlet geometry

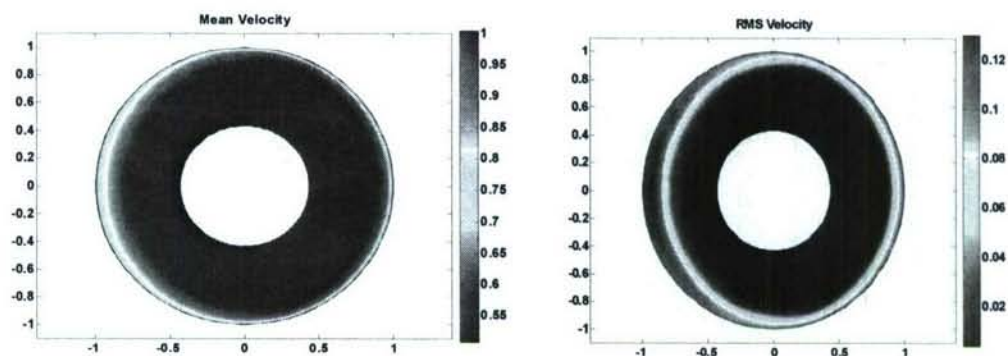


Figure 68 Mean and RMS contours downstream of the non-symmetric inlet.

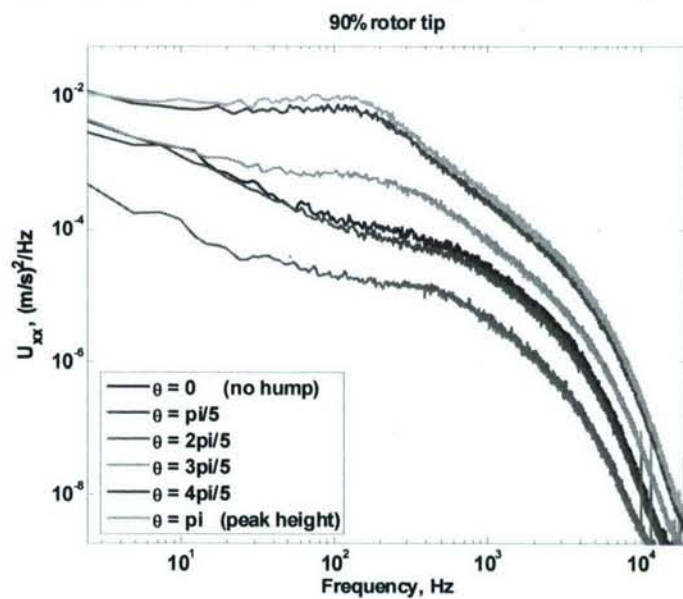


Figure 69 Sample velocity spectra downstream of the non-symmetric hump

8.3 In-vacuo Analysis of Elastic Shell

The natural frequencies of the elastic shell can be determined from analysis of the Donnell equations. By assuming the number of circumferential harmonics is large compared to the axial wave-number (Yu's assumption), the natural frequencies are given by equation 2.88 of Leissa (1973):

$$\Omega^2 = kn^4 + (1-\nu)^2 \left(\frac{\lambda_m}{n} \right)^4. \quad (59)$$

The nondimensional frequency, Ω , is given by:

$$\Omega^2 = \frac{\rho(1-\nu^2)R^2\omega^2}{E}, \quad (60)$$

where E is the elastic modulus of the shell, and ω is the circular frequency ($2\pi f$). The axial wave-number is given by the parameter λ_m , defined as:

$$\lambda_m = \left(\frac{R}{l} \right) \epsilon_m \quad (61)$$

where ϵ_m represent the roots of the clamped-clamped shell equation:

$$\cos(\epsilon_m) \cosh(\epsilon_m) - 1 = 0 \quad (62)$$

given as

$$\epsilon_m = 1.506\pi, 2.500\pi, 3.500\pi, \text{ etc...}$$

The results for the parameters given for the thin nickel shell are shown in Figure 70. The modal density is shown in Figure 71.

The natural frequencies of the shell were determined experimentally by exciting the shell using a speaker in close proximity to the shell. The cross spectral density between the shell vibration signal and the excitation signal provided the amplitude and phase information needed to determine the shell mode order by inspection. Contour plots of the vibration modes are shown in Figure 72. Each image shows 120 degrees of the shell that represents the practical limit of the projected view of the shell from a stationary laser source.

It is clear from inspection of Figure 70 that the true frequencies are lower than the values predicted by the in-vacuo shell theory. It is presumed that this is due to the fluid loading effects on the shell. Specifically, at 300Hz, the fluid loading factor $(\rho c)/(\rho_s h \omega) = 0.35$. It can also be noticed that two of the circumferential modes (15 and 16) have "locked on" to the organ pipe frequency of 189 Hz. The fluid loading factor at this frequency is 0.58, which suggests that the fluid

loading stress, the extensional (membrane) and flexural stresses are all important in determining the modal frequencies.

As a final note, the axial profile of the mode shapes of the in-vacuo shell vibration is of interest for comparison with the experimental data. The radial motion is given by (Leissa, 1973 eqn 2.86)

$$w = 2C \left[\sinh(\epsilon) - \sin \epsilon - \frac{1}{\cosh \epsilon - \cos \epsilon} \right] \quad (63)$$

$$[(\sinh \epsilon - \sin \epsilon)(\cosh \lambda s - \cos \lambda s) - (\cosh \epsilon - \cos \epsilon)(\sinh \lambda s - \sin \lambda s)]$$

The first three mode shapes are shown in Figure 73.

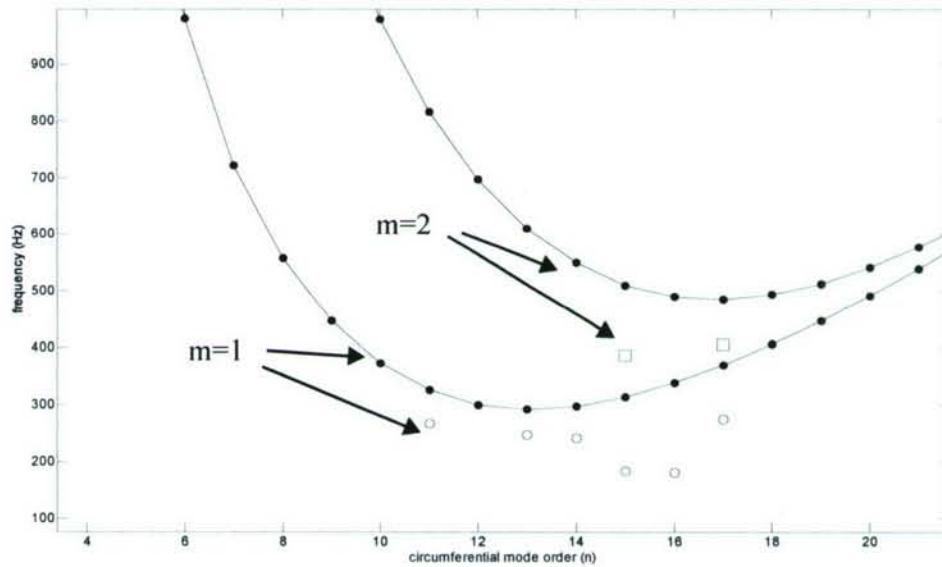


Figure 70 Theoretical (in-vacuo) shell frequencies (connected for reference) and measured values (open symbols).

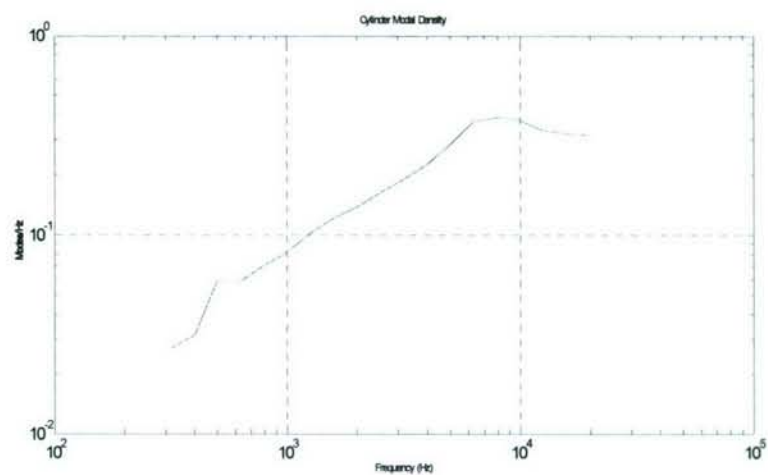


Figure 71 Modal density for the elastic shell

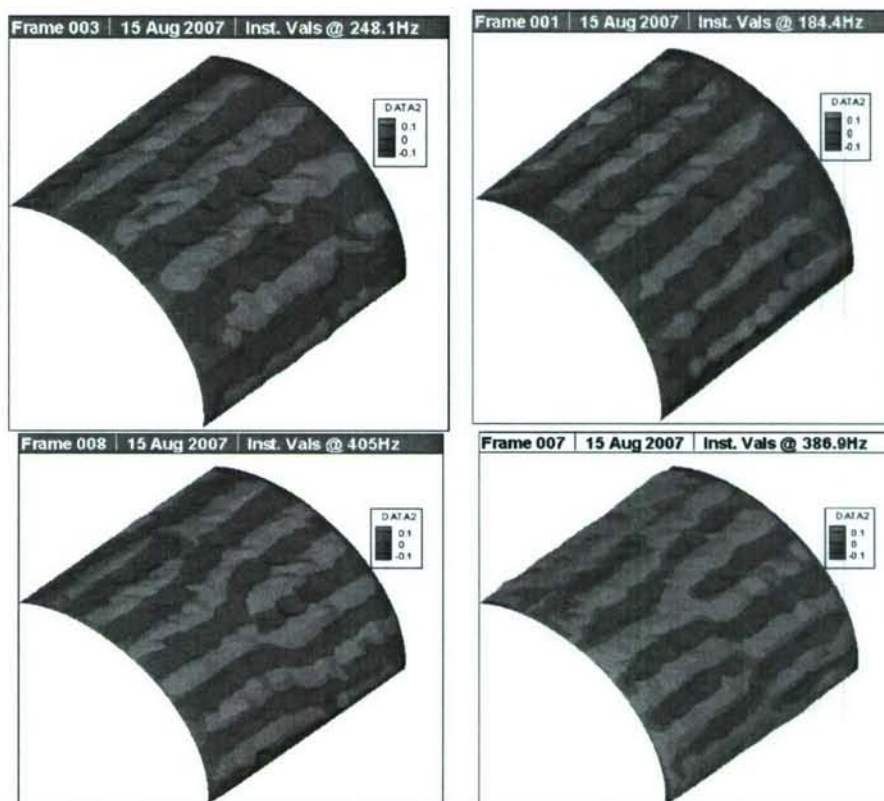


Figure 72 Visualization of measured mode shapes from acoustic excitation.

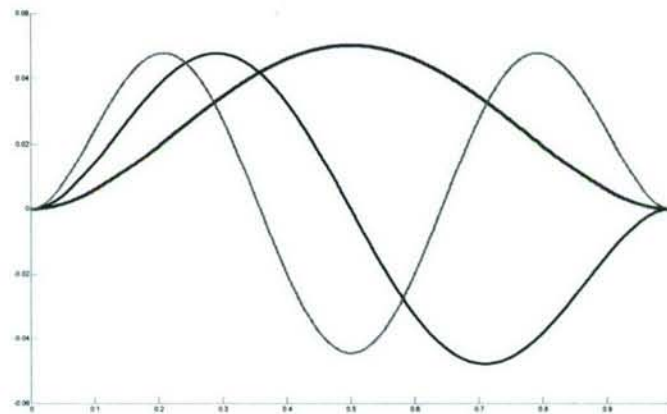


Figure 73 Axial profile of the eigenmodes of a clamped-clamped shell

8.4 Effects of Inlet Distortion

The main objectives in the final phase of this research involved the measurement of shell vibration amplitudes while the rotor ingests a distorted inlet flow. Under these condition, non-uniform convecting hydrodynamic pressures are present, as well as a circumferential varying acoustic source magnitude.

The experiments were conducted as follows. First, the distorted inlet geometry described above was installed at the inlet to the ducted rotor facility. The scanning LDV and single point LDV were then used to obtain the two point correlation measurements of the duct. The non-symmetric portion of the inlet was then “clocked” at 90 degree intervals with respect to the laser location and the two point scan was repeated. Preliminary results from a single point on the duct are shown in Figures 74 and 75. From a broad view, the overall amplitude of the vibration is not significantly different at the four locations around the duct. However, some clear differences are noted. First, the low frequencies show a broadband excitation that is 10dB higher for two of the neighboring locations. Additionally, the closer view of the lowest frequency modes in Figure 75 suggest that substantial differences do exist between the four locations. It appears that several of the modes have either shifted frequency, or are significantly less excited at certain locations.

The current focus is being placed on continued analysis of the acquired data. For example, the eigenmodes of the full two-point correlation matrix will allow the amplitudes of each azimuthal mode order to be compared for the various conditions. Additionally, the dependence of the structural vibration on rotor speed is currently being examined.

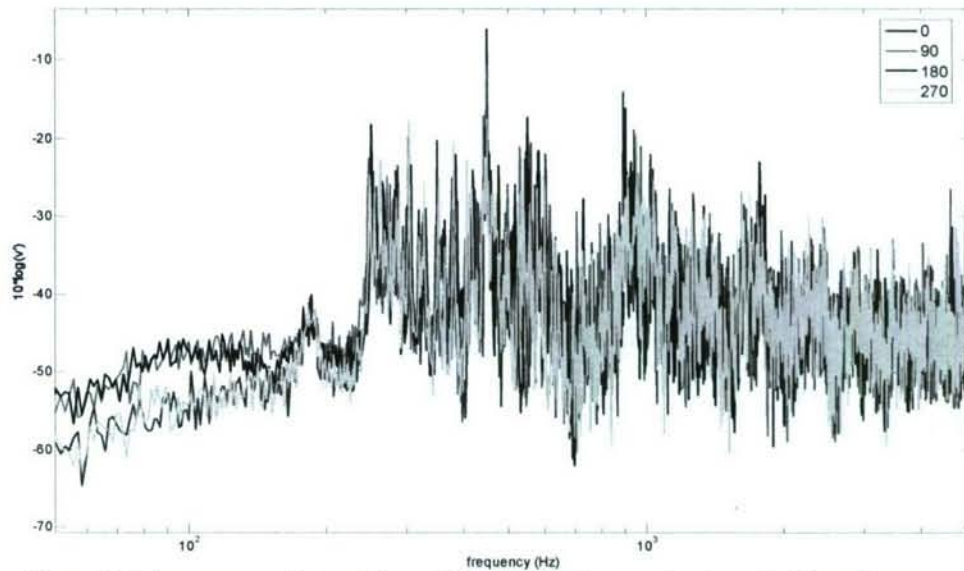


Figure 74 Autospectral densities of duct vibration at 4 azimuthal locations.

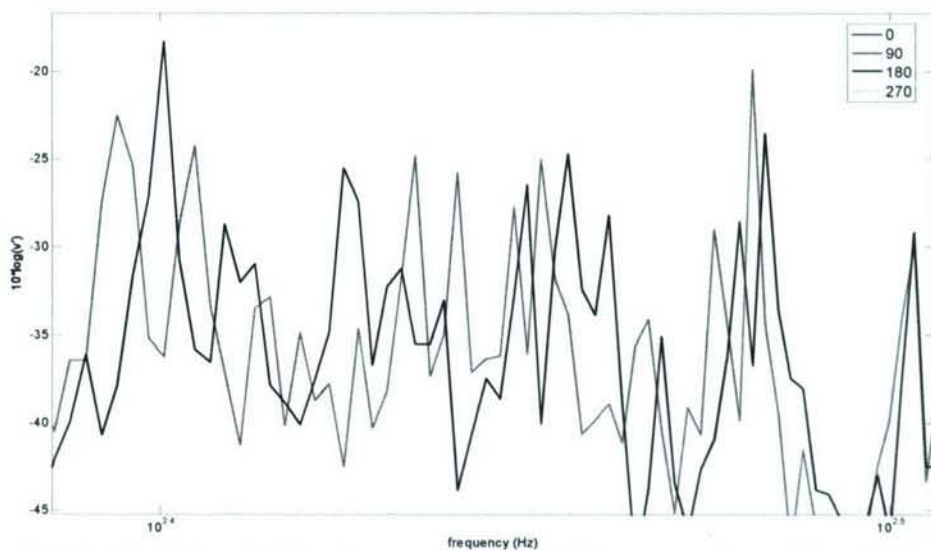


Figure 75 Detailed view of vibration spectral amplitudes at two circumferential locations of the duct.

9.0 DISCUSSION AND CONCLUSIONS

In addition to the detailed conclusions provided in each of the sections of this proposal, it is useful to provide some overall commentary and conclusions related to the successes of the research program as well as issues related to the ongoing work.

The initial objective of this research was to develop the experimental tools required for conducting a broad range of studies related to structural acoustics. More specifically, the use of air as a working fluid for investigating fluid-loaded cylindrical shells with complex hydrodynamic and acoustic forcing was considered. The challenge in this regard was to create high quality test specimens that were very thin, thus increasing the importance of fluid loading. Handling of the thin materials, applying uniform and measured static tension, and fixing uniform boundary conditions were all important considerations for the development of the experimental apparatus.

The facilities and instrumentation already available included the Anechoic Wind Tunnel, an 80 microphone phased array, and the initial design of the rigid-walled ducted rotor system. During this project, two laser Doppler vibrometry systems as well as an array of miniature microphones were added. Data acquisition and processing systems were also upgraded.

As described in this report, two new experimental test configurations were designed and manufactured. The first was a flat plate arrangement in which various materials could be stretched over a template with an arbitrary opening. This allowed the study of how the fluid loading effects the natural frequencies of the membrane. The geometry also provided a unique opportunity to investigate the effects of complex hydrodynamic forcing. The capabilities developed in these experiments presents a unique opportunity for studies in structural acoustics and fluid-structure interactions. Specifically, the effects of fluid loading, complex and non-homogeneous convecting pressures, and acoustic forcing can all be considered in terms of modal frequencies, mode shape functions, and the net radiated sound from the induced structural motion.

The second new facility that was designed and constructed under this project was the nickel shell used in the ducted rotor rig. Although the measurement objectives and capabilities are similar to the flat plate/membrane apparatus, a number of additional and complex scientific objectives can be addressed due to the complex nature of the shell vibrations. Also, a number of practical problems can be addressed such as the interaction with swirling rotor wakes, the fluid loading effects, etc. The present work began a new project where these features are examined using inflow bound-

ary conditions that exhibit strong velocity distortion as well as asymmetry in the turbulence characteristics. A large amount of experimental data is currently being processed to examine the frequency dependence of the modes, the modal shape functions as determined from the eigenvectors of the two point structural correlation matrix, and finally near-field and far-field sound radiation that is generated by the shell vibrations. These data will be compared to ongoing analytical work at Notre Dame that is focused on the swirling wake distribution downstream of the rotor and the interaction of the shell modes with the convecting pressures.

In closing, the project is complete and has been successful in meeting the original objectives of creating the experimental tools and expertise that allows practical structural acoustic problems to be studied using air-analog experiments. The processing and presentation of the complete data set including acoustic forcing, simple hydrodynamic forcing, and ducted rotor forcing is still in progress as part of the ongoing ONR funded project involving inlet distortion and wake development.

REFERENCES

- Amiet, R., "High Frequency Thin-Airfoil Theory for Subsonic Flow," AIAA Journal, Vol. 14, No. 8, 1976, pp. 1076-1082.
- H. M. Atassi, J. Fang, S. Patrick, Direct calculation of sound radiated from bodies in nonuniform flows, Journal of Fluids Engineering 115 (1993) 573-579.
- Belousov, Y. I. and Rimskii-Korsakov, A.V. (1975). "The reciprocity principle in acoustics and its application to the calculation of sound fields of bodies," Sov. Phys. Acoust., **21**, pp. 103-109.
- Bendat, J. and Piersol, A. (2000). *Random Data: Analysis and Measurement Procedure*, 3rd ed. (Wiley, New York).
- P. Bent, D. McLaughlin, Enhancements to noise source measurement techniques for turbomachinery, 15th AIAA Aeroacoustics Conference, Long Beach, California, October 25-27, 1993.
- W. K. Blake, Mechanics of Flow-induced Sound and Vibration (two volumes), Academic Press Inc. New York., 1986.
- Davies, H. G., "Sound from Turbulent-Boundary-Layer-Excited Panels," Journal of the Acoustical Society of America, Vol. 49, No. 3, 1971, pp. 878-889.
- P. E. Doak, Excitation, transmission and radiation of sound from source distributions in hard-walled ducts of finite length (i): The effects of duct cross-section geometry and source distribution space-time pattern, Journal of Sound and Vibration 31 (1) (1973) 1-72.
- P. E. Doak, Excitation, transmission and radiation of sound from source distributions in hard-walled ducts of finite length (ii): The effects of duct length, Journal of Sound and Vibration 31 (2) (1973) 137-174.
- R. Dunne, M. S. Howe, Wall-bounded blade-tip vortex interaction noise, Journal of Sound and Vibration 202 (5) (1997) 605-618.
- F. Fahy, Some applications of the reciprocity principle in experimental vibroacoustics, Acoustical Physics 42 (3) (2003) 217-229.
- Fahy, F. J. (1989). *Sound Intensity* (Elsevier Science, New York). pp. 110-149.
- Fahy, F. J. (1995). "The vibro-acoustic reciprocity principle and applications to noise control," *Acustica*, **81**, pp. 544-558.
- Goldstein, M. E. (1976). *Aeroacoustics* (McGraw-Hill, New York).
- Graham, W. R., "Boundary Layer Induced Noise in Aircraft, Part I: The Flat Plate Model," Journal

- of Sound and Vibration, Vol. 192, No. 1, 1996, pp. 101-120.
- Helmholtz, H. (1859). "Theorie der Luftschwingungen in Röhren mit offenen Enden" ("Theory of air oscillations in tubes with open ends"), *J. reine ang. Math.* **57**, 1-72.
- P. J. Huber, *Robust Statistics*, Wiley, New York, 1981.
- D. L. Huff, Fan noise prediction: Status and needs, NASA/TM-97-206533.
- Jacobsen, F. and de Bree, H.-E. (2005). "A comparison of two different sound intensity measurement principles," *J. Acous. Soc. Am.*, **118**, pp. 1510-1517.
- H. Kobayashi, Three dimensional effects on pure tone fan noise due to inflow distortion, AIAA 11th Fluid and Plasma Dynamics Conference, Seattle, Washington, July 10-12, 1978.
- H. Levine, J. Schwinger, On the radiation of sound from an unflanged circular pipe, *Physical Review* **73** (4) (1948) 383-406.
- C. Lee, M. K. Chung, Y. H. Kim, A prediction model for the vortex shedding noise from the wake of an airfoil or axial flow fan blades, *Journal of Sound and Vibration* **164** (2) (1993) 327-336.
- Lyamshev, L. M. (1959). "A question in connection with the principle of reciprocity in acoustics," *Sov. Phys. Dokl.* **4**, pp. 406-409.
- Maury, C., Gardonio, P., and Elliot, S. J., "A Wavenumber Approach to Modelling the Response of a Randomly Excited Panel, Part I: General Theory," *Journal of Sound and Vibration*, Vol. **252**, No. 1, 2002, pp. 83-113.
- N. Moisev, B. Lakshminarayana, D. E. Thompson, Noise due to interaction of boundary-layer turbulence with a compressor rotor, *Journal of Aircraft* **15** (1) (1978) 53-61.
- L. Mongeau, D. E. Thompson, D. K. McLaughlin, A method for characterizing aerodynamic sound sources in turbomachines, *Journal of Sound and Vibration* **181** (3) (1995) 369-389.
- C. L. Morfey, Rotating blades and aerodynamic sound, *Journal of Sound and Vibration* **28** (3) (1973) 587-617.
- P. M. Morse, K. U. Ingard, *Theoretical Acoustics*, Princeton University Press, Princeton, New Jersey, 1968.
- W. Neise, Application of similarity laws to the blade passage sound of centrifugal fans, *Journal of Sound and Vibration* **43** (1) (1975) 61-75.
- W. Neise, B. Barsikow, Acoustic similarity laws for fans, *Journal of Engineering for Industry* **104** (1982) 162-168.
- A. D. Pierce, *Acoustics: An introduction to Its Physical Principles and Applications*, McGraw-Hill,

- New York, 1981.
- Pope, S., *Turbulent Flows*, Cambridge University Press, London, 2000.
- D. A. Quinlan, M. H. Krane, Aeroacoustic source identification using frequency dependent velocity scaling, 2nd AIAA and CEAS Aeroacoustics Conference, State College, Pennsylvania, May 6-8, 1996.
- Rayleigh, J.W.S. (1945). *Theory of Sound* (Dover, New York).
- M. Sevik, Sound radiation from a subsonic rotor subjected to turbulence, NASA SP 304 (11) (1974) 493-511.
- Seybert, A. F. (1981). "Statistical errors in acoustic intensity measurements," *J. Sound & Vib.*, **75**, pp. 519-526.
- Steenhoek, H. F. and ten Wolde, T. (1970). "Reciprocal measurement of mechanical-acoustical transfer functions," *Acustica*, **23**, pp. 302-305.
- J. Weidemann, Analysis of the relations between acoustic and aerodynamic parameters for a series of dimensionally similar centrifugal fan rotors, NASA Technical Translation NASA TT F-13, 798.
- Wong, G. (1991). "Precision method for phase match of microphones," *J. Acous. Soc. Am.*, **90**, pp. 1253-1255.
- S. E. Wright, The acoustic spectrum of axial flow machines, *Journal of Sound and Vibration* 45 (2) (1976) 165-223.
- Wu, S. F., and Maestrello, L., "Responses of Finite Baffled Plate to Turbulent Flow Excitations," *AIAA Journal*, Vol. 33, No. 1, 1995, pp. 13-19.
- Z. Zhang, L. Mongeau, S. H. Frankel, Broadband sound generation by confined turbulent jets, *Journal of the Acoustical Society of America* 112 (2) (2002) 677-689.